

University of Alberta

Glaciers of the Canadian Rockies and their response to global climate change

by

Edward Pollock

A thesis submitted to the Faculty of Graduate Studies and Research
in partial fulfillment of the requirements for the degree of

Master of Science

Department of Earth and Atmospheric Science

©Edward William Pollock

Fall 2009

Edmonton, Alberta

Permission is hereby granted to the University of Alberta Libraries to reproduce single copies of this thesis and to lend or sell such copies for private, scholarly or scientific research purposes only. Where the thesis is converted to, or otherwise made available in digital form, the University of Alberta will advise potential users of the thesis of these terms.

The author reserves all other publication and other rights in association with the copyright in the thesis and, except as herein before provided, neither the thesis nor any substantial portion thereof may be printed or otherwise reproduced in any material form whatsoever without the author's prior written permission.

Examining Committee

Andrew Bush, Department of Earth and Atmospheric Science

Bruce Sutherland, Department of Earth and Atmospheric Science and the Department of
Physics

Gordon Swaters, Department of Mathematical and Statistical Sciences

ABSTRACT

This study investigates the interactions between carbon dioxide, climate, and glaciers of the Canadian Rockies under a relatively conservative IPCC emission scenario for the 21st century through the use of the PSU/NCAR MM5 mesoscale model (MM) nested within the Princeton GFDL global atmosphere-ocean model. A simple model of orographic precipitation is developed and indicates that if relative humidities change little in a warmer climate the Rocky mountains will experience substantially larger precipitation increases than the global average, despite a weakening midlatitude jet. Furthermore, a simple energy balance model indicates that the elevation of equilibrium net snow accumulation in the Rocky mountains rises steadily through the 21st century. Precipitation increases at high elevations offset increases in melt, particularly in 2050 but also evident at some isolated high elevations in 2100.

Preface:

Humankind is witnessing the most rapid climate change event seen in recorded history and this trend is likely to continue, and accelerate through the 21st century, as economies and populations grow under a significant dependence on fossil fuels (IPCC 2007). Global land surface temperatures are estimated to have risen by 0.7°C in the last century (Jones and Moberg, 2003). Even under this modest rise in global mean temperature, glaciers in midlatitudes and the tropics have receded substantially since the beginning of the 20th century (Oerlemans 2005). In addition, the rate of Arctic sea ice loss dramatically accelerated in the late 20th and early 21st centuries (Lindsay and Zhang 2005, Serreze et al. 2007, Stroeve et al. 2007), perhaps indicative of a dramatic shift in equilibrium state of the Arctic atmosphere-ocean system (Lenton et al. 2008). Estimates of global mean temperature under projected increases in atmospheric CO₂ concentrations predict much greater increases during the next century than were seen during the last (IPCC 2007), meaning that global warming is accelerating, further complicating matters concerning the eventual outcome of various components of the Earth's cryosphere. Global warming will therefore not only demand adaptive strategies, but also improved climate prediction to preserve our current way of life for future generations.

Increasing surface temperatures will not only cause a reduction in sea-ice, but they will also have an impact on the hydrological cycle, influencing the magnitude and location of precipitation and evaporation. There is more and more consensus among climatologists that increasing precipitation amounts, particularly at mid and high latitudes, are an inevitable consequence of warmer temperatures because a warmer atmosphere is able to contain more water vapour (Manabe et al. 1991, Wetherald and Manabe 2003, Held and Soden 2006, Ingram 2002, Lorenz and DeWeaver 2007). Mid-latitude cyclones are expected to become less frequent but more expansive and rain-producing (Bush and Peltier 1994, Geng and Sugi 2003), meaning that precipitation

events will be less frequent but more intense and widespread.

The precipitation increases can lead to increased snowfall in cold regions of the planet, such as the high latitudes and high altitudes (provided temperatures do not rise to the point where they affect a change in precipitation type). In fact, numerical models have predicted increases in snow and ice mass balance in Antarctica in a warmer climate due to increasing snowfall (Boer et al. 1991, Thompson and Pollard 1997). Such increases are largely attributable to increases in mid and high latitude poleward moisture transport in a warmer climate (Manabe et al. 1991).

Temperate glaciers (for which the ice base is not frozen to the bed) at midlatitudes are characterized by rapid mean annual flow rates and distinct accumulation and melt seasons, making their areal extent a strong function of mean temperature and snowfall. Numerical modelling studies of precipitation along the West coast of North America have shown increases in net annual snowfall at high altitudes in a warmer climate (Kim et al. 2002), and although much of the lower elevation glacial ice in Western Canada is rapidly disappearing, increases in the net volume contained at high elevation has been observed (Schiefer et al. 2007).

The relationship between glacial extent and mean temperature can be investigated using computational geophysical fluid dynamics modelling. Use of a mesoscale atmospheric model combined with observed meteorological inputs can yield a realistic simulation of the present day high elevation Rocky mountain climate. The same procedure can then be used to examine how such an environment may change under predicted meteorological inputs, generated by IPCC emission scenarios combined with general circulation model (GCM) experiments. The purpose of this study is to quantify changes in Rocky mountain climate in the 21st century and with specific emphasis on snow and ice mass balance in the target region. This will be done using a global atmosphere-ocean general circulation model coupled with a substantially higher spatial

resolution mesoscale model.

Chapter 1 describes the GCM and the global climate it predicts for the 21st century, with emphasis on the Rocky Mountain region. Chapter 2 describes the non-hydrostatic mesoscale model (MM) and its results, focusing on Rocky mountain processes not resolvable by the hydrostatic, large scale physics of the GCM.

Table of Contents

1. Chapter 1	1
1. Introduction	2
2. Global model setup	3
3. Results and Analysis	5
1. Trends in Global climate	5
2. Trends in Rocky mountain Climate	19
3. Trends in Orographic forcing	29
4. Discussion/Concluding Remarks	34
2. Chapter 2	39
1. Introduction	40
2. Regional model setup	44
3. Results and Analysis	46
1. January and July Trends	47
2. Annual Trends	61
3. Snow Mass Balance Trends	67
4. Discussion/Concluding Remarks	75
3. Final Remarks	78
4. References	80

List of Figures and Tables

Chapter 1

Figure 1.1: Carbon dioxide concentrations	4
Figure 1.2: Global temperature and precipitation	6
Figure 1.3: Hövmeuller diagrams	8
Figure 1.4: 50-year changes in latitude and height	11
Figure 1.5: Eliassen-Palm flux vectors	13
Figure 1.6: Meridional circulation changes	15
Figure 1.7: ENSO 3.4 regions sea surface temperatures	16
Figure 1.8: Changes in the El Niño Southern Oscillation	17
Figure 1.9: Regional mean temperature	20
Figure 1.10: January Regional mean temperature	21
Figure 1.11: July Regional mean temperature	21
Figure 1.12: Clouds, Annual and Seasonal Changes	23
Figure 1.13: Vertically integrated clouds and radiation	25
Figure 1.14: Regional mean Precipitation and wind	27
Figure 1.15: January regional mean Precipitation and wind	28
Figure 1.16: Regional Snowfall	28
Figure 1.17: Orographic forcing	30
Figure 1.18: Uplift potential condensation	33

Chapter 2

Figure 2.1: Regional model domain setup schematic	43
Figure 2.2: July changes in surface temperature and wind	48
Figure 2.3: July changes in surface insolation	49
Figure 2.4: January changes in precipitation and wind	51
Figure 2.5: January snowfall	53
Figure 2.6: January surface temperature	53
Figure 2.7: Uplift potential latent heat release	57
Figure 2.8: Liquid and vapour water states, and seasonal changes	59
Figure 2.9: Annual surface temperature	62
Figure 2.10: Annual surface radiation	63
Figure 2.11: Annual radiative melt	63
Figure 2.12: Annual rainfall	65
Figure 2.13: Annual snowfall	65
Figure 2.14: Sources of snow melt	70
Figure 2.15: Annual mass balance	71
Figure 2.16: Equilibrium line	73
Table 2.1: Average ELA and Positive mass balance area	74
Table 2.2: Mass balance results for locations of interest	74

**Chapter 1: Effects of increasing atmospheric
CO₂ concentrations on Rocky mountain
climate as simulated by a global coupled
atmosphere-ocean general circulation model.**

1: Introduction

Ever since Callendar (1938) put forth the idea that increasing atmospheric CO₂ may lead to an increase in global mean temperature, the subject has been gradually receiving more interest as the ongoing collection of temperature data began to prove his hypothesis. In the mid 1970s Manabe and Wetherald (1975), followed by Hansen et al. (1981), and others showed from numerical simulations that increasing CO₂ concentrations will lead to global temperature increases. Later, Santer et al. (1995) showed that global mean temperatures have been well correlated with atmospheric CO₂ concentrations over the last century, meaning that observed temperature increases could be explained simply by physically based radiative balance models. It was then shown that changes in atmospheric CO₂ concentration will eventually have an impact on the total ice contained within the world's cryosphere (Oerlemans 2005).

Knowledge of the potential outcome of the cryosphere under projected climate changes is essential because millions of people rely on snow and ice melt for hydroelectric power and agricultural purposes (IPCC 2007). The cryospheric extent can be viewed as a problem involving a water vapour laden atmosphere and a land surface whose equilibrium temperature is altitude and latitude dependent. Intuition tells us that a temperature increase will lead to a decrease in the extent of glaciers and many past studies have shown this (Schneeberger et al. 2003, Radic and Hock 2006) but it has also been shown that if temperatures increase and changes in relative humidity are small there will be increases in precipitation at midlatitudes (Ingram 2002; Lorenz and DeWeaver 2007), more substantial in locations prone to orographic forcing (Giorgi et al. 1994, Kim et al. 2002). It is then possible that increased melting of glaciers due to warmer temperatures can be offset by increased accumulation of snow at high altitudes. Nevertheless, since 1985 most of the glaciers of Southwestern Alberta and Southeastern British Columbia have undergone significant volume loss, particularly at lower

elevations, under climate change (Schiefer et al. 2007).

Many of the complex interactions between atmosphere and land surface which result in the presence of a glacier (or lack thereof) can be investigated numerically using geophysical fluid dynamics (GFD) models. This study will use computational GFD to analyze the effects of increasing atmospheric CO₂ concentrations on global climate dynamics. This will be done with specific emphasis on changes in the Rocky mountains, since they contain many small and large glaciers as well as extensive icefields, all of importance to Canada. The impact of global warming on the various facets of the general circulation system relevant to Western North America (such as the El Niño Southern Oscillation (ENSO)) will be examined. Changes in the midlatitude jets and their associated cyclogenesis, the location and strength of orographic uplift, and the moisture content of airflows traversing the mountains will also be examined.

The remainder of this chapter is structured as follows. Section 2 details the model setup. Section 3a examines the changes in global climate, with emphasis on circulation patterns, ENSO, temperatures, precipitation, and clouds. Section 3b presents temperature and precipitation results specifically relevant to Western North America. Section 3c contains an analysis of trends in the Rocky mountains through the 21st century, with specific emphasis on regional scale changes in water vapour availability and orographic uplift. Section 4 contains a discussion of results pertinent to the extent of Rocky mountain glaciers. Conclusions are presented in section 5.

2: Model Setup and Intergovernmental Panel on Climate Change (IPCC) forcing

A global atmospheric general circulation model is dynamically and thermodynamically coupled with a global ocean general circulation model. The atmospheric component (Gordon and Stern 1982), developed at the Geophysical Fluid Dynamics Laboratory in Princeton (GFDL), is a spectral model with rhomboidal

truncation at 30 zonal waves. This gives the model an equivalent spatial resolution of 3.75° longitude \times 2.25° latitude (at the equator). The model contains 14 terrain-following sigma levels with the lowest sigma level approximately 30 m above ground in a standard atmosphere. For the ocean, the Modular Ocean Model version 2 (e.g., Pacanowski 1995) is implemented with a spatial resolution comparable to the atmospheric model. The two general circulation models exchange boundary condition information at 1-day intervals. Large ice sheets such as those of Greenland and Antarctica have a fixed albedo of 0.6 and their areal extent and elevation is constant during model integration. Precipitation is determined to be snow if the temperature at a height of 350 m above ground is below freezing. The albedo of snow covered grid cells depends on surface temperature and snow depth, with snow depth determined by surface hydrology. (See Manabe (1969) for further details.)

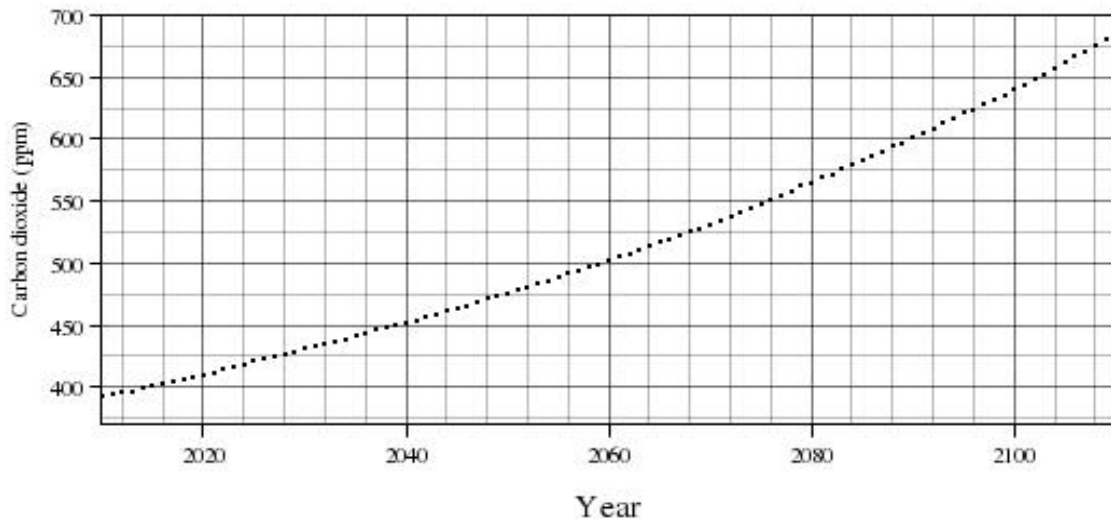


Figure 1: IPCC SRES upper B2 estimates of global atmospheric carbon dioxide concentration (in parts per million by volume) as a function of time.

Two global model integrations were performed. The first, starting from 2007 and ending in the year 2110, has carbon dioxide concentrations in the model atmosphere set to fit the IS92a-Fr-Central emission scenario, close to the upper B2 family estimates from

the Special Report on Emission Scenarios. In this scenario the global mean emission rate of CO₂ increases roughly linearly through the 21st century, bringing the atmospheric CO₂ concentration to almost 690 ppmv by the year 2110 (Fig. 1). The second integration is a 28 year control simulation with CO₂ concentrations set to modern values of 387 ppmv.

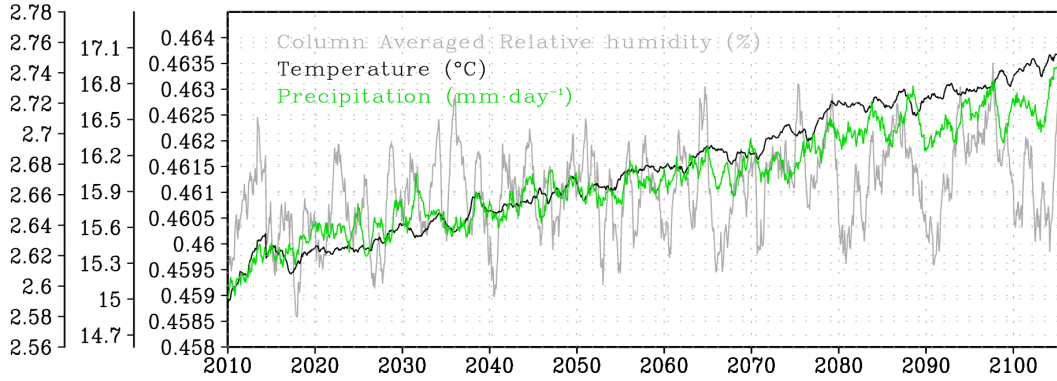
3: Results and Analysis

The model integration was performed using a Silicon Graphics Origin 2400. The integration requires about 16 hours of CPU time per year to run with two processors (beyond which the model does not scale well). Model atmosphere and ocean output requires about 21.6 megabytes per output time slice. The raw monthly mean output over the 131 years of integration requires about 34 gigabytes of storage space. In addition, 55 years of daily output are required for the second chapter of this study, requiring another 440 gigabytes of storage space.

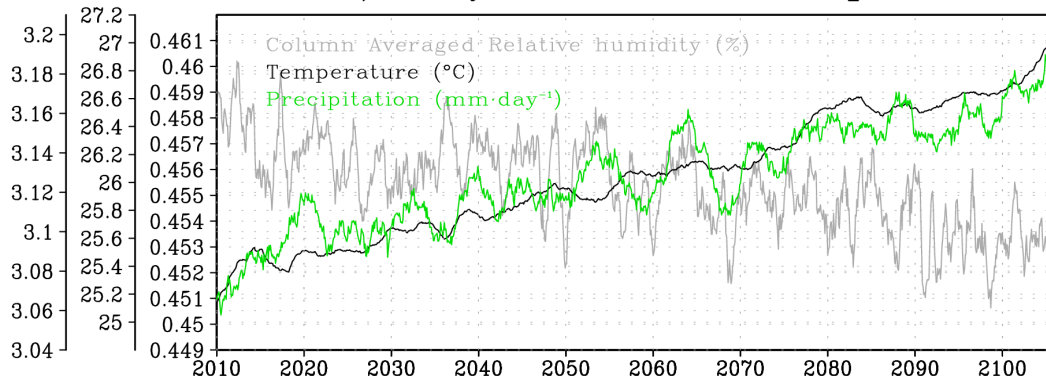
3a: Trends in global climate

A steady increase of global average surface temperature from 288.0 K to 290.0 K is simulated (Fig. 2a) as is an increase in global average precipitation from about 0.260 cm/day to 0.273 cm/day (a 5% increase) between 2010 and 2110. Trends in global precipitation are a consequence of temperature increases, and the lack of equivalent percentage changes in atmospheric relative humidity (Figs. 2a-b). At the mid and high latitudes, surface temperatures increase by approximately 2.1 degrees from 278.8 K and precipitation increases by roughly 0.008 cm/day from 0.119 cm/day over the 100 year interval (Fig. 2c). Precipitation amounts increase by 4% in the tropics and by 7% in the mid and high latitudes, a significantly larger increase, consistent with the higher amplitude warming at mid and high latitudes (Fig 2c). These precipitation increases are roughly proportional to surface temperature increases (Figs. 2a-c), consistent with the

a) 1-year mean, Global



b) 3-year mean, Tropics



c) 3-year mean, Mid & High latitudes

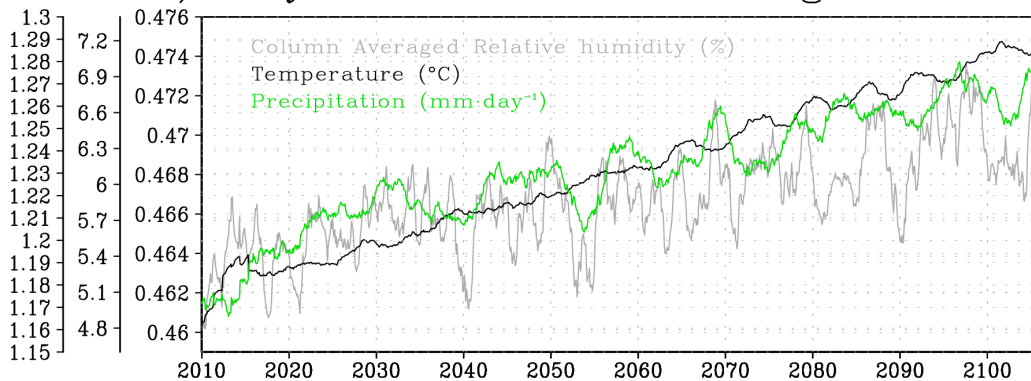


Figure 2: Areal averaged time series from the transient CO₂ simulation. a) 1-year running mean of surface temperature, precipitation, and column averaged relative humidity averaged over the planet. b) As in b but for the 3-year running mean averaged over the tropics, 30°S-30°N. c) As in b but for the 3-year running mean averaged over the mid and high latitudes, 90°S-30°S and 30°N-90°N.

idea that a temperature increase leads to an increase in evaporation and atmospheric water vapour content, with a consequent increase in precipitation (Lorenz and DeWeaver 2007). The precipitation increase presented here is much larger than the observed global increase of ~1-2.5% during the 20th century (Dai et al. 1997). Temperature and precipitation also show strong latitudinal variability in the simulated warming atmosphere (Figs. 3a and 3c). Precipitation increases occur in the intertropical convergence zone (ITCZ) and at midlatitudes, but the largest long term increase occurs at high latitudes polewards of 75°N/S (Fig. 3c).

Most of the largest temperature increases are initially confined to latitudes greater than 60°N by 2025, but spread to the midlatitudes, the tropics, and the Southern hemisphere by 2060 (Fig. 3a). Temperatures increase by up to 2 degrees in the tropics and by up to 3.5 degrees in the Arctic by the end of the 21st century (Fig. 3a). As in previous simulations (e.g. Holland and Bitz 2003), there is higher amplitude warming near the North and South poles, caused by a reduction in sea-ice and snow cover and the impact of this on surface temperatures through the ice/snow-albedo feedback mechanism. The Southern hemisphere is less sensitive to the change in radiative forcing than the Northern hemisphere. Specifically, temperature increases in the Southern hemisphere lag those of the Northern hemisphere by about 20 years through the 21st century (Figs. 3a). This occurs for two reasons. First, the world's surface oceans take centuries to reach full thermal equilibrium after solar/terrestrial radiative balance is altered (Manabe and Stouffer 1994, Stouffer 2004), and the Southern hemisphere oceans cover more area than those of the Northern hemisphere. Second, the Southern hemisphere contains the continental ice sheets of Antarctica, which, in the model, do not respond to the simulated increases in temperature.

The strongest midlatitude zonal winds shift meridionally as the position of the midlatitude temperature front shifts and there is a distinct North-South oscillation in the

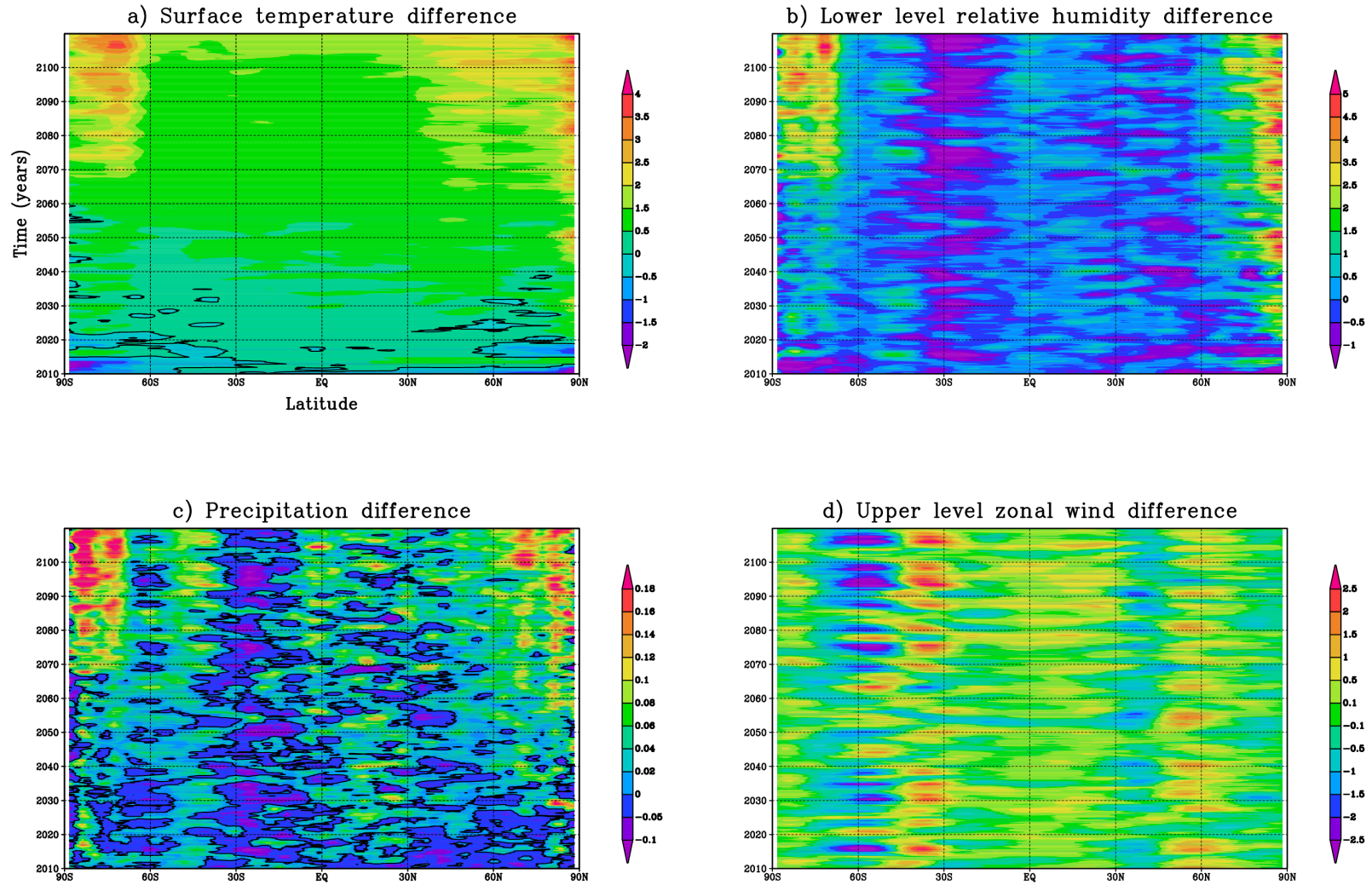


Figure 3: The zonally averaged 2-year running mean of the transient CO_2 run minus the mean of the control run. a) The surface temperature difference ($^{\circ}\text{C}$). b) The lower level absolute relative humidity difference. c) The percentage change in precipitation. d) Upper level zonal winds (m/s). *Lower level denotes an average over the lowest 5 σ -levels ($\sigma = 0.99665 - 0.77695$) and upper level denotes the 7 σ -levels above lower level ($\sigma = 0.77695 - 0.17065$).

position of both midlatitude jets (Fig. 3d). This suggests fluctuations associated with the Northern and Southern Annular Modes (NAM/SAM) (Thompson and Wallace 1998, Thompson and Wallace 2001, Cash et al. 2004) and indicates that the effects of SAM oscillation increases in a warmer climate (Fig. 3d). Despite the variability, decreases in the strength of both the Northern and Southern midlatitude jets and the Easterly trade winds of the ITCZ are simulated (Fig. 3d). The former is consistent with the fact that the Arctic and Antarctic regions exhibit the largest temperature increases, reducing latitudinal temperature gradients, thereby reducing the zonal wind strength in the upper troposphere through thermal wind balance.

Lower level relative humidity increases by almost 4% in polar regions by 2100 (Fig. 3b), although any significant long term changes in this quantity at other latitudes are small and more difficult to quantify. The timing of increases in relative humidity around 2030 in the Arctic and in 2065 in the Antarctic coincides with the largest temperature increases in those regions (cf. Fig. 3a). This illustrates that although changes in relative humidity are small, long term changes in mean temperature and relative humidities are well correlated. Given the large temperature increases (cf. Fig. 3a) and the fact that relative humidity changes are small explains the precipitation increases (cf. Fig. 3c).

Vertical motion in the atmosphere generally results from three distinct processes: baroclinic instability, convection, or orographic uplift, all three of which can occur either independently or simultaneously, depending on the state of the atmosphere. Therefore, the effects of these processes are cumulative and the relative fraction of each that influences total precipitation depends on the region of interest and the mean climate state. It follows that the global mean increase in precipitation (cf. Figs. 2a-c, 3c), is mostly the result of either convective or baroclinic processes and not orographic processes, because mountain ranges cover a small fraction of the globe. If relative humidities do not change much, as simulated, mountainous regions should experience substantially larger increases

in total precipitation than the global mean increases. The controls on orographic precipitation over Western Canada will be treated in greater detail in section 3c.

Temperature increases are greatest at lower levels in polar regions, with the magnitude of temperature increases generally decreasing with altitude (Fig. 4a). In contrast, tropical temperature increases are greatest in the upper half of the troposphere (Fig. 4a), caused by increased latent heating in the moister ITCZ. The large scale temperature changes lead to weakened midlatitude jets, consistent with Giorgi et al. (1992), who found a decrease in zonal wind strength over Europe in a doubled CO₂ atmosphere. Furthermore, weakened tropical Easterly trade winds are consistent with the results of the doubled CO₂ atmosphere of Bush (2007) and with observations over the past 50 years (Vecchi et al. 2006). In both hemispheres there is a poleward shift in the mean position of the midlatitude jet in addition to a general weakening (Fig. 4b), in general agreement with the transient CO₂ simulations of Rinke and Dethloff (2008), who found signs of a Northward shifting midlatitude jet over the Northern hemisphere. However the magnitude of each of these changes is different between the two hemispheres. In particular, the Northern hemisphere jet is primarily weakened with a small displacement, whereas the Southern hemisphere jet is shifted polewards significantly with a small weakening (Fig. 4b). The latter result is a consequence of the static nature of the model's Antarctic ice sheet in the simulation. Temperatures rise more in areas surrounding Antarctica than over the continent itself (cf. Fig. 3a), whereas the Arctic experiences its highest amplitude warming at the pole (cf. Fig. 3a) where there is only ocean and sea ice. These differences cause hemisphere-dependent changes in the midlatitude temperature front, leading to the different changes in the Northern and Southern hemisphere midlatitude jets.

Simulated zonal mean specific humidity increases substantially (Fig. 4c), especially at higher latitudes, with 50-year increases of up to 5% in the tropics and up to

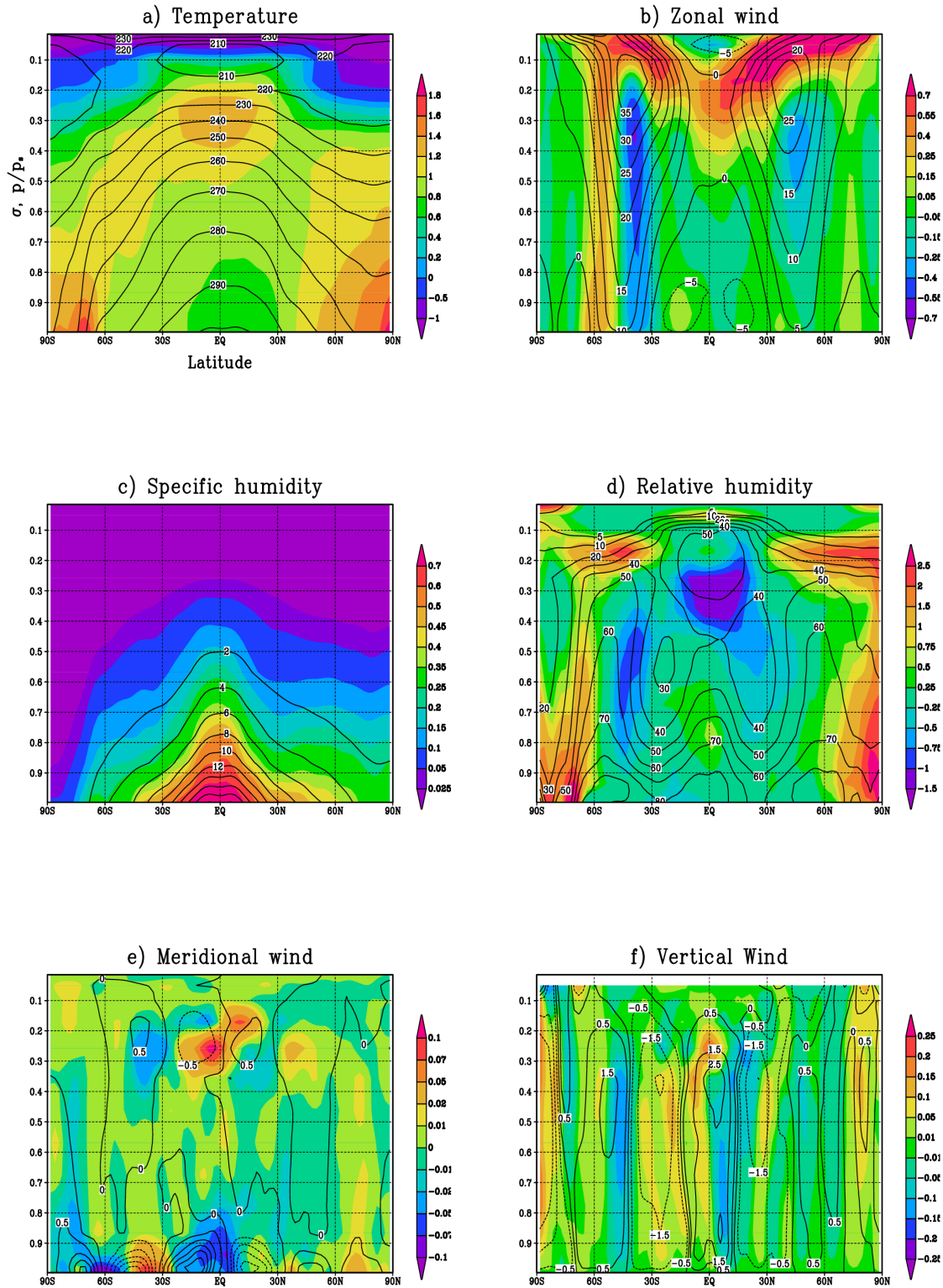


Figure 4: The zonally averaged 2061-2089 mean minus the zonally averaged 2011-2039 mean for a) temperature ($^{\circ}\text{C}$), b) zonal winds (m/s), c) mixing ratio (g/kg), d) relative humidity, e) meridional winds (m/s), f) vertical winds (cm/s). Solid contours show the 2011-2039 means for reference.

15% in the mid and high latitudes. This result is consistent with the trend of observed increases since 1958 (Ross and Elliot 2001), and can be attributed to the fact that additional radiative heating of the Earth's surface tends to be manifested in the latent heat fluxes as opposed to the sensible heat fluxes (Manabe and Wetherald 1975, Wetherald and Manabe 2003, Held and Soden 2006). The increase in vapour content is related to the temperature increase such that the global mean change in relative humidity is small (Ingram 2002). Nevertheless, zonal mean relative humidity does evolve in an increasing CO₂ atmosphere. A decrease of about 1 percentage point is evident through most of the subtropical atmospheric column. In contrast, relative humidity increases slightly at upper levels in the ITCZ and more substantially at higher latitudes (Fig. 4d), with the high latitudes experiencing the most pronounced changes (Fig. 4d). These results (i.e. decreases in midlatitude jet strength and increases in specific humidity with relative humidity remaining fairly close to unchanged) have important implications for orographically forced precipitation amounts, described in section 3c.

In addition to the zonal winds (cf. Fig. 4b), meridional (cf. Fig. 4e) and vertical (cf. Fig. 4f) winds are also reduced in a warmer climate, particularly in the tropics, consistent with an overall weakening of the large scale circulation patterns. Unlike in the tropics however, surface mass transport increases substantially poleward of 60° (Fig. 4e), as does vertical lifting (Fig. 4f) and the westerly winds (cf. Fig. 4b). This is partially in response to the high latitude surface warming (cf. Figs. 3a and 4a) and the conversion of added latent heat (cf. Figs. 4c and 4d) into wind energy and partially in response to the poleward shifted midlatitude jets (cf. Fig. 4b).

A measure of the amount of baroclinic activity present can be obtained through the use of the Eliassen-Palm flux vector, plotted in the vertical and meridional directions. The vertical component of the Eliassen-Palm flux vector is proportional to the scaled meridional eddy heat flux, $v'T'$, and the horizontal component, the scaled meridional eddy

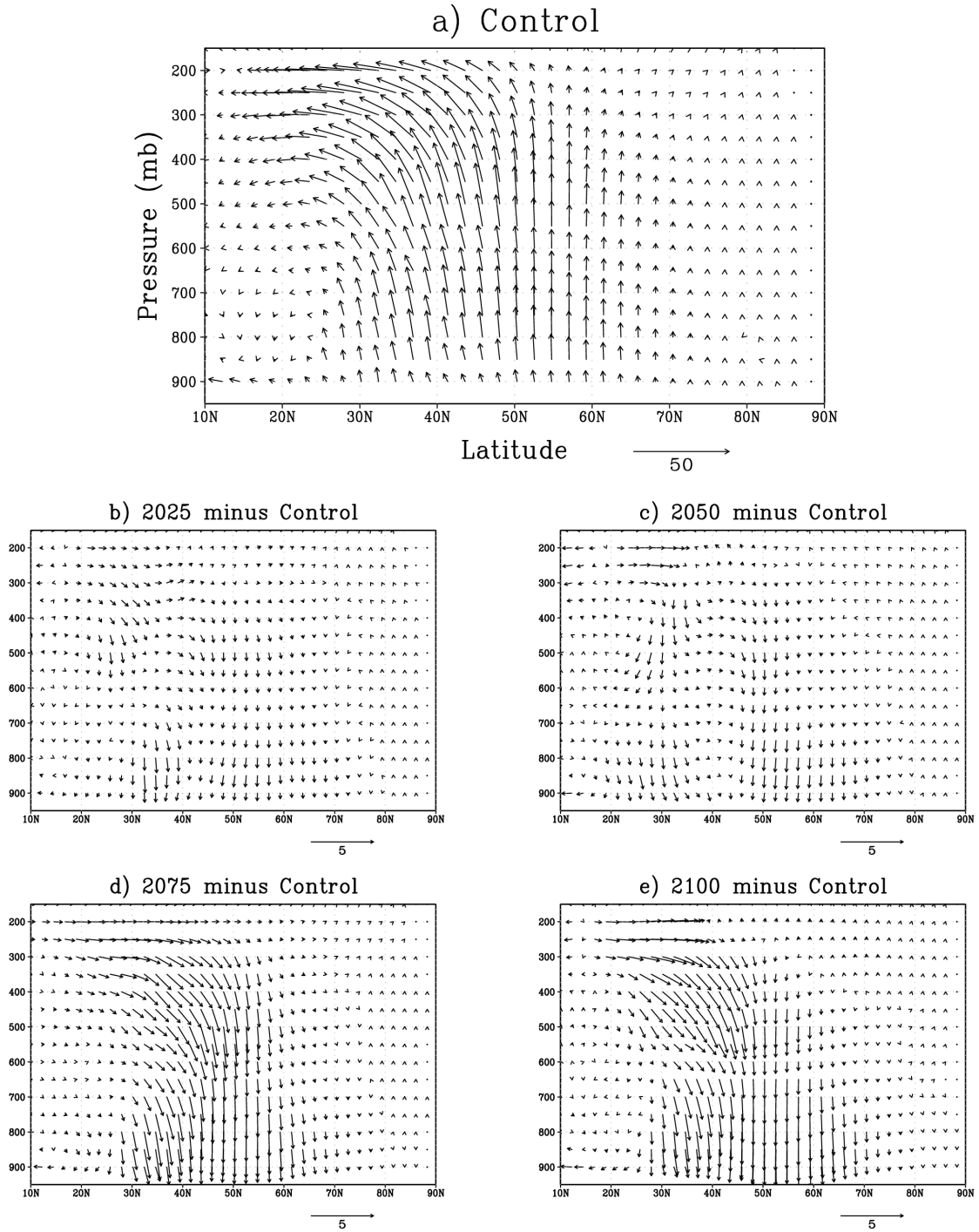


Figure 5: The 10-year Eliassen-Palm flux vectors for a) the Control simulation years 15-24. b) The increasing CO₂ simulation years 2020-2029 minus a. c) As in b but for the years 2046-2055. d) As in b but for the years 2070-2079. e) As in b but for the years 2090-2099.

momentum flux, $u'v'$. Although baroclinic events of a warmer climate are less frequent, they have also been shown to cover a greater latitudinal extent (Bush and Peltier 1994), and contain more energy through latent heat release (Geng and Sugi 2003). Eddy momentum and heat flux generally decrease through the 100 year period, with a more rapid decrease between 2050 and 2075 (Figs. 5b-c). The global increase in precipitation (Figs. 2-bd, 3c) must therefore be explained largely by increases in convective activity, and not baroclinic activity. However, convection is often found in the vicinity of frontal zones associated with baroclinic activity so the role of baroclinic eddies in delivering precipitation at midlatitudes will remain paramount in a warmer climate. Total baroclinic instability associated with the midlatitude jet decreases substantially in a warmer climate, with up to 20% less over the midlatitudes by 2100 (Figs. 5e). In light of these results (Fig. 5d-e), precipitation increases during the 21st century (cf. Fig. 3c) are due to the moister atmosphere (cf. Fig. 4c-d) and increased convection, with baroclinic activity being less important in delivering precipitation to the midlatitudes.

The amplitude of the Hadley circulation gradually decreases as the simulation progresses towards 2110 (Figs. 6b-e), indicating that the observed trend in weakening tropical circulation (Zhang et al. 2006; Vecchi et al. 2006) are likely to continue into the 21st century. A weakening meridional circulation has been suggested to be a necessary consequence of a moister atmosphere, as latent heat fluxes begin to assume a larger role in planetary scale heat transport (Lorenz and DeWeaver 2007). There is also a poleward shift in the position of the Ferrel cells which results in more uplift at high latitudes (Fig. 6b-e). This is consistent with the poleward shift in the midlatitude jet and associated baroclinic activity (Rinke and Dethloff 2008). In polar regions, the effect of substantially increased temperatures and mixing ratios (cf. Fig. 4a, 4c and 4d) combined with increased circulation (Fig. 6b-e) is to increase precipitation substantially more than over most other regions of the planet (cf. Fig. 3c), where relative humidities stay relatively

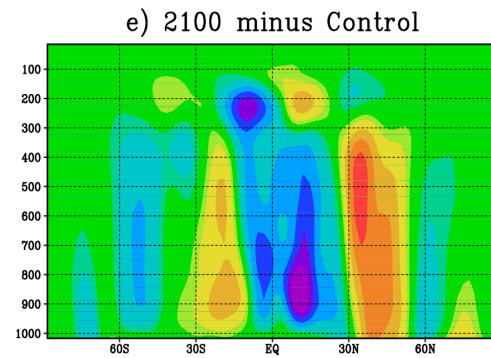
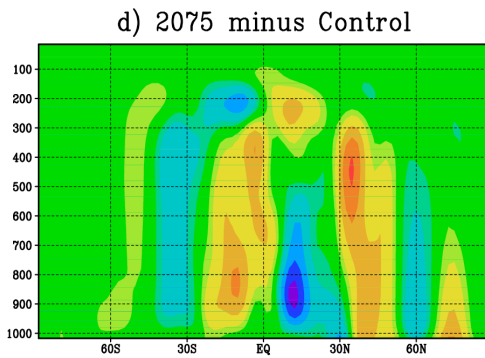
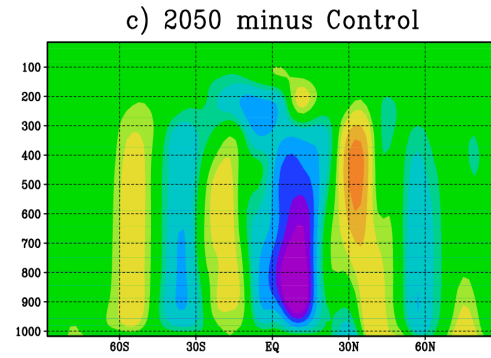
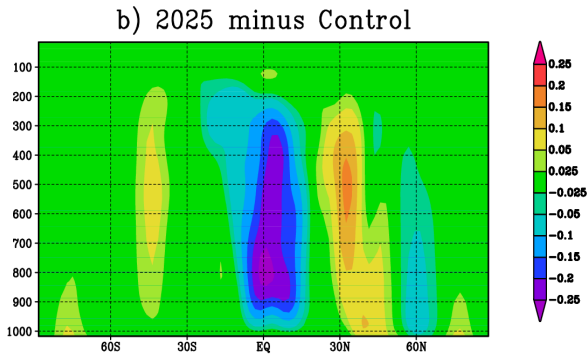
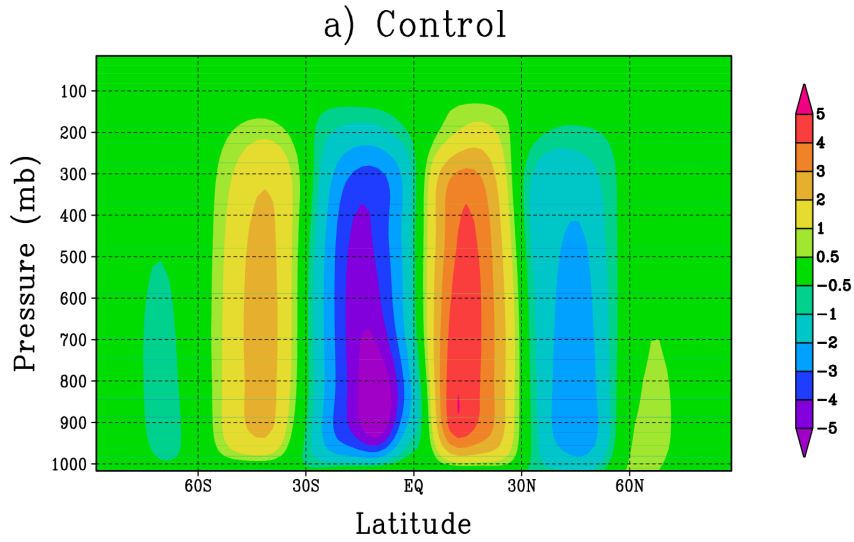


Figure 6: The Mean Meridional mass stream function ($\times 10^{10} \text{ kg s}^{-1}$) for a) the years 5 – 27 of the transient CO_2 run. b) The mean of the years 14 – 2036 of the transient CO_2 run minus a. c) As in b but for the years 2038 – 2060. d) As in b but for the years 2064 – 2086. e) As in b but for the years 2087 – 2109.

constant and meridional circulation weakens (cf. Figs. 3c, 6b-e). The weakened Hadley circulation thus counter-acts the effects of increasing specific humidity on tropical and subtropical precipitation. In addition, it limits the ability of the atmosphere to transmit anomalous tropical conditions to higher latitudes.

Sea surface temperatures in the Niño 3.4 region of the equatorial Pacific Ocean gradually increase, leading to a more El Niño-like mean state by 2100 (Fig. 7), consistent with long term temperature increases (cf. Fig. 2b). Despite the evolving mean state of the equatorial Pacific, the frequency of actual El-Niño events decreases in the warmer climate, as has been seen in simulations with doubled (Bush 2007) and increasing CO₂ concentrations (Boer et al. 2004). A gradual warming of the global oceans under increasing CO₂ concentrations has also been shown in other past studies (Manabe and Stouffer 1994, Stouffer 2004). ENSO's teleconnection patterns are calculated for the

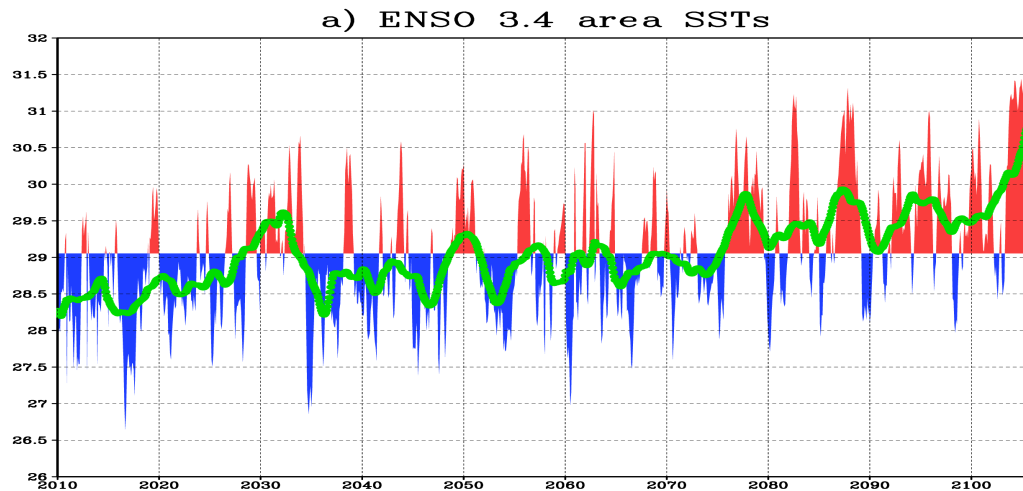


Figure 7: Areal averaged time series from the transient CO₂ simulation. a) Sea surface temperatures (°C) averaged over 170°W-120°W,5°S-5°N (the Niño 3.4 region). Blue/Red denotes below/above long term mean. Green is the 4-year mean running mean.

years 2014-2059 and for the years 2060-2105 of the increasing CO₂ run using the Niño 3.4 index to define ENSO (Trenberth 1997). Anomaly differences are defined with respect to the 11 year centered running mean of the month in question to filter out the effects of long term increases in sea surface temperatures on the teleconnection signal.

The temperature and sea level pressure teleconnection patterns simulated in the first fifty

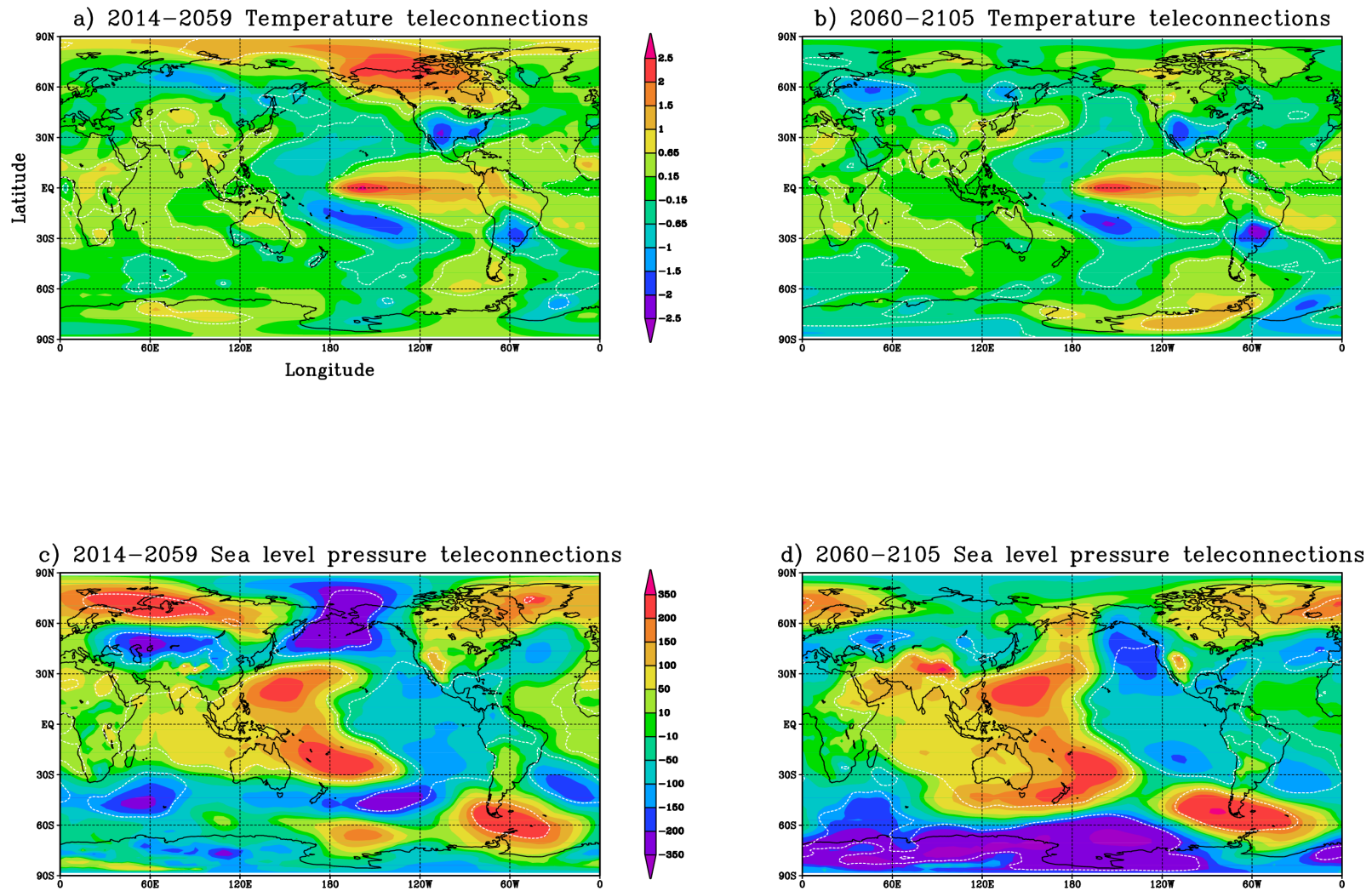


Figure 8: ENSO's teleconnections and changes in teleconnections. a) The surface temperature teleconnections calculated from the years 2014-2059. b) The surface temperature teleconnections calculated from 2060-2105 minus a. c) The sea level pressure teleconnections calculated from the years 2014-2059. d) The sea level pressure teleconnections calculated from 2060-2105 minus c. The dashed contours indicate where a Student's t-test results indicate that teleconnection patterns are statistically significant within the 95% confidence interval.

years of the model run (Figs. 8a and 8c) are very similar to observations with a significant warming in Northwestern North America, cooling over Northern Eurasia and the North Atlantic, and a strengthened Aleutian low during El Niño events (Horel and Wallace 1980).

Many of ENSO's Northern hemisphere teleconnections weaken in the 2nd half of the 21st century. A Student's t-test reveals that ENSO's teleconnection patterns are no longer statistically significant in Northern high latitudes in the second half of the 21st century (cf. Figs. 8a-d). In particular, the observed increase in surface temperatures over Northern North America and the strengthened Aleutian low experienced during El Niño events become less statistically significant in the second half of the 21st century (Figs. 8b and 8d). ENSO therefore exerts less influence on the the mean state of North America and all of the Northern high latitudes in a warmer climate, consistent with the findings of Meehl et al. (2006) and Meehl and Teng (2007). The reverse is true over Antarctica, which experiences more statistically significant reductions in sea-level pressure during El Niño events of the future. The differing patterns of ENSO teleconnections in opposing hemispheres in a warmer climate are related to the model's Antarctic ice sheet and Southern oceans, the simulated warming patterns (cf. Fig. 3a, 4a), and ultimately the weakening zonal winds and Hadley circulation (cf. Figs. 3d, 4b, 5b-e).

In general, polar surface temperatures increase more than tropical surface temperatures (cf. Figs. 3a and 4a) because of the ice and snow albedo feedback mechanism. This causes the strength of the zonal winds to decrease in both hemispheres (although there is hemispheric asymmetry) through thermal wind balance (cf. Figs. 3d and 4b). In addition to decreases in zonal wind strength, the strength of the meridional circulation also decreases, largely in response to the presence of more water vapour (cf. Fig. 6) and enhanced meridional latent heat flux. This decrease in the mechanical efficiency of meridional heat transport in the atmosphere is balanced by an increase in

the strength of the hydrological cycle (Lorenz and DeWeaver 2007) which increases the efficiency of atmospheric meridional heat transport. These changes are shown to ultimately have an impact on the ENSO, reducing the spatial extent of teleconnection patterns over Northern high latitudes (cf. Fig. 8b and 8d).

3b: Trends in Rocky Mountain Climate

Annual mean temperatures over Eastern North America increase by over 2.4 degrees by 2100 (Fig. 9e), and by just over 1 degree over the Pacific Ocean, with the magnitude of the temperature change generally increasing towards the East over the continental interior. Annual mean temperatures over the Rockies increase by 1.8 to 2.1 degrees, substantially larger than the observed increase of about 1 degree over Western Canada since 1900 (Zhang et al. 2000). Because of the prevailing Westerlies in the region, warming patterns reflect the fact that the oceans respond to changes in radiative forcing relatively slowly (Manabe and Stouffer 1994, Stouffer 2004), limiting the warming of the maritime atmosphere. In contrast, continental air masses respond more rapidly to changes in radiative forcing, leading to a higher amplitude continental warming (Hansen et al. 1984).

Geopotential heights generally increase (a necessary consequence of the overall warming trend), with greater increases over Eastern North America and the Northwest Pacific. Changes in geopotential height are shown to be directly proportional to changes in temperature, with larger increases over the Arctic and Eastern North America and smaller increases over the North Pacific (Figs. 9b-e). Changes in geopotential height are also indicative of changes in the upper level winds; a weakening meridional geopotential height gradient (Fig. 9b-e) is consistent with a decrease in the strength of the midlatitude jet (cf. Fig. 4b).

By 2100, surface temperatures increase by over 3 degrees over Eastern North

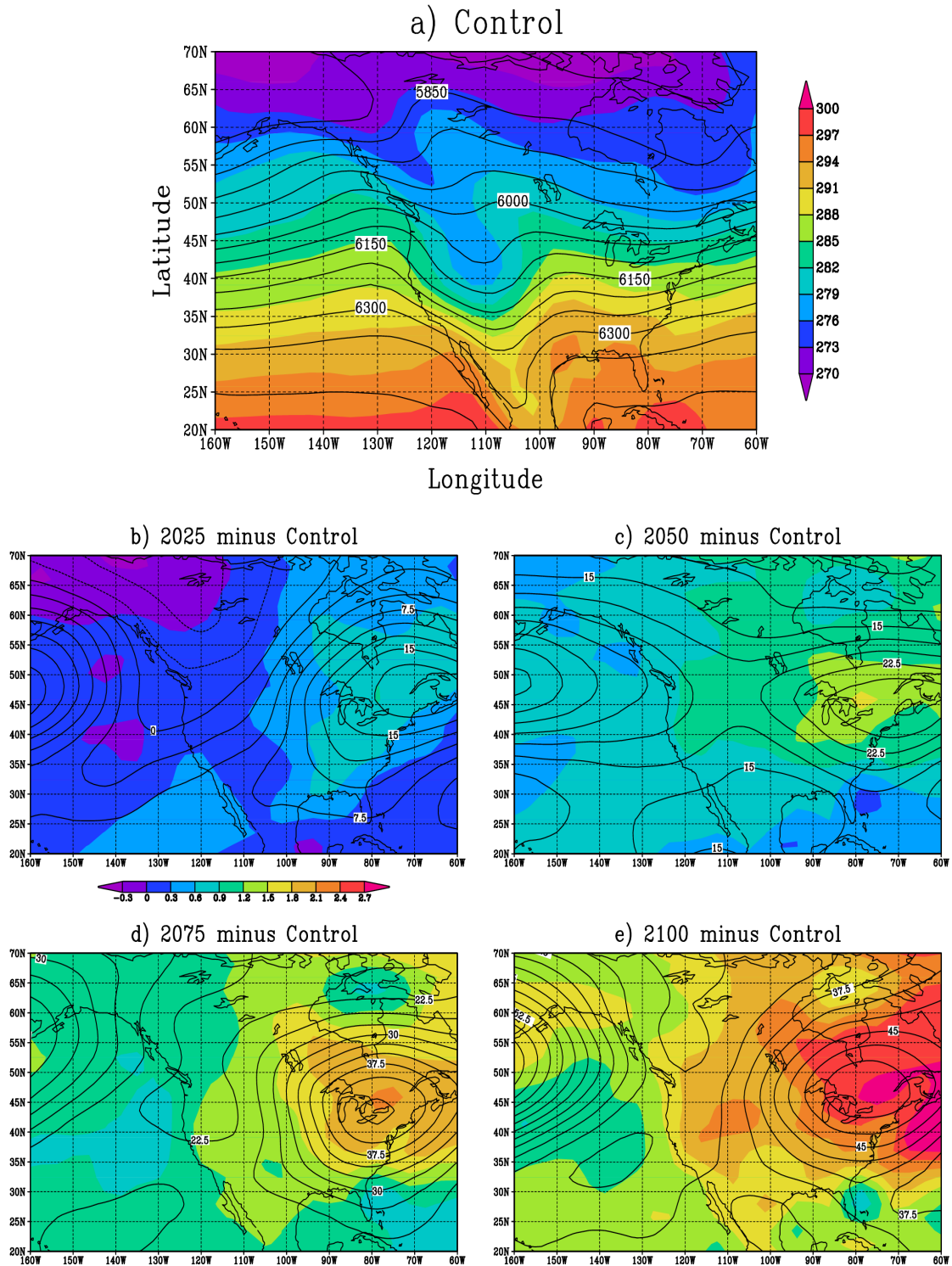


Figure 9: The mean surface temperature (K) and 500mb Geopotential height (m) for a) the years 5 – 27 of the control run. b) The mean of the years 2014 – 2036 of the transient CO₂ run minus a. c) As in b but for the years 2038 – 2060. d) As in b but for the years 2064 – 2086. e) As in b but for the years 2087 – 2109. Shaded represents surface temperature and solid contours show geopotential height.

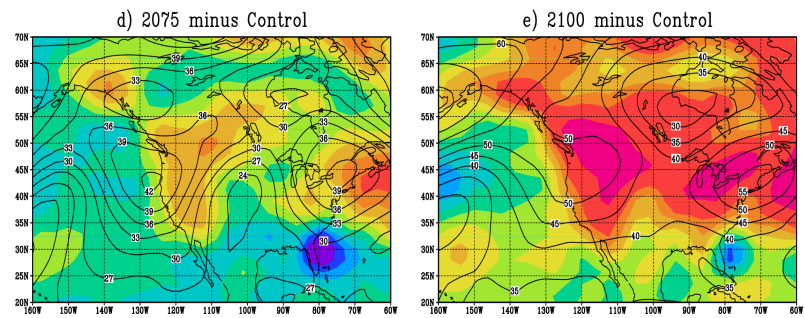
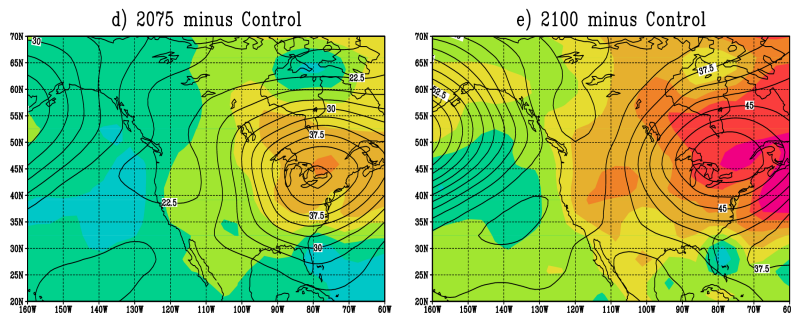
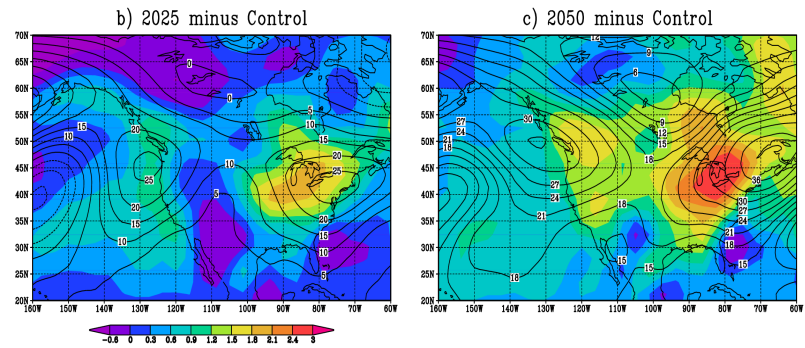
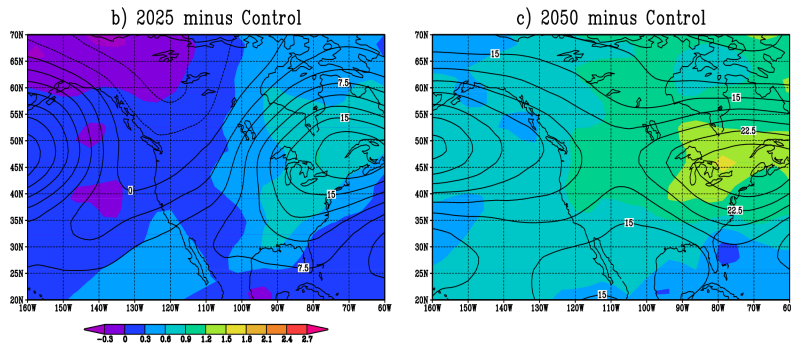
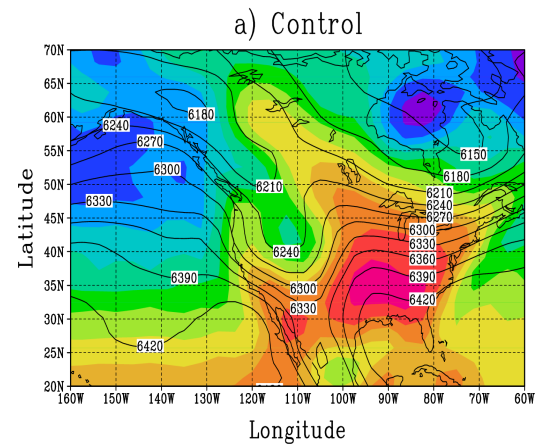
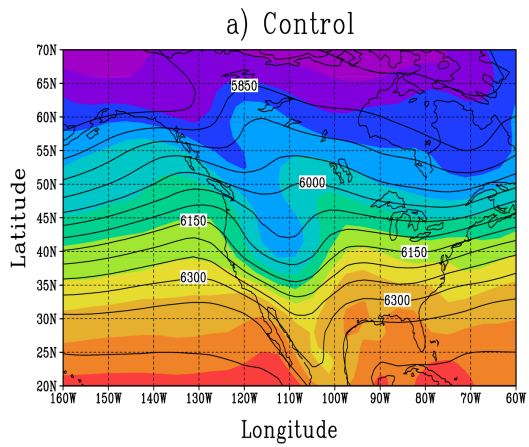


Figure 10: As in Fig. 9 but for the months of January only.

Figure 11: As in Fig. 9 but for the months of July only.

America during July (Fig. 11e) and by 2 degrees over the same region during January (Fig. 10e). The higher amplitude summer warming, is consistent with Manabe et al. (1992) and is explained by the weakening of the summer westerly jet, which allows air masses to reside over the continents for longer periods combined with the fact that continental air masses respond to anomalous radiative forcing more rapidly than do maritime ones. As a result, the warming signal over Eastern North America is displaced further East and reduced because of the increased strength of the prevailing Westerlies during the winter months.

Although temperatures are well correlated with summer melt of high altitude snowpack through the positive degree days index (Hock 2003), melt in the Rocky mountains is mostly controlled by incoming solar radiation. An investigation of the effects of a warming climate on cloud cover and incident short wave radiation is therefore necessary in a snow mass balance study of the Rocky mountains. Simulated annual mean Northern hemisphere vertical and latitudinal cloud distribution changes in a warming climate. High clouds thicken and form higher (in pressure coordinates), tropical and midlatitude low and mid-level cloud amounts decrease, and mid-high latitude low cloud amounts increase (Figs. 12a-b). Although changes in high cloud are independent of season, this is not the case for middle and low clouds. During the winter, low clouds increase North of 50°N and middle clouds increase North of 60°N . In contrast, during the summer mid-level clouds decrease over all of the mid and high latitudes and low clouds increase only North of 60°N , with a upward shift in altitude. The simulated changes during the summer and during the annual mean are consistent with the findings of Hansen et al. (1984) and Dai et al. (2001), with an overall upward shift in the cloud base and a reduction of low and mid-level clouds.

The increase in high cloud altitude and high cloud amounts are consequences of the atmospheric temperature and specific humidity increases (cf. Figs. 4c, 12b-e), which

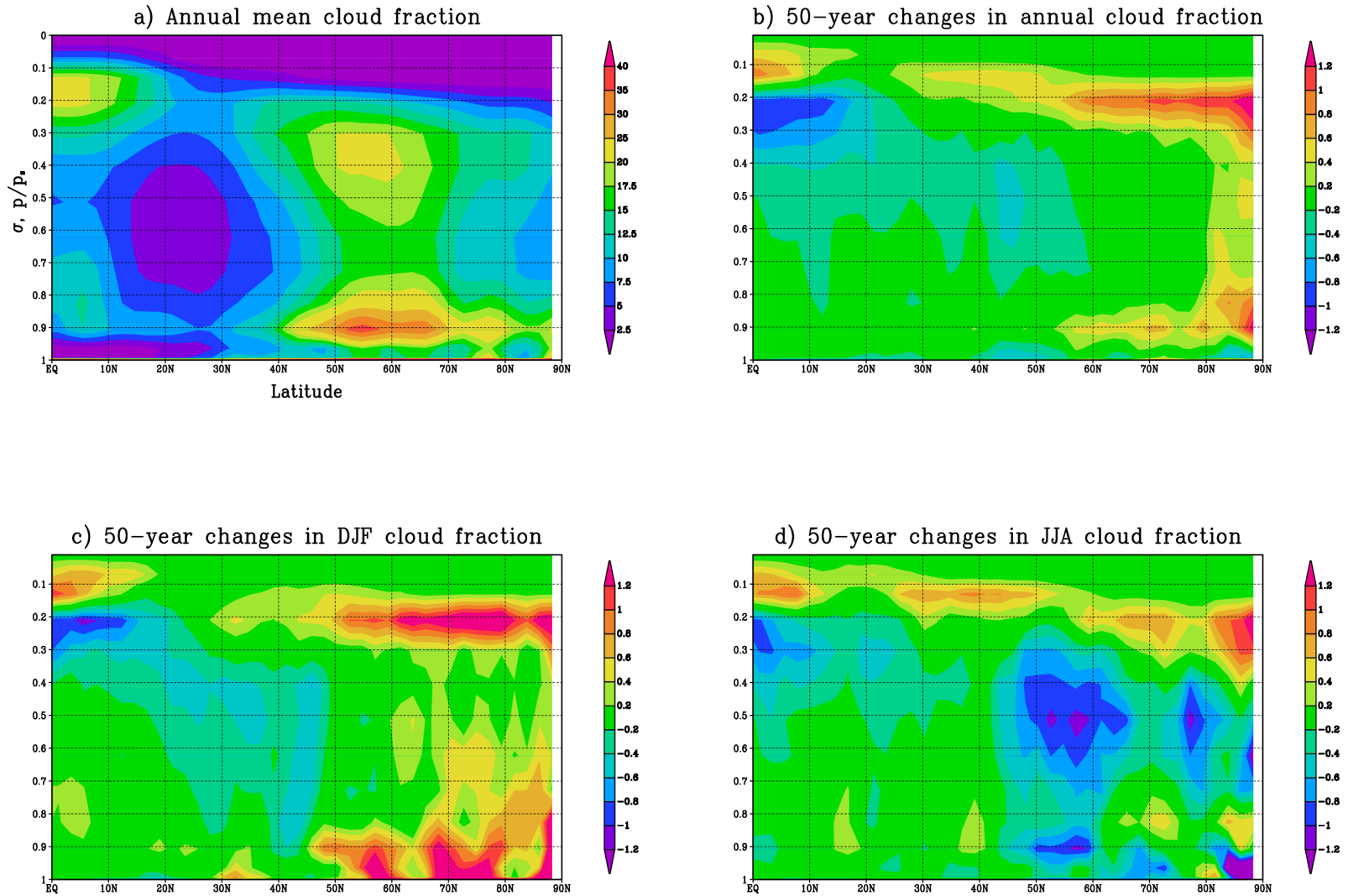


Figure 12: a) The annual mean of the zonally averaged cloud fraction from the years 2011-2039 of the increasing CO_2 simulation. b) The annual mean of the zonally averaged cloud fraction from the years 2061-2089 from the increasing CO_2 simulation minus a. c) As in b but for only the winter months, January, February, and March. d) As in b but for only the summer months, June, July, and August.

lead to increases in latent heat release and moist convection, raising clouds to higher levels. Similar processes result in an upwards shift in low-level clouds in the Arctic. The simulated increases of wintertime middle level cloud amounts at high latitudes is related to the widening and Northward shifting band of influence of midlatitude baroclinic activity associated with the weakened and poleward-shifted midlatitude jet (Rinke and Dethloff 2008, Bush and Peltier 1994) in addition to the increases in atmospheric water vapour (cf. Fig. 4c). In contrast, the decrease in summer mid-level cloud amounts at mid-high latitudes is a consequence of the higher amplitude summer warming (Figs. 12b-12e) and a weakened summertime jet (cf. Figs. 3d and 4b), which reduces orographically forced condensation, baroclinic uplift, and moisture availability over continents.

Low and mid-level cloud has the effect of decreasing the net radiation incident at the surface, since it is a more efficient net reflector of the sun's radiation than high clouds (Hansen et al. 1981). Although simulated mid-level cloud at mid and high latitudes increases during the winter, it decreases during the summer under global warming because the continents are comparatively dry and warm the atmosphere efficiently. The seasonality of these changes makes them a positive feedback for further warming because incoming solar radiation is strongest during the summertime. Furthermore, high clouds are efficient absorbers of the Earth's long wave radiation, implying that a global increase in high cloud is a positive feedback mechanism for further warming.

Although there is some vertical redistribution of clouds in a warmer atmosphere, the annual mean low and mid-level vertically averaged cloud fraction increases in most places (Figs. 13a-b), resulting in a decrease of mean annual short wave radiation in most low elevation and maritime regions (Figs. 13c-d), but particularly over the Eastern slopes of the Rocky mountains. The exception to this is the Western slopes and higher elevations of the Rockies, where decreases in cloud cover are substantial enough to increase solar radiation (Figs. 13b-d). The differing changes in low and middle level

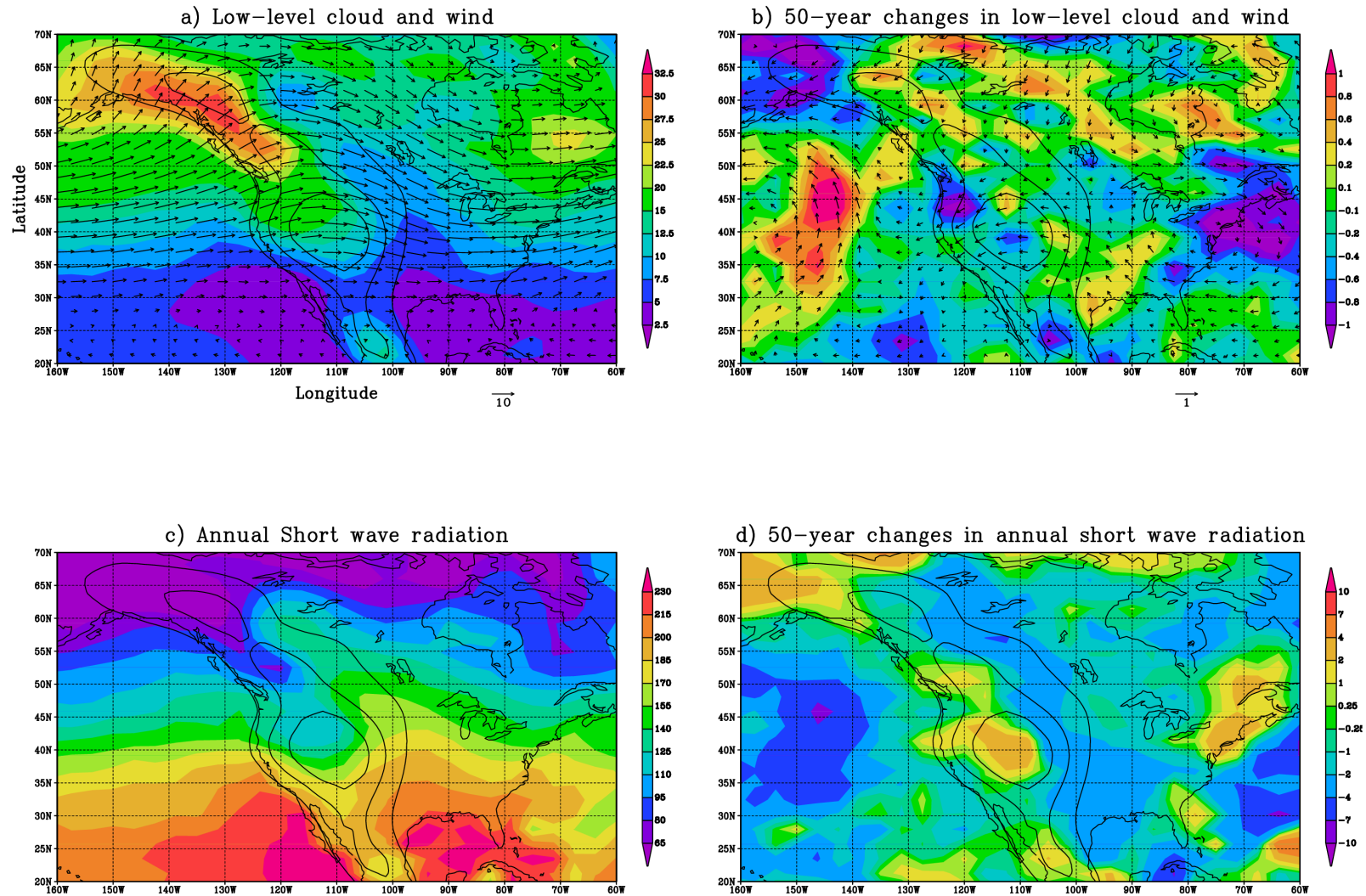


Figure 13: a) The annual mean vertically averaged cloud fraction from the years 2011-2039 of the increasing CO_2 simulation and winds (m/s). b) The annual mean vertically averaged cloud fraction and winds from the years 2061-2089 minus a. c) Annual mean incident short wave radiation at the surface ($W m^{-2}$) from the years 2011-2039 of the increasing CO_2 simulation. d) Annual mean incident short wave radiation at the surface ($W m^{-2}$) from the years 2061-2089 of the increasing CO_2 simulation minus a. The winds and clouds are averaged over the the levels $\sigma = 0.9-0.5$.

cloud and surface short wave radiation amounts on either side of the continental divide are related to the decreasing midlatitude jet strength (cf. Figs. 4b and 13b) and changes in cloud formation by orographic forcing. Nevertheless, overall changes in simulated cloud and surface solar radiation results over the Rockies are indicative of an environment more conducive for snow melt in warmer climate, largely because of the substantial decreases in summertime mid-level clouds (cf. Fig. 12d).

The effects of rising temperatures have been shown to have an effect on incident radiation in the Rocky mountains, the dominant mechanism for melt of high elevation snow and ice. However, the source of snow and ice at high elevation (precipitation) is equally important in the determination of net mass balance. Observations have shown that precipitation in Canada has increased at least 5% since 1900 (Zhang et al. 2000), which compares reasonably well with the increase of almost 7%/century predicted by this model during the (cf. Fig. 3c) next century on considering the fact that global warming is accelerating. The control simulation precipitation and wind patterns are reasonably close to NCEP Reanalysis data (Kalnay et al. 1996) over the West coast of North America (Fig. 14a), with the highest precipitation rates occurring in the regions with the strongest upslope winds (Johansson and Chen 2003). In general, precipitation amounts increase as time progresses, predominantly in the Arctic, Eastern North America, and the West coast. Increases in annual mean precipitation along the West coast are generally larger than the global mean increase of 7%/century (cf. Fig. 2c), however, most of the precipitation over the West coast of North America occurs during the winter months when strong westerlies result in large quantities of orographic precipitation.

January precipitation increases in time, particularly in 2075, when the area receives up to 15% more precipitation than the control simulation (Fig. 15d). There is a simulated increase in orographic precipitation during January over the Rocky mountains despite the decreasing jet strength (cf. Fig. 4b). The West coast experiences simulated

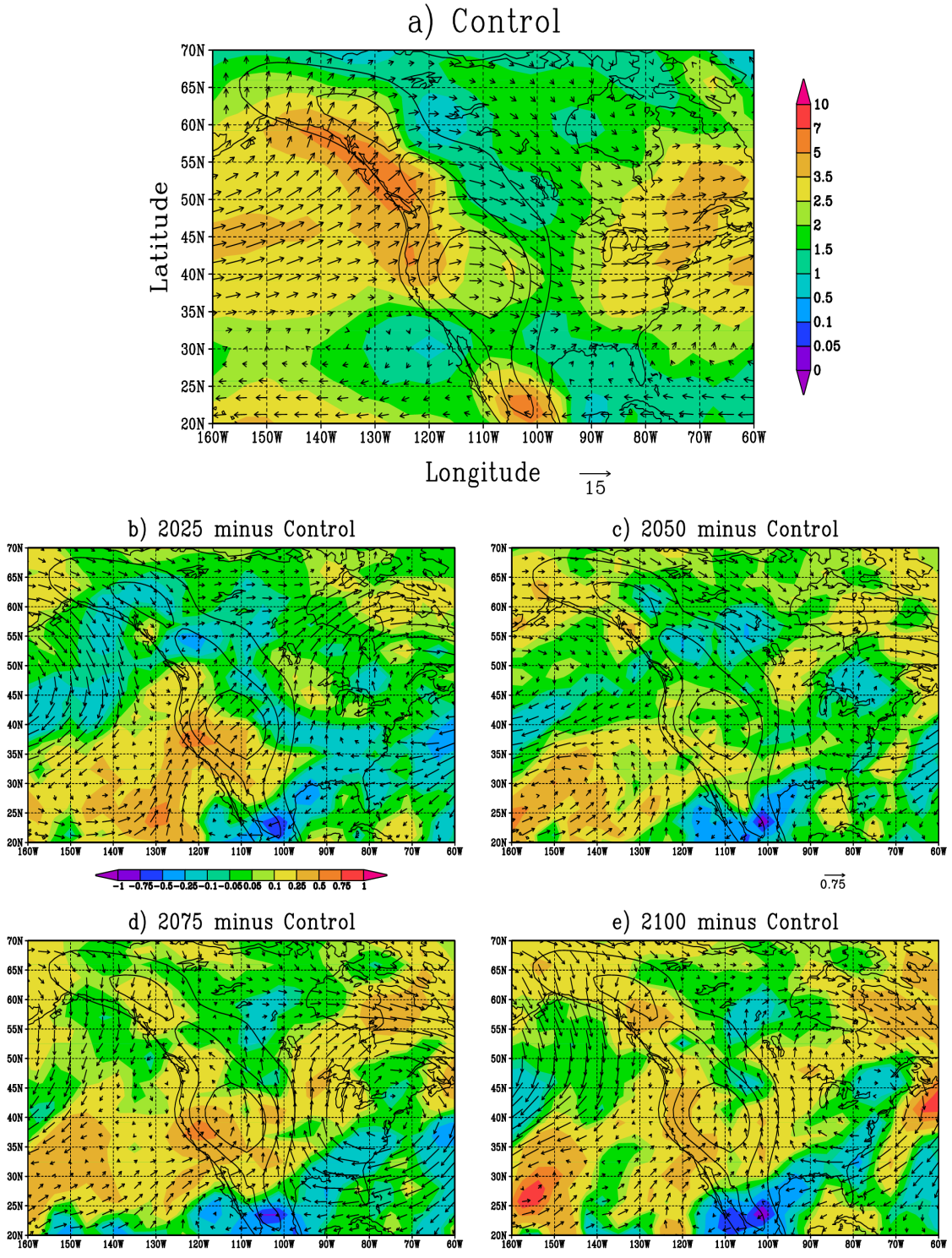


Figure 14: The mean precipitation (mm/day) and lower level winds (m/s) for a) the years 5 – 27 of the control run. b) The mean of the years 2014 – 2036 of the transient CO₂ run minus a. c) As in b but for the years 2038 – 2060. d) As in b but for the years 2064 – 2086. e) As in b but for the years 2087 – 2109. Results are overlaid on 500, 1000 and 1500 m elevation contours for reference. Winds are averaged over lowest 5 σ levels: $\sigma = 0.99665 - 0.77695$.

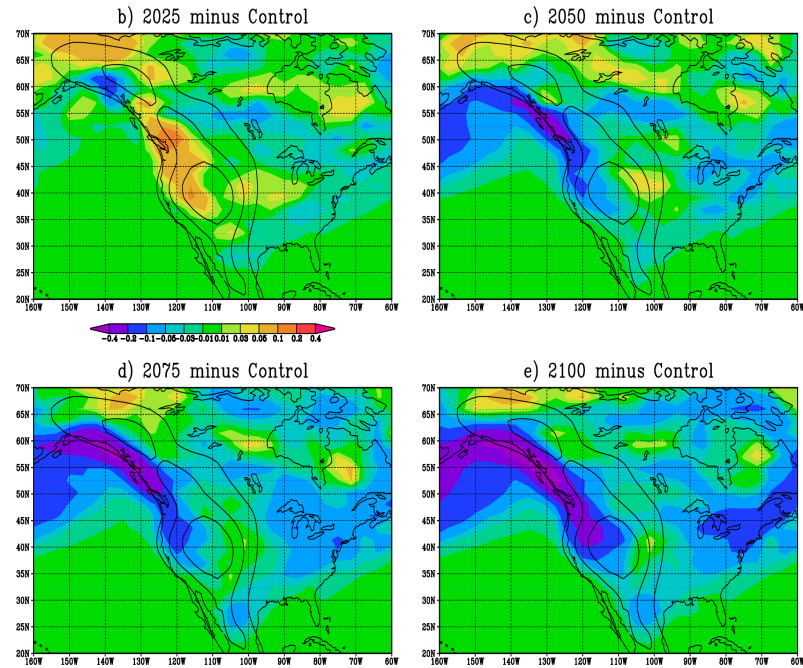
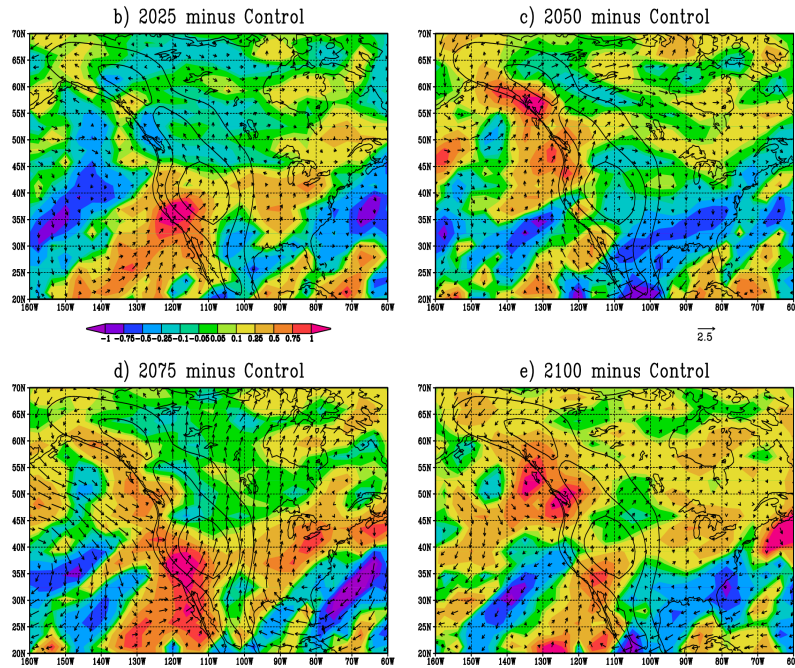
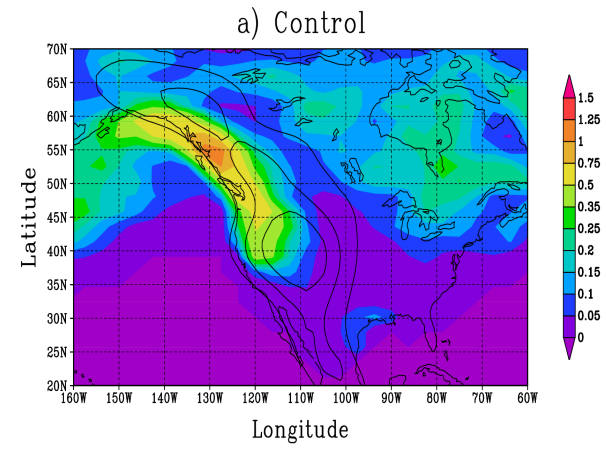
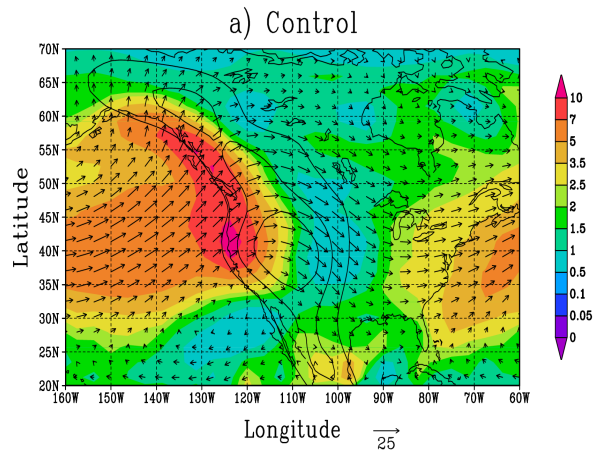


Figure 15: Changes of January mean Precipitation and lower level winds. As in Fig. 13 but for only January.

Figure 16: a) The annual mean snowfall (cm water equivalent). As in Fig. 15 but for snowfall.

January precipitation increases of about 10%/century, larger than the increases of 7%/century predicted by the area-averaged results (cf. Figs. 2d and 3c) and indicative of the fact that regions prone to orographic forcing experience a disproportionate share of the global mean precipitation increase.

Annual mean snowfall is highest over the Northwestern Coast of North America and in Quebec (Fig. 16a). The timing of the changeover of precipitation from snowfall to rainfall is controlled by the temperature at which condensation occurs, which is primarily a function of latitude, elevation and time. Trends in snowfall in a warming climate can initially increase at high elevations given the greater moisture content, but once temperature increases at that altitude reach a threshold required to change the precipitation type, trends in snowfall will reverse, despite the ongoing increase in precipitation. For example, the higher latitudes experience increased snowfall until 2050 (Figs. 16c-d) while most other lower elevations and lower latitudes experience continuous reductions through the 21st century. In contrast, coastal B.C. and Alaska experience a reversal of the snowfall trend earlier, between 2025 and 2050 (Figs. 16b-c). After 2050, the highest elevations of the Eastern slopes of the Rockies are the only places in North America (excluding the Arctic) which receive neutral or increased annual mean snowfall (cf. Fig. 16d-e) and by 2100, virtually all other locations experience substantial reductions in simulated snowfall (Fig. 16e) as the winter season becomes shorter and more precipitation falls as rain. This is primarily a result of the high elevation, the continental climate, and decreases in the midlatitude jet strength (cf. Fig. 3d).

3c: Orographic lift and water vapour

A decrease in the strength of the midlatitude jet would have a negative impact on orographic precipitation rates if all other factors were held constant. Broccoli and Manabe (1992) found that maximum precipitation rates over North America were

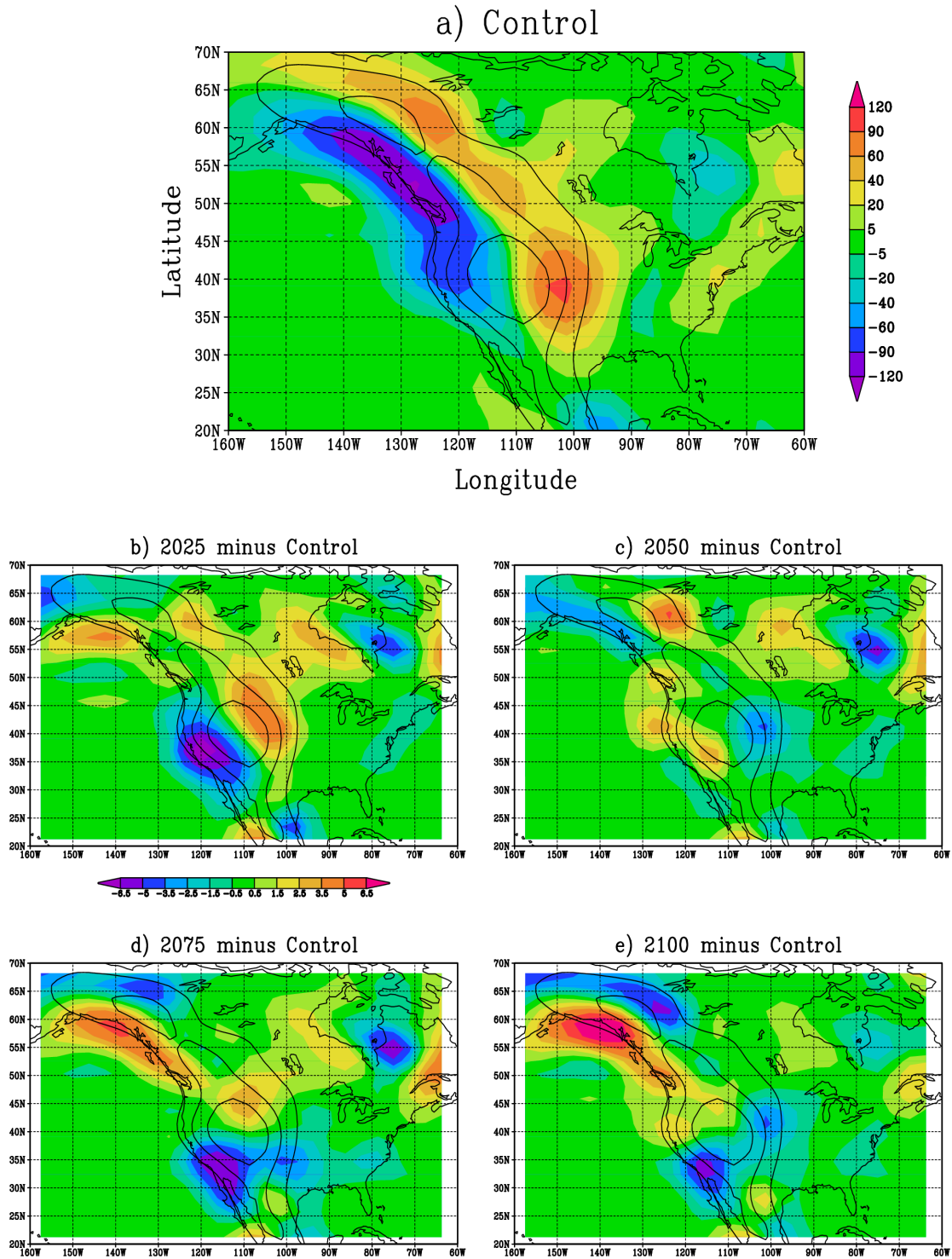


Figure 17: Mean ω (mPa s^{-1}) for a) the years 5 – 27 of the control run. b) The years 2014 – 2036 of the transient CO_2 run minus a. c) As in b but for the years 2038 – 2060. d) As in b but for the years 2064 – 2086. e) As in b but for the years 2087 – 2109. Results are averaged over lowest 5 σ levels: $\sigma = 0.99665 - 0.77695$ and overlaid on the 500, 1000 and 1500 m elevation contours for reference

displaced inland, away from the West coast, in a simulation of a flat planet atmosphere. From the momentum equation in sigma coordinates, the vertical motions induced by orographic forcing may be written as $\omega = \vec{u} \cdot \vec{\nabla} p_\sigma$ where p_σ is the pressure on a sigma surface, u is the vector wind, and ω is the orographically forced vertical motion in pressure coordinates ($\text{Pa} \cdot \text{s}^{-1}$). In general, precipitation patterns and anomalies in Western North America correlate spatially and temporally with negative ω and its anomalies (cf. Figs. 14, 15, and 17). Simulated results indicate that there is a gradual decrease of ω , with roughly 5% less air lifted over the Rockies by the end of the 21st century. This is essentially a 5% decrease in the vertical winds forced by topography. However, there are simulated increases in precipitation (cf. Figs. 2a-c, 3c, 14b-e, 15b-e), so this mechanical explanation cannot be the only factor important for predicting long term precipitation changes over topography.

The condensation rate of an adiabatically lifted air parcel of unit mass may be written as a function of the surface temperature T , the dewpoint temperature T_d , the vertical velocity in the air column w , and the height of ascent H . Although the condensation rate is not the precipitation rate, it is an important factor in the determination of the precipitation rate and is also responsible for the formation of clouds which block incoming solar radiation, both pertinent variables for glacial mass balance calculations. The differential condensation rate of mass m (measured in kg m^{-2}) at a point in a saturated column of air can be written as,

$$(3.1) \quad \frac{dm}{dt} = \frac{d\rho}{dT} \frac{dT}{dz} \frac{dz}{dt}$$

where ρ is the saturated vapour density (in $\text{kg} \cdot \text{m}^{-3}$ a function of air temperature only), Γ_m is the moist adiabatic lapse rate in $^\circ\text{C}/\text{m}$, and $w = dz/dt$ is the rate of ascent in m/s .

Taking the empirical equation of Bolton (1980), which gives the saturation vapour pressure e_s (in kPa) as a function of T in $^\circ\text{C}$,

$$(3.2) \quad e_s(T) = 0.6112 \exp\left(\frac{17.67T}{243.5 + T}\right)$$

and dividing by $R_{H_2O}T$ (where R_{H_2O} is the gas constant for water vapour), one arrives at the following relation for the saturation density of water vapour as a function of temperature.

$$(3.3) \quad \rho(T) = \frac{611.2}{R_{H_2O}(T + 273.15)} \exp\left(\frac{17.67T}{243.5 + T}\right)$$

Noting that temperature is a function of height, the volume moisture deposition rate in a saturated column may be written from (3.1) as

$$(3.4) \quad \frac{dM}{dt} = \int_{h_{LCL}}^{h_{top}} \frac{dm}{dt} dz = \Gamma_m w \int_{T_d}^{T_t} \Gamma_m^{-1} \frac{d\rho}{dT} dT$$

where M is the volume of water, T_t is the temperature at the top of the layer and T_b is the temperature at the lifting condensation level (both functions of T , T_d , and H). The resulting integral is evaluated easily if the moist adiabatic lapse rate is taken to be a constant (a reasonable assumption for shallow uplifting depths), giving the following expression for the condensation rate per unit area in a saturated air column undergoing lift between T_b and T_t .

$$(3.5) \quad \frac{dM}{dt} = \frac{w}{R_{H_2O}} 611.2 \left[\frac{1}{T_b + 273.15} \exp\frac{17.67T_b}{243.5 + T_b} - \frac{1}{T_t + 273.15} \exp\frac{17.67T_t}{243.5 + T_t} \right]$$

with

$$(3.6) \quad T_t = H \Gamma_m + \Gamma_m \frac{T - T_d}{\Gamma_m - \Gamma_{dp}} + T_b$$

and

$$(3.7) \quad T_b = \frac{T \Gamma_{dp} - T_d \Gamma_d}{\Gamma_{dp} - \Gamma_d}$$

as a first order approximation, where Γ_d is the dry adiabatic lapse rate, and Γ_{dp} is the

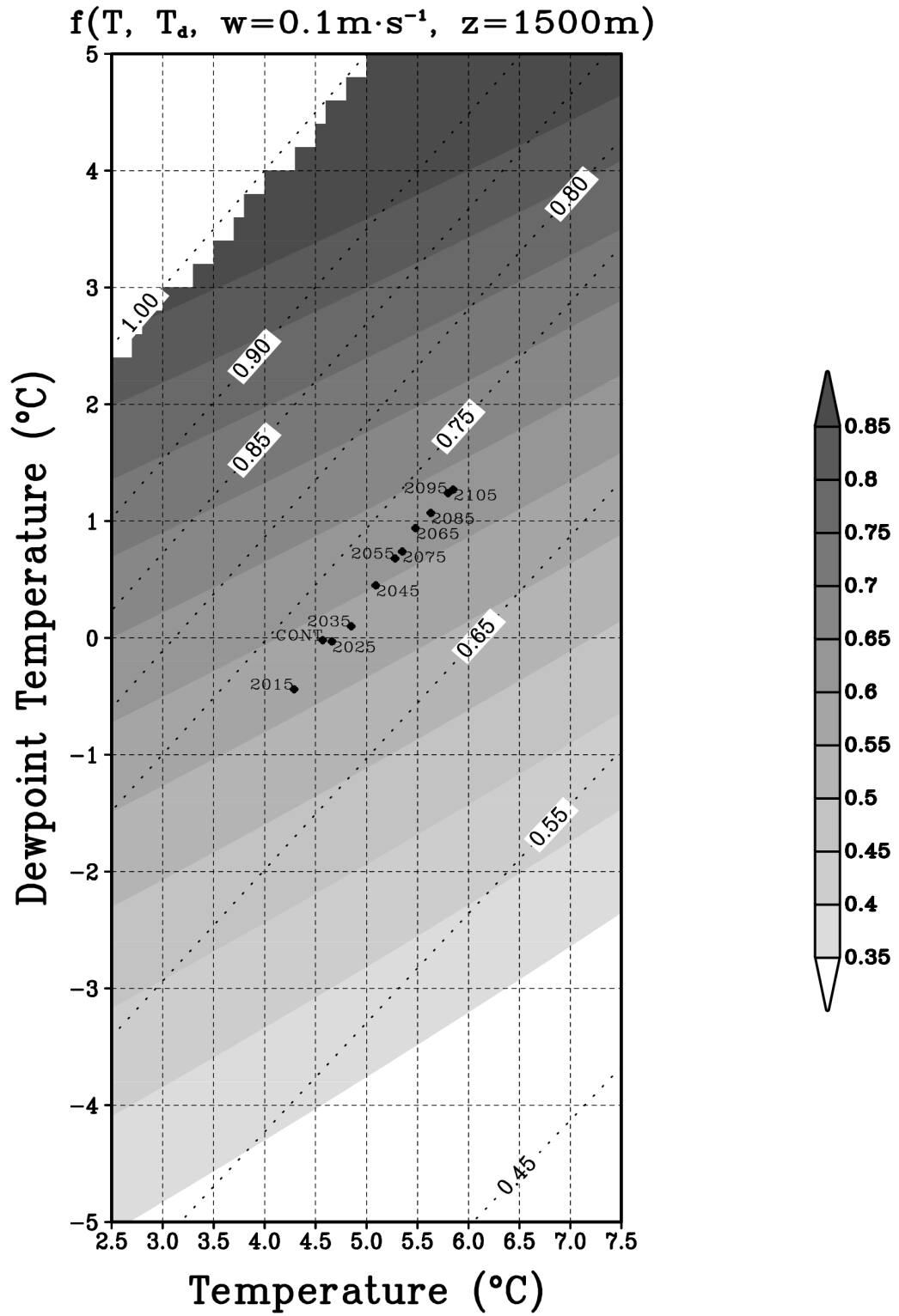


Figure 18: The condensation rate (mm/hr). Points plotted are model 10 year averages over lowest 5 σ levels, spanning $\sigma=0.99665 - 0.77695$, 170W to 130W, and 30N to 55N. Dotted lines are lines of constant relative humidity.

dewpoint temperature lapse rate.

Figure 18 shows a graph of this function with H and w set to 1500 m and 0.1 m/s respectively. These values are typical for parcels with a horizontal velocity of 16.7 m/s being uplifted by a 1500m/250 km aspect ratio slope, consistent with the model average terrain slope and horizontal velocities from coastal British Columbia in winter (cf. Fig. 15). Lines of constant relative humidity are also plotted for reference and cross from regions of low condensation rate to regions of high condensation rate as temperature increases.

The points plotted are 10 year means from a 3 dimensional box over the Northeast Pacific, which is the source region for much of the precipitation that falls over Western Canada. Global warming has been shown to increase temperature and dewpoint temperatures in such a way as to keep relative humidity changes relatively small (Ingram 2002), causing precipitation rates to increase (Lorenz and DeWeaver 2007). The relationship between temperature and dewpoint temperature over the Northeastern Pacific in a warmer climate is such that relative humidity remains roughly unchanged and the condensation rate of potentially uplifted air parcels increases by around 15% by the end of the 21st century (Fig. 18).

If potential condensation increases by 15%/century (cf. Fig. 18) and vertical motions forced by topography decrease by 5%/century (cf. Fig. 17), then it is reasonable to assume that precipitation rates due to orographic forcing will increase by about 9%/century (see eqn. (3.1), $1.15 \text{ times } 0.95 = 1.0925$) along the West Coast of North America. Based on the net 7%/century increase in mid and high latitude precipitation due to changes in convection and baroclinic activity (cf. Figs. 2d and 3c) and the 9%/century increase predicted by this simple orographic model (cf. Figs. 17, 18), one can infer that precipitation amounts could increase substantially over the Rocky mountains, by 16%/century. Although the effects of orographic forcing are evident in the modelled

precipitation fields over the Rockies, the simulated increase of around 10%/century is likely to be an underestimate because of the GCM's spatially smoothed topography.

4: Discussion

Studies of climate change performed using the GFDL and other general circulation models (Hansen et al. 1984, Manabe et al. 1991, Johns et al. 2003, Meehl et al. 2005, Flato and Boer 2006) have generally shown similar responses to increasing CO₂ concentrations. Namely, precipitation in the ITCZ and at mid and high latitudes (cf. Figs. 2a-c, 3c, 14, and 15) and surface temperatures (cf. Figs. 9, 10, and 11), with higher amplitude changes at high latitudes and over land (cf. Figs. 3a and 4a). The precipitation increases are attributable to increases in water vapour content (cf. Figs. 3b, 4c, and 4d) despite decreases in the baroclinic activity associated with the midlatitude jets (cf. Fig. 4b). Trends in relative humidity over the past 100 years have shown very little change (Dai 2006), lending credibility to model predictions in the vicinity of the Rocky mountains, which also show little change in relative humidity through the 21st century (cf. Figs. 3b, 4c-d, 18). Lorenz and DeWeaver (2007) argue that because relative humidities are predicted to stay close to constant in a warming climate (Ingram 2002), precipitation rates must increase despite a weakening of the large scale circulation, emphasizing a more prominent role of latent heat fluxes in global energy redistribution. Simulated warming patterns over North America are also similar to those produced in regional climate modelling studies of Canada. In particular, Plummer et al. (2006) found greater summertime warming over the Great Lakes region of Canada (cf. Figs. 9-11) and a higher amplitude Arctic warming during winter (Figs. 3a, 4a). Although the magnitudes of the temperature increases simulated by Plummer et al. (2006) and Flato and Boer (2006) is larger than the increases presented here, this is primarily due to the stronger CO₂ forcing used in those studies.

Snow and ice mass balance studies have shown that environments at high latitudes and high altitudes can become more favorable for the existence of semi-permanent snow and ice in a warmer climate, as warmer temperatures result in more precipitation which falls as snow (Hewitt 2005, Box et. al 2006, Fealy and Sweeney 2007). However, precipitation type is controlled by temperature, which rises under projected 21st century atmospheric CO₂ concentration. As a result, at higher elevations of North America annual mean snowfall initially increases but then drops off under the CO₂ forcing (cf. Figs. 1, 16–e). A regional modelling study of the Sierra Nevada by Kim et al. (2002) found similar variability in a doubled CO₂ climate, with snowfall increases at elevations above 2500 m. This illustrates the effects of elevation on temperature and thus precipitation type in a warmer climate.

Given the spectrally smoothed model topography (Navarra et al. 2000), model elevations at the locations of the glaciers are on the order of 100's of meters less than the elevations of actual equilibrium line altitudes (ELAs) in the Rocky mountains. Estimates of temperatures at the high elevation at which glaciers in the Rockies exist (~ 2000-3500 m, Ommanney (1984), Schiefer et al. (2007)) would need to be acquired through statistical downscaling techniques. Furthermore, the model underestimates orographic precipitation and, consequently, changes in orographic precipitation due to global warming. In addition, the seasonality of maximum precipitation amounts in the Rockies combined with smoothed model topography make determination of the rate at which annual mean snowfall transitions to rain as a function of elevation very difficult, and changes in the nature of precipitation (snow or rain) are critical for mountain glaciers. Despite these topographic issues, the model reproduces an adequately realistic seasonal cycle and mean climate state over the North American Cordillera, a prerequisite for any climate change study. As a next step, it is therefore desirable to use a model containing sufficiently high spatial resolution (Bromwich et. al 2005, Box et. al 2006) to represent

the complex topography of the Rocky mountains, driven by the results presented here, to gain a better grasp on global warming related changes as a function of altitude in this important region.

5: Conclusions

In comparison to other IPCC emission scenario simulations, the GFDL model has produced a reasonable representation of the climate system, with comparable seasonal cycles in temperature, precipitation, and wind patterns. Increasing CO₂ concentrations in a controlled experiment give an idea of how climate in the Rocky mountains may change during the next century. The thermal inertia of the ocean, combined with the seasonal weakening of midlatitude jets, results in a significantly higher amplitude continental warming, especially during the summer, and over Eastern North America. In addition, higher amplitude polar warming due to snow albedo feedbacks will result in a decrease in the strength of the midlatitude jet and its associated baroclinicity. The mean meridional circulation also decreases, as a consequence of significantly enhanced latent heat fluxes. With the decrease in the zonal wind strength at midlatitudes comes a decrease in mechanical orographic forcing over the Rocky mountains. However, model results indicate that the effects of these processes on precipitation are more than compensated for by increases in atmospheric water vapour and that precipitation generally increases. The GFDL model takes into account baroclinic and convective processes adequately, with the former explicitly resolved and the latter parameterized. However, because of the spectrally smoothed model topography, orographic processes are likely underestimated.

The observed large amounts of precipitation over the West coast are a consequence of the moisture laden Westerly winds orographically uplifted by the Rocky mountains in addition to baroclinic and convective activity. In the context of other types of precipitation, orographic precipitation is comparatively simple, depending only on the

slope of the topography, the strength of the wind, and the moisture content of the air (Andrieu et al. 1996, Esteban and Chen 2008). Analysis of modelled changes in potential orographic precipitation in coastal British Columbia in a warmer climate indicates that although there is a decrease in the strength of the midlatitude jet, the effect of this on orographic precipitation is merely to counter, to some degree, the effect of the increases in water vapour on precipitation. Modelled potential orographic precipitation over coastal British Columbia increases by about 9%/century (cf. Figs. 17 and 18). Because this is in addition to simulated increases in precipitation due to baroclinic and convective process, precipitation increases of 16%/century are likely for coastal British Columbia under the forcings presented here, representing a substantially larger increase than the global mean.

Chapter 2: Simulations of the potential effects of increasing atmospheric CO₂ concentrations on Alberta glaciers using a high resolution regional climate model.

1: Introduction

The mass balance of the world's glaciers has been shown to be well correlated with global mean temperature observations (Oerlemans 2005) suggesting that glaciers are important indicators of climate change. In response to the rising temperatures, most glaciers at mid and high latitudes have been receding rapidly in the last century (Oerlemans 2005), but there are also upward trends in precipitation and snowfall in some mountain ranges (Masiokas et al. 2006), leading to rare cases of glacial expansion (Molnia 2006, Fealy and Sweeney 2007, Hewitt 2005, Muskett et al. 2008). This counterintuitive behavior suggests that glacial recession is not necessarily a linear function of mean temperature.

There are hundreds of glaciers, ice fields, and semi-permanent areas of snow and ice in the mountains of Western Alberta and British Columbia (Ommanney 1984, Schiefer et al. 2007). These ice masses are a source of fresh water which contributes significantly to river flow and is particularly important during hot, dry summers (Sidjak and Wheate 1999; Stahl et al. 2008). Furthermore, they have undergone significant volume loss since 1985 (Schiefer et al. 2007). Global warming-related changes to these glaciers will therefore have an impact on agriculture, hydroelectric power generation, and municipal water supplies in Western Canada. The objective of chapter 2 will be to build on GCM results presented in chapter 1 and to provide a climate forecast with sufficiently high spatial resolution to quantify the potential changes to particular glaciers in Southwestern Alberta and Southeastern British Columbia. These glaciers were targeted because of the monitoring stations that have been established on them as a part of the Western Canadian Cryospheric Network (WC2N, <http://wc2n.unbc.ca/>).

The general circulation model (GCM) results presented in chapter 1 show a realistic response to increasing CO₂ concentrations, in general agreement with predictions of Johns et al. (2003) and Meehl et al. (2005) amongst others. Simulated precipitation

rates increase by up to 10% and July temperatures increase by up to 3°C in the Rocky mountains by the end of the 21st century. Furthermore, because Rocky mountain precipitation is largely orographic, results from chapter 1 imply that precipitation increases are likely to be significantly amplified in a warmer climate, due to increases in specific humidity. Although these results are essential for a regional climate change study, the GCM data on its own lacks the spatial resolution necessary to fully quantify regional climate changes. In particular, orographic precipitation rates are underestimated given the spectrally smoothed topography (Navarra et al. 2000). Nevertheless, the GCM does capture changes in global dynamics, such as the weakening and Northward-shifting midlatitude jet and the intensification of the hydrological cycle under increased atmospheric specific humidity, a necessary first step in quantifying local changes in glacial mass balance at high elevations.

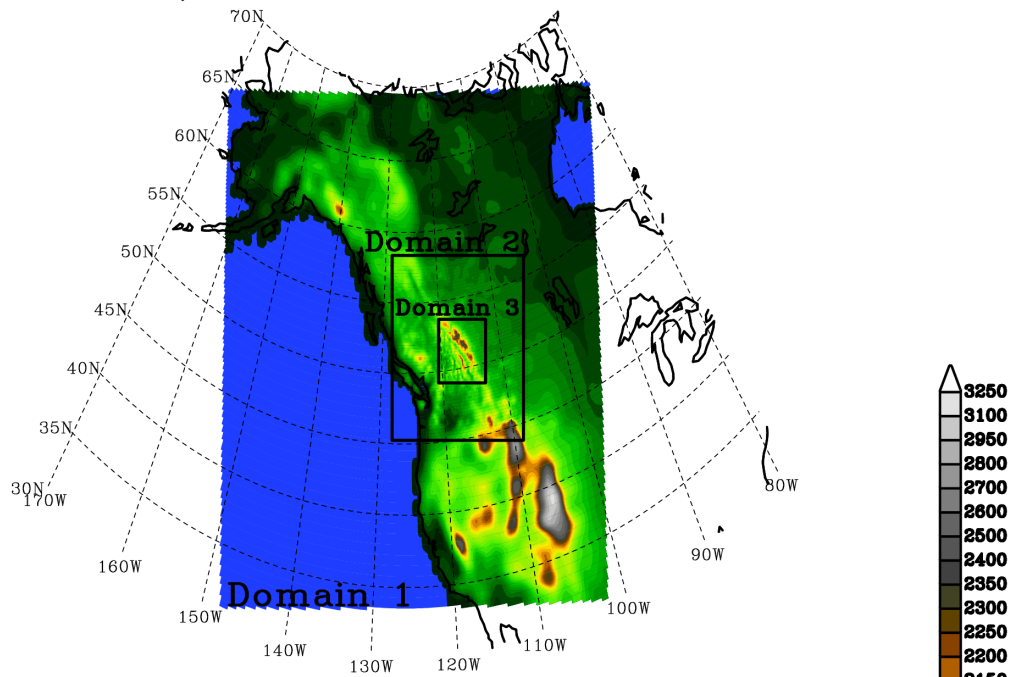
Numerous studies have been performed on the potential behavior of large icesheets such as those of Greenland and Antarctica under global warming scenarios (Huybrechts and de Wolfe 1999, Otto-Bliesner et al. 2006), but few studies of potential global warming-related changes to small glaciers have been performed, in part because of the inability of low resolution GCMs to quantify changes in regions where elevation varies significantly over small distances, i.e. mountainous regions. The goal of this study is to acquire climate data at sufficiently high spatial resolution to capture the small scale topographic features of the Rocky mountains and the effects of these on precipitation, temperature, and solar radiation, necessary for quantification of glacial mass balance in the region.

One way of obtaining a complete set of GCM variables required to examine the possible impact of climate change on glacial mass balance is to extrapolate from the results using a technique known as statistical downscaling (Widmann et al. 2003, Wood et al. 2004, Radic and Hock 2006). By applying sets of transfer functions to local GCM

data, one can extract higher resolution information from low resolution data. These transfer functions are acquired by quantifying relationships between observations and global reanalysis data (e.g. Wilby et al. 1998). Although this technique is straightforward and computationally inexpensive, it relies on knowledge of global teleconnections and temporal oscillations (Wilby 1997) that can potentially change in time. This was shown to be the case in a warmer climate in chapter 1, with teleconnections associated with equatorial Pacific sea surface temperatures weakening at high latitudes (cf. Fig. 1.6). Finding an adequate statistical downscaling model is further complicated by the rough/steep topography of the Rocky mountains. An alternate approach to acquiring high spatial resolution climate data from an GCM, and the one that is pursued in this chapter, is to feed global model results into a significantly higher resolution mesoscale model (MM).

The non-hydrostatic Pennsylvania State University / National Corporation for Atmospheric Research Mesoscale Model 5 (PSU/NCAR MM5) is chosen as an adequate MM based on the availability of complicated moisture and land surface parameterizations, as well as accurate results produced in studies of mountainous and seasonally snow covered Iceland by Bromwich et al. (2005). Results at 6 km horizontal resolution are obtained for significant portions of the Rocky and Columbia mountains. This spatial resolution is sufficient to resolve the large valleys such as those of the Columbia, Kootenay, Bow, North Saskatchewan, and Athabasca rivers in addition to major ranges of the Columbia and Rocky mountains. This area contains the Haig, the Ram River, and the Peyto glaciers, specified to be of particular interest by the WC2N. The Ram River glacier is a small cirque glacier well East of the continental divide, the Haig glacier is small and located on a plateau on the continental divide, and the Peyto glacier is a considerably larger valley glacier whose source region is the Wapta ice fields, an area on the continental divide. Peyto glacier, in particular, has experienced substantial

a) MM5 domains



b) Domain 3

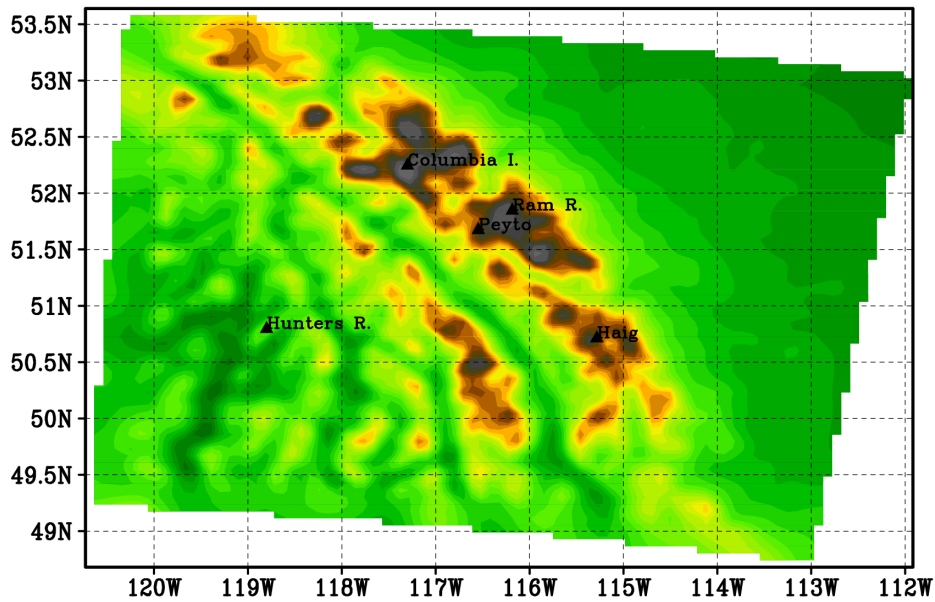


Figure 1: a) The 3 regional model domains and topography. b) Topography in domain 3 and the locations of the Haig, Ram River, and Peyto glaciers. Coloured contours show elevation in meters.

recession in the last century (Watson and Luckman 2004). In addition to these glaciers, the Columbia Icefields and a relatively high elevation region of the Western Columbias will also be considered. The 5 locations of interest are marked on a topographic profile of the highest resolution nested domain (Fig. 1b).

The remainder of chapter 2 is presented as follows. Section 2 is a detailed explanation of the MM5 parameterizations used as well as the model configuration. Section 3 presents results from an ensemble of Januaries and Julies over Western Canada but with a focus on the Rocky mountains. Section 4 presents high spatial resolution annual mean results from the nested domains. Finally, section 5 discusses implications for glacial mass balance and section 6 provides a discussion and conclusion.

2a: Mesoscale model setup

The MM has 24 sigma levels with higher vertical resolution near the surface. Three domains of roughly 54, 18, and 6 kilometer horizontal resolution (82x76, 88x79, and 94x82 grid points respectively) are set up to run over the Rocky mountains (Fig. 1a). The domain timesteps are 162, 54, and 18 seconds respectively. The solar constant used is $1324.69 \text{ W} \cdot \text{m}^{-2}$.

2b: Mesoscale model parameterizations

To account for the wide range of precipitation types encountered in all seasons in the Rocky mountains, the model implements the Reisner et al. (1998) mixed phase method, which includes five states: vapour, ice, snow, rain, and cloud, each quantity being dependent on each other and on other model variables such as vertical velocity and temperature. In order to better parameterize surface moisture fluxes in both winter and summer, the NOAH land surface model is used (see Chen and Dhudia 2001, NOAH is short for National Center for Environment Prediction (NCEP), Oregon State University

(OSU), Air Force (AF), Hydrology Research Lab (HRL, National weather service)), with surface soil moisture, temperature, and water quantities extrapolated to lower levels based on modern mean difference profiles through soil layers. Sea surface temperatures are updated during model integration from the Modular Ocean Model version 2 (e.g., Pacanowski 1995) daily mean data. The Grell (1993) cumulus parameterization is implemented and includes shallow convection. The planetary boundary layer physics implements a non-local approach (see Troen and Mahrt (1986)) and vertical mixing in clouds conserves equivalent potential temperature. The radiation scheme includes the effects of clouds on long and short wave radiation and is based on that of Stephens (1984) and Garand (1979) and it is computed every ten time steps.

2c: Choice of GCM data used as input

The GCM used as input for the MM is the Princeton GFDL model (Gordon and Stern 1982). Two global atmosphere-ocean model integrations were performed. The first, starting from 2007 and ending in the year 2110 has model atmosphere CO₂ concentrations prescribed by the IS92a-Fr-Central emission scenario, closest to the upper B2 family of modern IPCC projections, which predicts the atmospheric carbon dioxide concentration to be almost 690 ppmv by the year 2110 in a quadratically increasing fashion (cf. Fig. 1.1) (IPCC 2007). The second integration is a 28 year control run, with carbon dioxide concentrations set to 387 ppmv. These data sets are subdivided into 10 year subsets. 10 years is chosen as an adequately long time interval to capture interannual variability in the boundary condition forcing of the MM. The subsets used were the years 15-24 of the control run and the years 2020-2029, 2045-2054, 2071-2080, and 2096-2105 from the transient CO₂ run, henceforth referred to as the Control, 2025, 2050, 2075, and 2100 runs, respectively. The MM is run in one month intervals, with a two day spin up period from the 10-year subsets of GCM daily data in two ways.

First, it is run using all 10 Januaries and all 10 Julies from the 10 year subsets, adding up to 100 runs in total. The months of January and July are chosen because these are the coldest and hottest months of the year in the Rocky mountains. Global warming-related changes to the climate of the most extreme months are therefore indicative of changes in the maximum amplitude of the seasonal cycle in precipitation and temperature. In particular, the heaviest precipitation and coldest temperatures along the west coast are observed during winter and the reverse is true during summer. Although this method produces information on changes in the amplitude of the seasonal cycle, it gives little information on changes during the fall and spring, months crucial for determination of changes in annual precipitation amounts and type.

Second, to acquire high resolution climate data spanning the entire seasonal cycle, the months whose surface temperature and precipitation over the Rocky mountains (120°W - 110°W and 47°N - 55°N) are closest to the 10-year mean (over the same region) from the 10-year subsets were also used as input for the MM. This method is preferable to using the 10-year monthly means since daily variability in the boundary condition forcing enables synoptic systems to contribute to the regional climate results. In this way, the mean annual cycle for the control simulation, 2025, 2050, 2075, and 2100 can be acquired at the high spatial resolution of the MM. These additional simulations require 50 more MM integrations. The total of 150 MM simulations represents 10% of the total number of months output by the GCM runs. MM simulations for a higher percentage of the GCM runs are, at this time, computationally infeasible.

These simulations therefore provide snapshots of January, July, and annual mean climate over the Rockies for 5 time periods in the 21st century, Control (present day CO_2), 2025, 2050, 2075, and 2100.

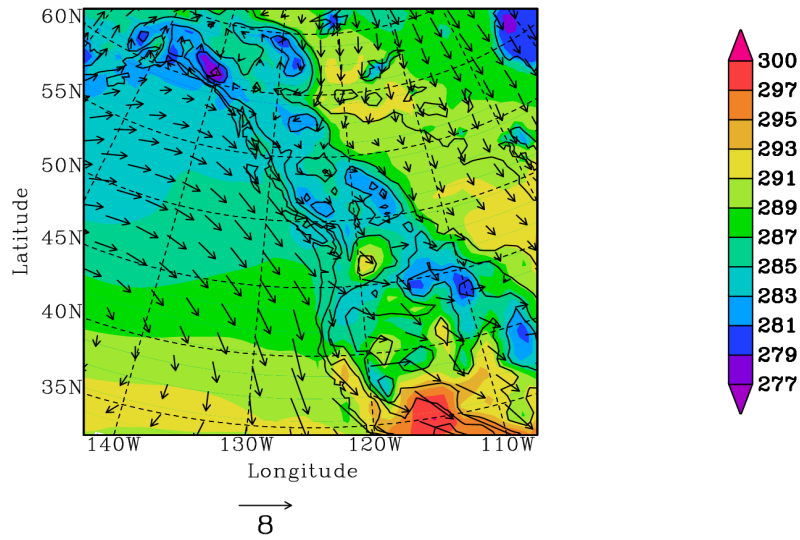
3: Results and Analysis

The model integrations were performed using 64 processors on a Western Canada Research Grid (Westgrid) SGI Origin model 3900 with 256 MIPS 700 megahertz IP35 processors and 256 gigabytes of main memory. The 150 month long integrations required approximately 16 hours of computer time per integration. Two and three dimensional model output for all 3 domains required ~26.5 megabytes per day of output. Daily output over the total of 150 months requires about 121 gigabytes of storage space. In addition, the 50 years of daily mean global ocean and atmosphere data used as input for the MM required about 400 gigabytes of storage space.

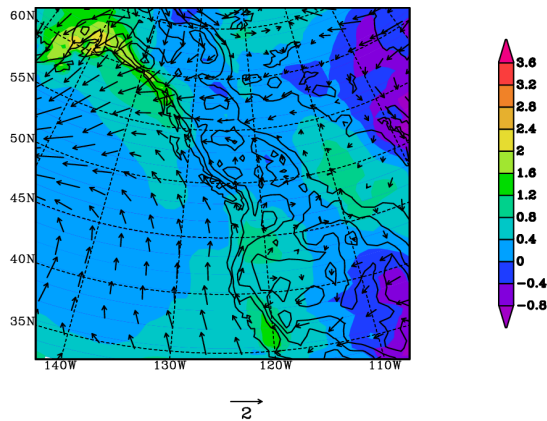
3a: January/July Results

The MM reproduces the higher amplitude continental warming simulated by the GCM for July (cf. Figs. 1.9b-e, 2b-e) although there is a significant degree of regional variability not observed in the GCM results. The differences between GCM and MM warming patterns are primarily related to differences in spatial resolution, but are also related to differences in the complexity of model land surface treatments. The U.S. desert Southwest and the plains of the interior of North America experience the largest increases in temperature, with smaller changes in the North Pacific and at higher elevation regions (Fig. 2b-e), primarily along the Cordillera South of 60°N, with the most obvious moderating effects in the mountains of Colorado and the coast mountains of British Columbia. Temperatures in the Rocky mountains increase by over 2°C by 2100 (Figs. 2b – 2e), about 1°C less than increases in surrounding regions and in the GCM predicted increases for the same region (cf. Fig. 1.11). Although surface temperatures are an important indicator of long term snow melt at midlatitudes (primarily because they are well correlated with insolation on daily and seasonal timescales), an indirect, statistically-based method such as the positive degree day melt index (Hock

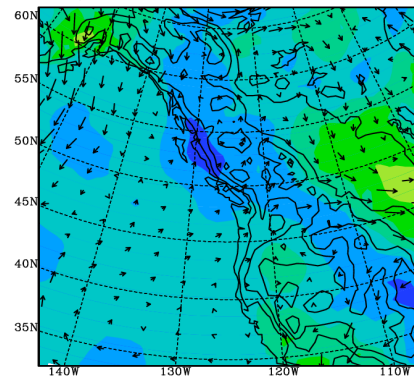
a) Control



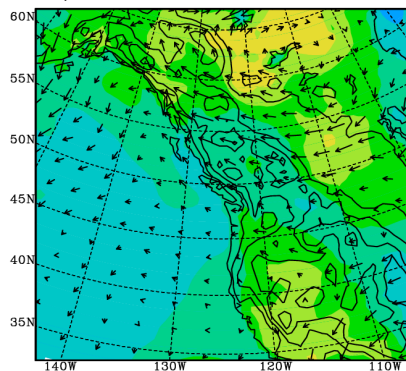
b) 2025 minus Control



c) 2050 minus Control



d) 2075 minus Control



e) 2100 minus Control

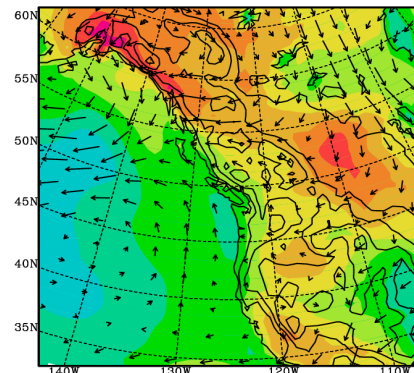
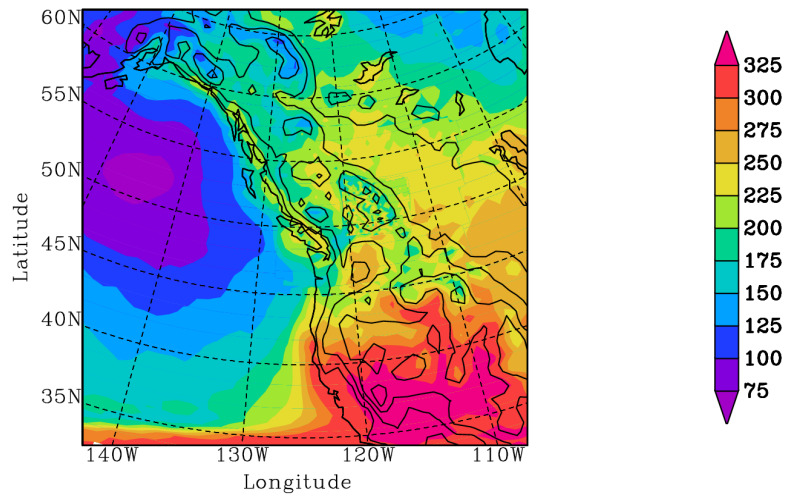
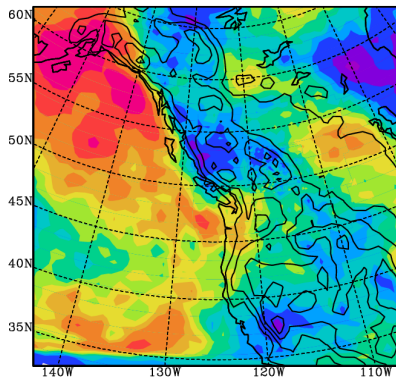


Figure 2: The domain 1 temperature (K) and lower level winds (m/s) for a) the 10-year July control simulation. b) The 10-year July 2025 mean minus a. c) As in b but for 2050. d) As in b but for 2075. e) As in b but for 2100. The winds (m/s) are averaged over the lowest 8 σ levels: $\sigma = 0.995 - 0.775$. Results are overlaid on 500, 1000, 1500, 2000 and 2500 m elevation contours for reference.

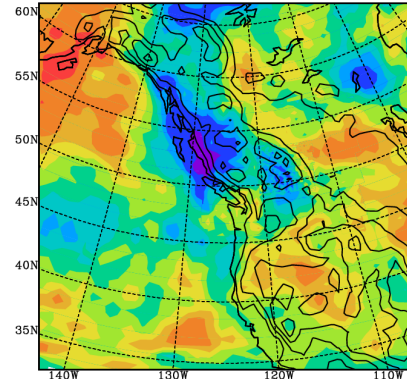
a) Control



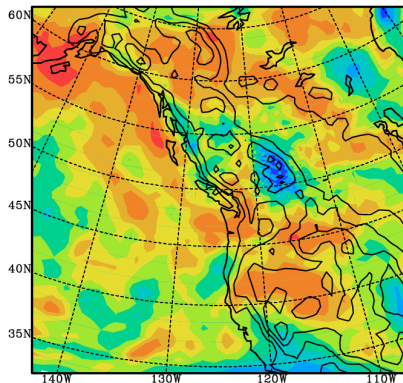
b) 2025 minus Control



c) 2050 minus Control



d) 2075 minus Control



e) 2100 minus Control

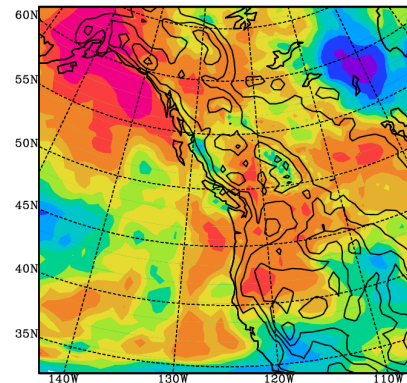


Figure 3: The domain 1 surface radiation (W/m²) for a) the 10-year July control simulation. b) The 10-year July 2025 mean minus a. c) As in b but for 2050. d) As in b but for 2075. e) As in b but for 2100. Results are overlaid on 500, 1000, 1500, 2000 and 2500 m elevation contours for reference.

2003) cannot take into account the full complexity of the dependence of snow and ice at high elevations in the Rockies on global mean temperatures. Although the sensible heat flux into a snow or ice surface is proportional to the air temperature, the largest source of energy for snow and ice melt in the Rocky mountains is the incident short wave radiation (Munro 1990) despite the fact that snow albedo ranges between 60 and 90% (Warren 1982). Therefore, potential changes in short wave radiation in a warmer climate cannot be ignored.

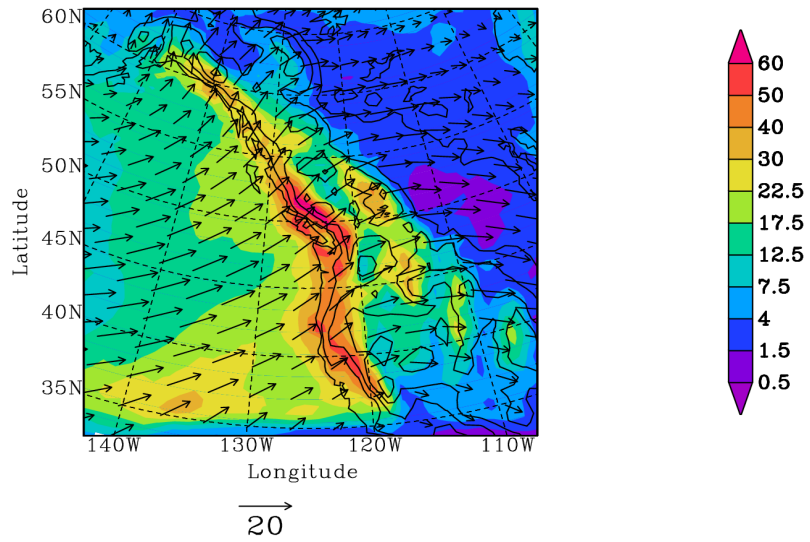
July surface insolation decreases strongly with latitude and with altitude in many locations, primarily as a result of cloud formation by orographic forcing (Fig. 3a). It is apparent that annual mean surface radiation is affected only by cloud cover and latitude. Minimum and maximum net surface solar radiation (incoming minus outgoing) in the Northeast Pacific and in the Southwestern U.S., respectively. There is a local maximum in incoming surface radiation over the steep terrain of the coast mountains. This is of frequent downsloping surface winds that inhibit the formation of low clouds in this region during the summer (cf. Fig. 2a). Results in time show substantial increases in incoming July short wave radiation in most places (Figs. 3b-e) that are correlated with temperature increases (Fig. 2b-e). The exceptions are the higher elevation locations. In the Rocky mountains, in particular, short wave radiation is reduced below the control values, most substantially in 2075, and least in 2100 (Figs. 3b-e). These changes are consistent with the elevation dependence of temperature increases (Fig. 2b-e), with limited temperature increases at higher elevation. Negative trends in short wave radiation are a consequence of increased orographically forced condensation in the moister climate. The reduction in incoming solar radiation at higher elevations is a negative feedback mechanism for snow and ice melt in a warming climate.

The MM produces more regional variability in the precipitation fields than simulated in the GCM results. Specifically, the improved representation of orographic

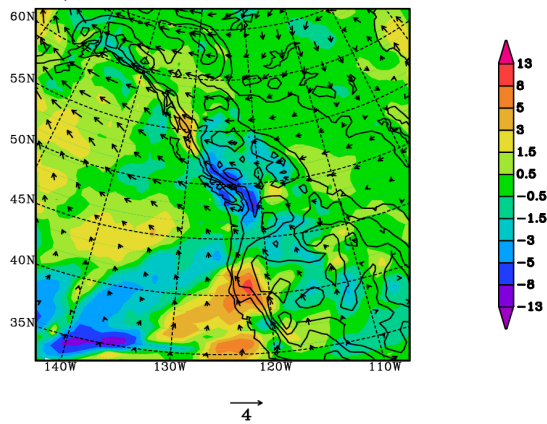
forcing in the higher resolution topography causes the greatest precipitation amounts to be concentrated in steep coastal regions and at high elevations during January (Fig. 4a). Cyclonic activity off the Pacific coast increases and moves Southeastwards until 2075, resulting in increases of precipitation along the West coast South of 50°N (Fig. 4b-d). However, as CO₂ concentrations approach double the modern value by 2100, the trend in increasing precipitation over the Rockies decreases, such that precipitation and wind changes between 2075 and 2100 resemble those from the doubled CO₂ experiments of Giorgi et al. (1994) and Leung and Ghan (1999b). In particular, there is a Northward shift of the strongest upsloping surface winds between 2075 and 2100, resulting in less precipitation in Washington and Oregon states and more along the British Columbia coast through South coastal Alaska. A gradual shift such as this can be explained by the higher amplitude polar warming, with midlatitude baroclinicity shifting poleward in the later years of the transient CO₂ simulation (Rinke and Dethloff 2008). However the higher amplitude polar warming occurs gradually through the 21st century and the trends in increasing Pacific cyclonic activity (Figs. 4b-e) decrease only after 2075 (Figs. 4c-e), suggesting that the changes simulated here can occur rapidly in time despite the gradual overall trend.

Although there is a Northward shift of the midlatitude precipitation band some time between 2075 and 2100 (cf. Figs. 4d and 4e) the mountains of Southern Alberta and British Columbia remain within the area significantly affected by baroclinic activity through 2100. Consequently, progressively more precipitation falls in the Rocky mountains in January as the century progresses, with increases of between 5 and 10% in 2050 and 2075 (Fig. 4b and 4c) and between 10 and 15% in 2100 (Fig. 4e), just short of the 16%/century increase suggested by the analysis of orographic precipitation performed in chapter 1 (Fig. 1.14). As expected, these increases are generally greater than the increases predicted by the GCM over the same region, a consequence of the improved

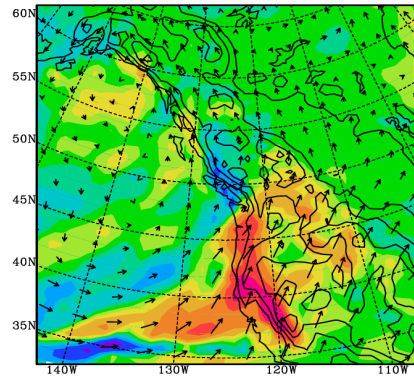
a) Control



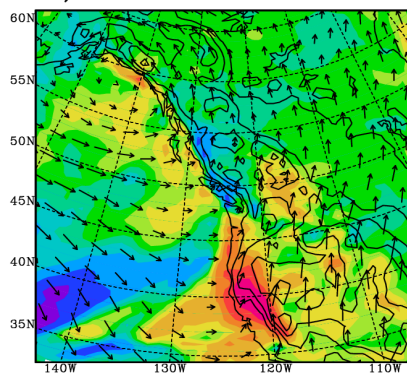
b) 2025 minus Control



c) 2050 minus Control



d) 2075 minus Control



e) 2100 minus Control

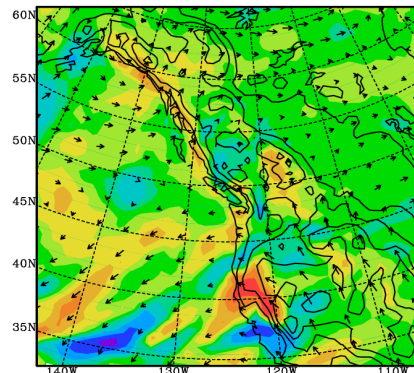


Figure 4: The domain 1 precipitation (cm) and lower level winds (m/s) for a) the 10-year January control simulation. b) The 10-year 2025 mean minus a. c) As in b but for 2050. d) As in b but for 2075. e) As in b but for 2100. The winds (m/s) are averaged over the lowest 8 σ levels: $\sigma = 0.995 - 0.775$. Results are overlaid on 500, 1000, 1500, 2000 and 2500 m elevation contours for reference.

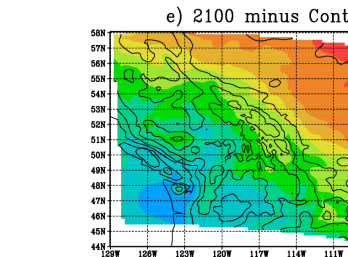
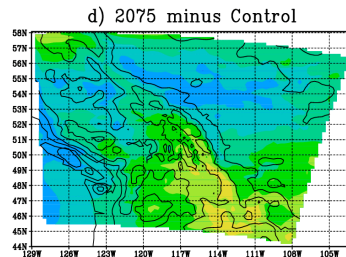
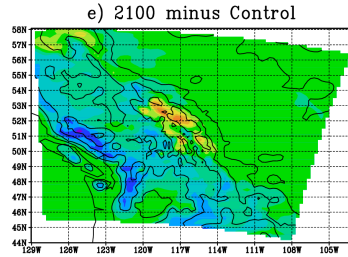
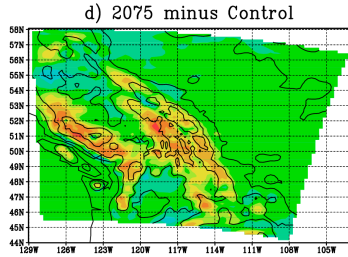
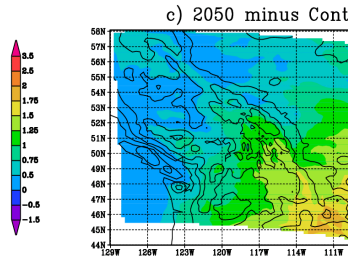
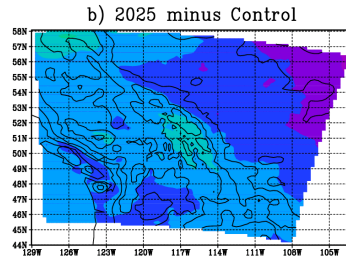
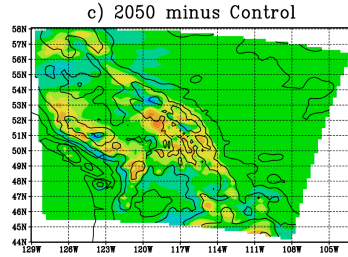
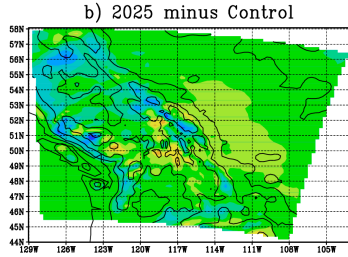
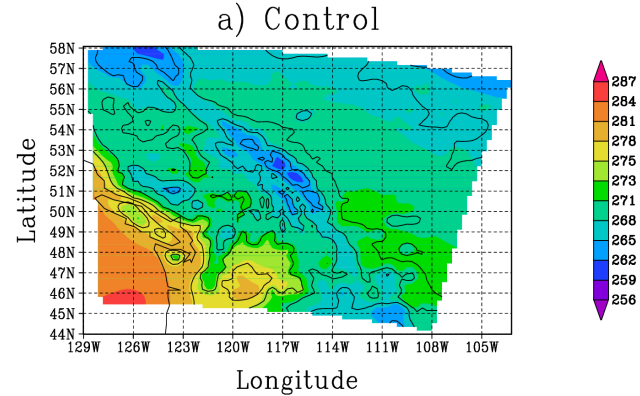
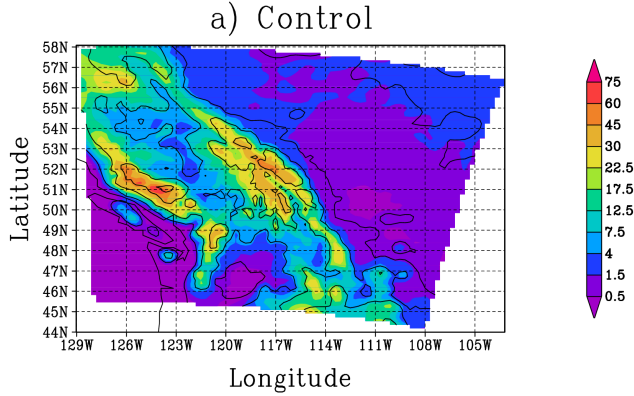


Figure 5: a) The control simulation 10-year January mean snowfall (cm water equivalent). b) The 10-year 2025 mean minus a. c) As in b but for 2050. d) As in b but for 2075. e) As in b but for 2100. Results are overlaid on 250, 500, 750, 1000, 1250, 1500 1750, 2000, 2250 and 2500 m elevation contours for reference.

Figure 6: a) The control simulation 10-year January mean temperature (K). b) The 10-year 2025 mean minus a. c) As in b but for 2050. d) As in b but for 2075. e) As in b but for 2100. Results are overlaid on 250, 500, 750, 1000, 1250, 1500 1750, 2000, 2250 and 2500 m elevation contours for reference.

representation of orographic precipitation. Precipitation increases do not necessarily guarantee increases in snow accumulation at high elevation because temperature increases will affect the fraction of precipitation that falls as snow.

In response to the effects of rising temperatures on precipitation and precipitation type (Fig. 5b-e), snowfall increases at high elevation with simultaneous decreases at lower elevations locations until 2075 (Figs. 5b-d). This occurs despite increases in surface temperature at high elevation (Fig. 6b-e). By 2100, however, the Rocky mountains experience much warmer temperatures and more precipitation falls as rain, resulting in a reduction of snowfall except at elevations above ~2250 m, where increased snowfall is evident (Fig. 5e).

Unlike in July, when temperature increases are more moderate at high elevation (Fig. 2b-e), in January there is substantially more warming at high elevation, particularly in the Rocky mountains but also in the Coast Mountains (Fig. 6b-e). This is evident throughout the 21st century, with lines of constant temperature change virtually parallel to lines of constant elevation (Fig. 6b-e). January surface temperatures increase by about 1.5°C in the Rocky mountains by 2100 (Fig. 6e), consistent with January results from chapter 1 (Fig. 1.8e). Temperature increases at high elevation are 0.25-0.5 degrees greater than those of surrounding lower elevations. The greatest temperature increase as well as the largest decrease in snowfall over the Rockies are observed in 2100 (cf. Figs. 5e and 6e), demonstrating the effect of temperature on precipitation type. Other mesoscale modeling studies have found a similar higher amplitude warming over higher elevations (Giorgi et al. 1994, Giorgi et al. 1997, Leung and Ghan 1999b, Kim et al. 2002) and the causes are largely attributed to snow and ice albedo feedback mechanisms. The simulations presented here, however, suggest an additional cause for higher amplitude warming at high elevation.

January surface temperature increases in the Rocky mountains are consistently

greater than those of surrounding low-elevations (Fig. 6b-e) and snowfall amounts increase through 2075 but then fall off by 2100, except at the highest model elevations (Fig. 5b-e), contrary to the notion that elevation-dependent temperature increases are caused by snow albedo feedback mechanisms alone. Furthermore, results from Marshall (2003) suggest that the snow-albedo effect on temperatures does not play as significant a role in determining surface temperature during January as it would during other times of the year when the solar inclination angle is higher at midlatitudes. These factors serve to reduce snow albedo feedback effects in the modeled January climate, and yet altitude dependent warming mechanisms are still clearly present (Figs. 6b-e).

Another mechanism which results in an altitude dependent warming is additional latent heating of the more moisture laden airflow uplifted by the Rocky mountains in the warmer climate. Evidence that higher amplitude warming at high elevations can be partially attributed to increased latent heating of airflow traversing the mountains comes from use of the following description of potential latent heating by orographic precipitation. With the aid of an empirical equation for the saturation vapour pressure (kPa) as a function of temperature ($^{\circ}\text{C}$) (Bolton 1980),

$$(3.1) \quad e_s(T) = 0.6112 \exp\left(\frac{17.67T}{243.5 + T}\right)$$

one can write the latent heating of an air parcel due to condensation of water vapour as a function of its surface temperature T and dewpoint temperature T_d , its lifting height H (in meters), and the consequent change in vapour density $\Delta\rho_v$. For a parcel of air, the rise in temperature due to latent heat release can be related to the amount of water that has changed phase as:

$$(3.2) \quad \Delta T = \frac{L_f \Delta\rho_v}{\rho_a c_p} .$$

with L being the latent heat of evaporation of water, c_p the heat capacity of air, ρ_a is the

density of air at H (taken to be 1.1 kg m^{-3} at 1500 m, consistent with a surface temperature of roughly 5°C and a pressure of 101.3 kPa). The temperature increase of uplifted parcels is then

$$(3.3) \quad \Delta T = \frac{611.2 L_f}{\rho_a c_p R_{H_2O}} \left[\frac{1}{T_b + 273.15} \exp \frac{17.67 T_b}{243.5 + T_b} - \frac{1}{T_t + 273.15} \exp \frac{17.67 T_t}{243.5 + T_t} \right]$$

with

$$(3.4) \quad T_t = H \Gamma_m + \Gamma_m \frac{T - T_d}{\Gamma_m - \Gamma_{dp}} + T_b$$

and

$$(3.5) \quad T_b = \frac{T \Gamma_{dp} - T_d \Gamma_d}{\Gamma_{dp} - \Gamma_d}$$

as a first order approximation, where Γ_w is the moist adiabatic lapse rate, Γ_d the dry adiabatic lapse rate, Γ_{dp} is the dew point temperature lapse rate, R_{H_2O} is the specific gas constant of water vapour, and T_t and T_b are the temperatures at the uplift height and at the lifting condensation level respectively. This function gives the temperature change due to latent heating of an uplifted parcel with specified surface temperature and water vapour concentration. A more accurate approximation of the change in temperature of an uplifted parcel can be acquired through iteration (Bolton 1980), however this approach is deemed sufficiently accurate for this purpose.

Figure 7 is a graph of this function with H set to 1500 m, a reasonable value for orographically forced ascent along the west coast, consistent with average surface flow and elevation characteristics in Figure 4. Lines of constant relative humidity are plotted for reference. The lines of constant temperature change (shaded contours) represent the relationship that surface temperature and dewpoint temperature must have to maintain the same latent heating, if uplifted. The points plotted are derived from the GCM data 10 year means from a 3-dimensional box over the Northeast Pacific confined to the lowest

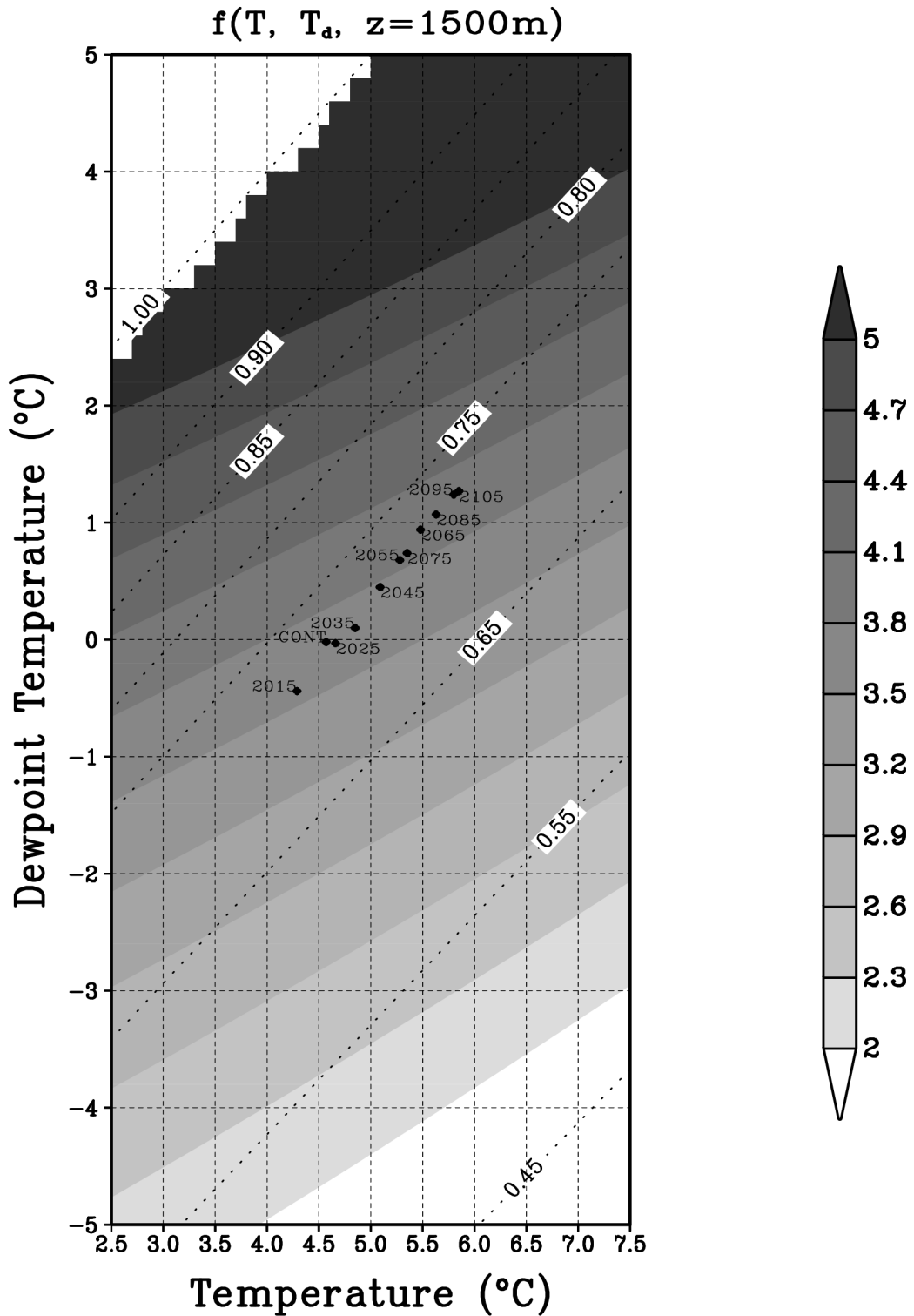


Figure 7: The potential latent heating due to uplift ($^{\circ}\text{C}$) of North Pacific Surface parcels. The points plotted are the AOGCM 10 year averages over lowest 5σ levels: $\sigma = 0.99665 - 0.77695$, spanning the region bounded by 170°W to 130°W and 30°N to 55°N . The dotted lines denote constant relative humidity.

quarter of the atmosphere (the area spanning 170W to 130W and 30N to 55N), the source region for much of the low-level air flowing over the Rocky mountains. A line through these points is roughly parallel to lines of constant humidity (as suggested to be a realistic consequence of global warming by Ingram (2002) and Lorenz and DeWeaver (2007)) and crosses from regions of lower latent heating into regions of higher latent heating with time. GCM results present a situation in which greater latent heating of uplifted lower-level North Pacific air occurs in a warming climate scenario. In fact, because of probable increases in atmospheric water vapour the latent heating of uplifted North Pacific surface air increases by about 0.5 degrees per 1500 meters per hundred years, roughly 15% more than the surrounding sea level increases. These results suggest that global warming will not only warm the higher terrain directly through ice and snow albedo feedback, but will also warm the lower to middle troposphere indirectly through enhanced latent heat release in the more humid air.

It has been shown that global warming should result in global increases in high cloud and a decrease in low and middle level cloud as a consequence of an upwards shift in cloud height (Hansen et al. 1984). This is a positive feedback for further warming because low and middle level clouds reflect short wave radiation efficiently and high cloud is a net absorber of long wave radiation (Hansen et al. 1984). However Hansen et al. (1984) do not discuss the seasonality of cloud cover changes or the effects of orographic forcing in great detail. The effects of changes in orographically forced condensation of water has been shown to have potentially significant effects on temperature and cloud cover at high altitude (Figs. 1.17, 7). As has been previously discussed, lower atmosphere water vapour content increases substantially in a warmer climate during both January and July (Figs. 8a and 8b) and at all lower levels of the troposphere. The increases are most pronounced during July (Fig. 8b) over the continental interior, as a direct consequence of the greater increases in simulated air

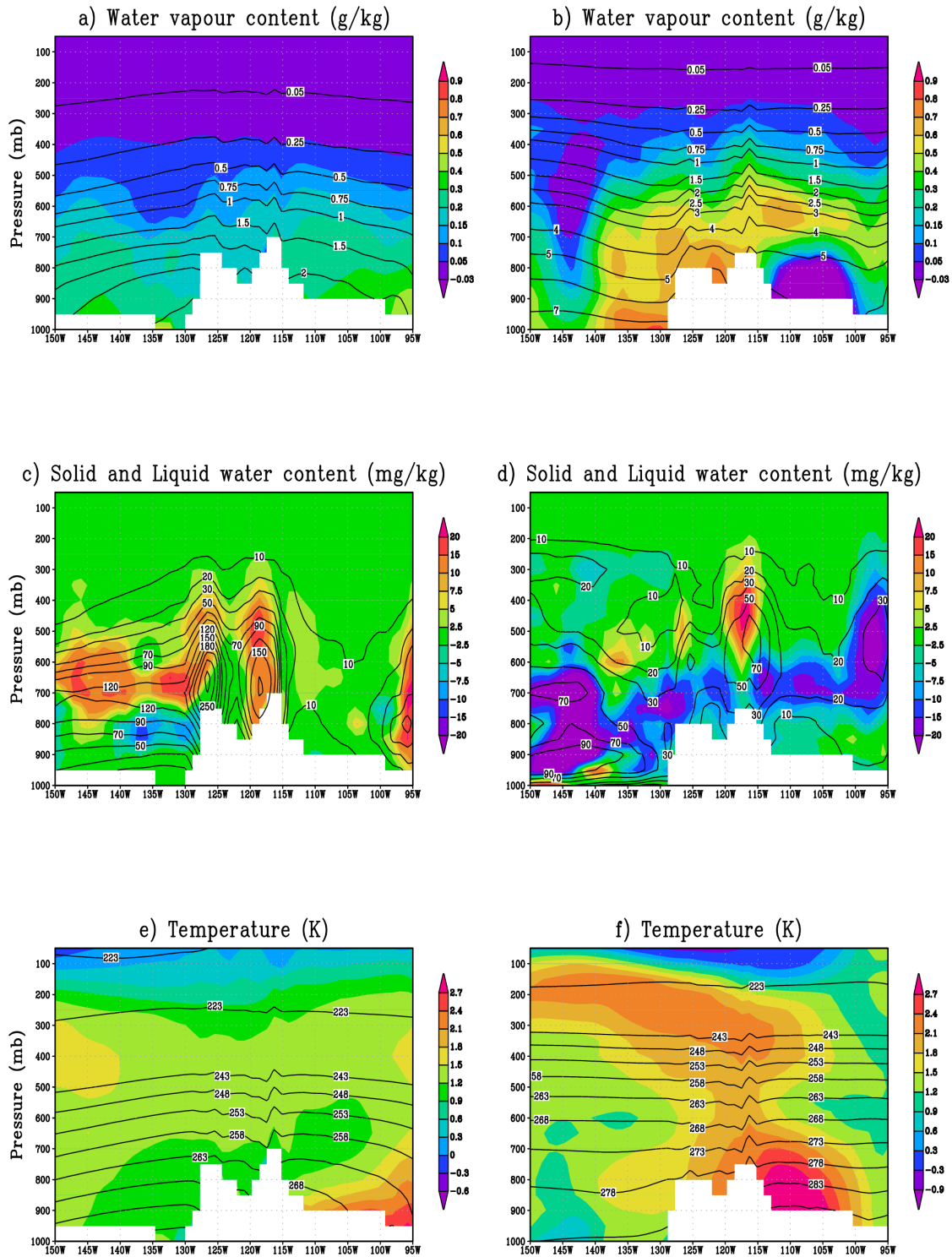


Figure 8: All plots show the 2100 mean minus the control mean in colour, giving 100-year rate of change of a) the January specific humidity. b) As in a but for July. c) The January solid plus liquid water concentration. d) As in c but for July. e) The January temperature. f) As in e but for July. The black lines show the control mean.

temperature there (Figs. 2b-e).

During January, increases in solid plus liquid water are simulated above 850 mb over mountainous topography (Fig. 8c). In contrast, over the Pacific solid plus liquid water increases only above 750 mb and decreases below that level (Fig. 8c), illustrating an upwards shift in the cloud base over the ocean during January. The most substantial increases in atmospheric solid plus liquid water content are simulated over the Western slopes of the Coast Mountains and the Rockies (Fig. 8c), where clouds are already very prevalent, indicating that cloud water density in January increases in a warmer climate over Southern British Columbia. The situation is much different during July, when the upwards shift in cloud water is prevalent not only over the Pacific but also over the Cordillera. Increases in cloud water are simulated only above 650mb over the Coast Mountains and the Rockies, with substantial decreases below that level (Fig. 8d). Increased middle level cloud during July are only simulated over the higher elevations (Fig. 8d), consistent with the changes in net radiation (cf. 3e). This also illustrates that orographic forcing in a warmer climate cannot be ignored in the determination of future radiative balance. Both January and July changes in cloud water show increases in cloud base height (figures 8c and 8d), as was suggested to be a likely consequence of increasing global temperatures by Hansen et al. (1984). Furthermore, these increases are more pronounced during the summer than during the winter (Fig. 8c and 8d), consistent with results of Dai et al. (2001).

Temperatures increase substantially in the lower levels of the troposphere, with higher amplitude changes over the continental interior during July (Fig. 8f), primarily because of the seasonal weakening of the midlatitude jet stream. Tropospheric temperature increases (Figs. 8e and 8f) allow for an increase in water vapour (Figs. 8a and 8b), which ultimately has the effect of increasing and redistributing cloud water (Figs. 8c and 8d) and latent heat release in the lower troposphere. This is particularly

apparent during January over the Rocky mountains, where temperature increases are proportional to height, caused by orographic forcing in the moister atmosphere (Fig. 8e). This phenomenon is also present during July (Fig. 8f), although substantially weaker because of weaker orographic forcing and the effects of increasing cloud cover (Fig. 8d) on radiative heating. Figures 8e and 8f, together with figures 2b-e and 6b-e, illustrate that the sign and magnitude of elevation dependent warming is seasonally dependent over the Rocky mountains, with temperatures increasing as a function of elevation during January, and decreasing below 600 mb during July.

Changes in the vertical distribution of clouds and latent heating during January and more so during July have an impact on the net short wave radiation absorbed at the surface, which influences snow melt. However, it is also necessary to take into account changes during spring and fall to create a model of Rocky mountain snow mass balance due to the fact that radiative snow melt occurs primarily when surface air temperatures are above freezing (otherwise absorbed radiation will be largely balanced by a sensible heat flux rather than a latent heat flux). During periods when temperatures are generally well above or below freezing (cf, Figs. 2a and 4a), snow mass balance is a weak function of temperature. During the spring and fall, however, temperatures oscillate about the freezing mark frequently, making snow melt a much stronger function of temperature. Hence, global warming-related changes during the spring and fall are crucial for the determination of changes in net snow accumulation in a warmer climate.

3b: Annual Results

Annual mean surface temperatures gradually increase from control values and, as in the July results (cf. Figs. 2b-e), the largest increases are found over the continental interior rather than over the ocean (Figs. 9a-e). As presented earlier, high elevations experience a higher amplitude warming during January (cf. Fig. 6b-e) and a reduced

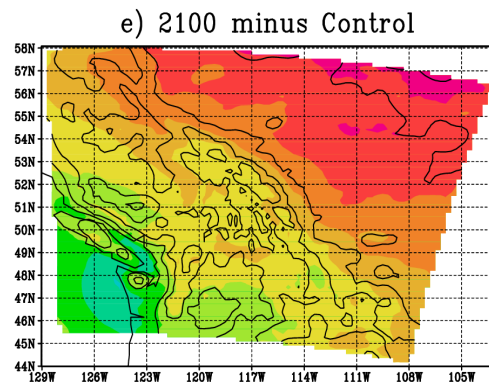
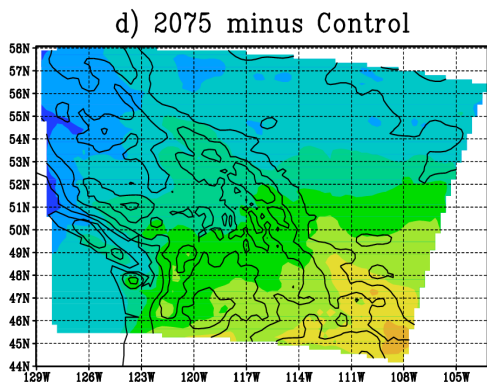
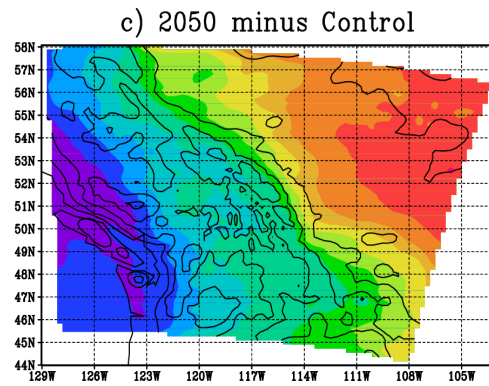
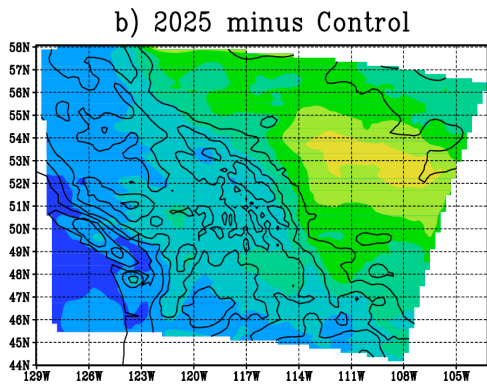
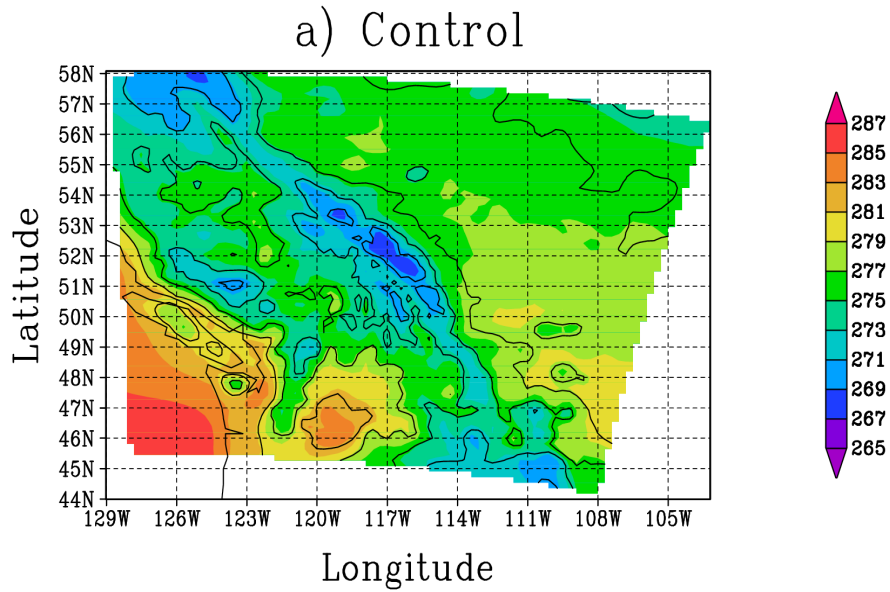


Figure 9: The domain 2 annual surface temperature (K) for a) the control simulation. b) The domain 2 annual 2025 mean surface temperatures minus a. c) As in b but for 2050. d) As in b but for 2075. e) As in b but for 2100. Results are overlaid on 250, 500, 750, 1000, 1250, 1500, 1750, 2000, 2250, and 2500 m elevation contours for reference.

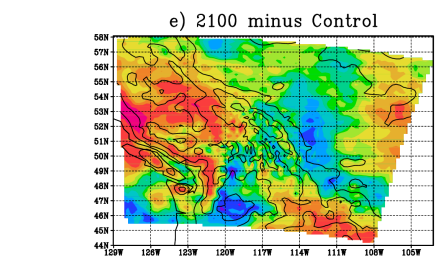
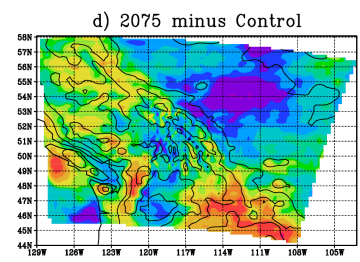
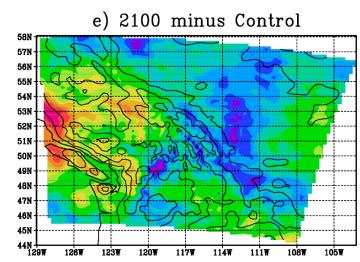
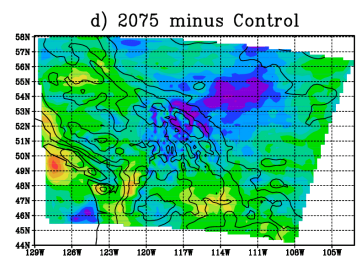
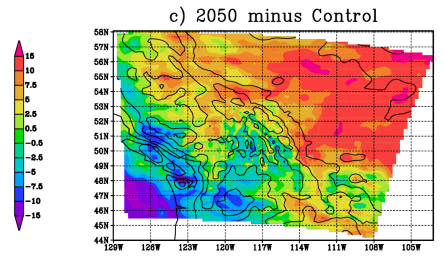
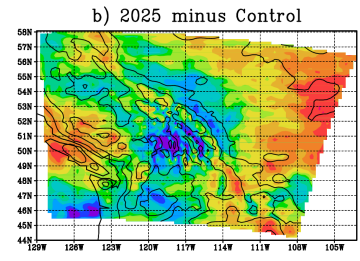
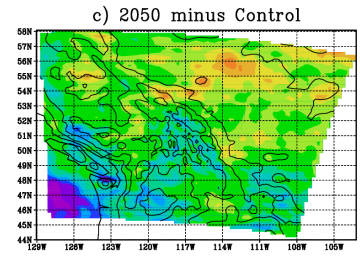
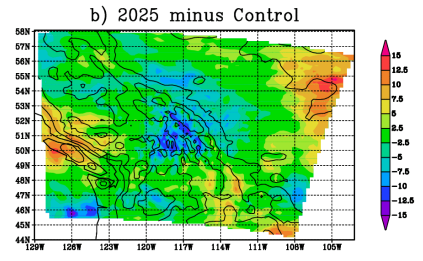
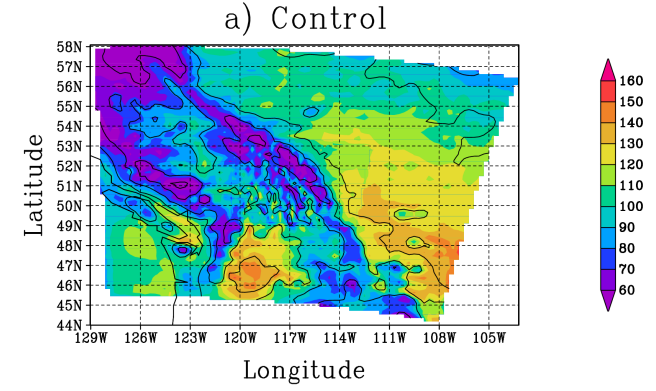
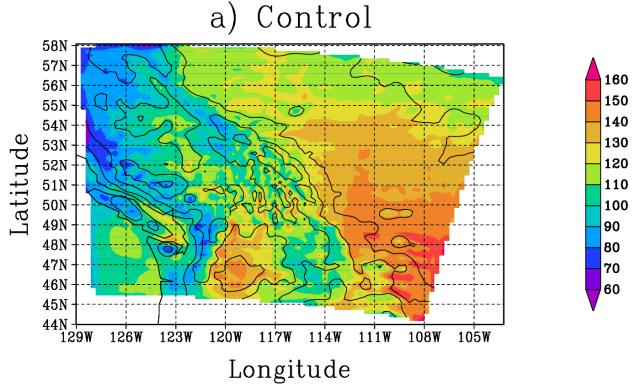


Figure 10: a) The control simulation annual mean short wave radiation (W/m^2). b) The 2025 mean minus a. c) As in b but for 2050. d) As in b but for 2075. e) As in b but for 2100. Results are overlaid on 250, 500, 750, 1000, 1250, 1500 1750, 2000, 2250 and 2500 m elevation contours for reference.

Figure 11: a) The control simulation annual mean short wave radiation at temperatures above freezing (W/m^2). b) The 2025 mean minus a. c) As in b but for 2050. d) As in b but for 2075. e) As in b but for 2100. Results are overlaid on 250, 500, 750, 1000, 1250, 1500 1750, 2000, 2250 and 2500 m elevation contours for reference.

warming during July (cf. Fig. 2b-e). Due to the contrasting seasonal signals, the altitude-dependent warming mechanism is difficult to detect in the annual mean results (Figs. 9b-e). Although these temperature increases will have an impact on snow mass balance directly through sensible heat fluxes, they are also important to the length of the radiative melt season.

As is the case with January precipitation (cf. Fig. 5a), annual mean insolation is shown to be highly dependent on the presence, or lack thereof of orographic uplift and consequent cloud cover (Fig. 10a). Surface insolation is greatest East of the Rocky mountains and at lower elevations and weakest over the coast mountains and the Rockies, where low-mid level cloud formation by orographic forcing is prominent (Fig. 10a). Changes in July surface solar radiation in time show the greatest increases over the Western slopes of the Coast mountains, the Rockies, and the Cascades and decreases over the Eastern slopes, consistent with chapter 1 (cf. Fig. 1.12b). This result is caused by a lengthening summer season and the associated summertime downsloping surface winds which occur then (cf. Fig. 2a). Eastern slopes and the very highest elevations of the Rocky mountains experience decreasing surface solar radiation, with the strongest signals in 2075 and 2100 (Figs. 10b-e). Although annual mean surface radiation decreases below control values (Figs. 10b-e), temperatures distinctly increase through the 100 year period (Figs. 2b-e, 4b-e, 9e-f) and this has an effect on potential radiative snow melt.

Since intense incident surface short wave radiation at temperatures below freezing is infrequent and causes minimal snow melt due to sensible heat fluxes, it is useful to consider only the incident short wave radiation when surface air temperatures are above freezing. Doing so reduces annual mean insolation by a negligible amount off the coast of British Columbia, by approximately 10% over the plains of Alberta, and by 20% at elevations above 2000 m (cf. Figs. 10a and 11a). Although net surface solar radiation decreases at higher elevations in a warmer climate (cf. Fig. 10b-e), the amount of

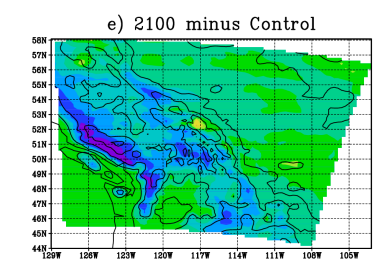
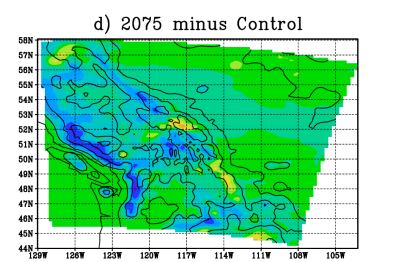
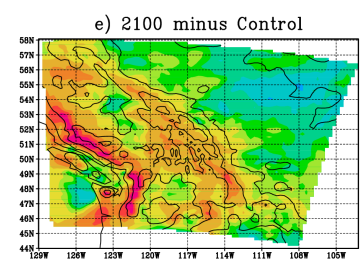
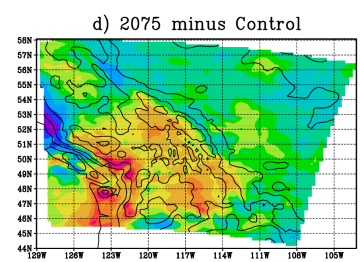
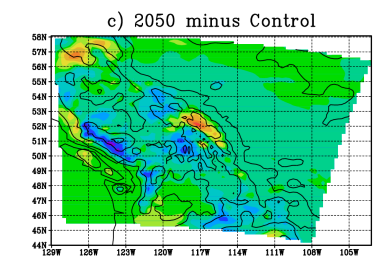
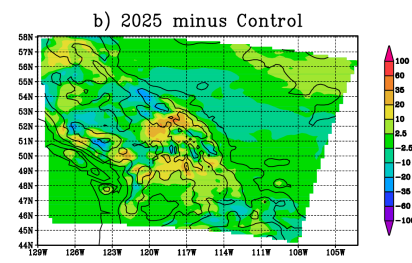
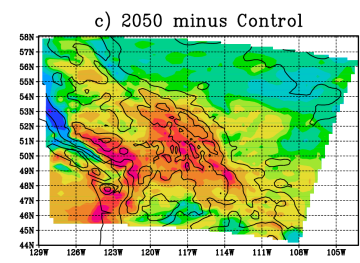
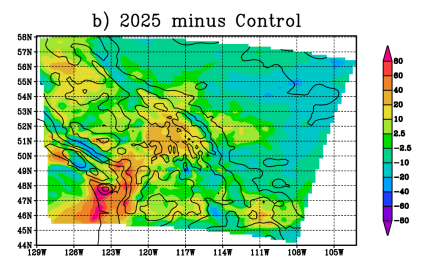
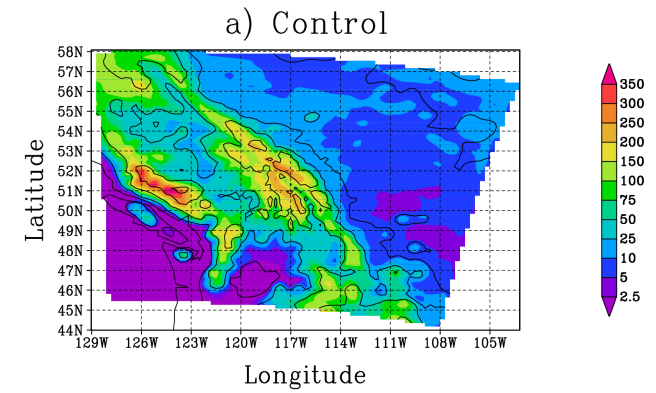
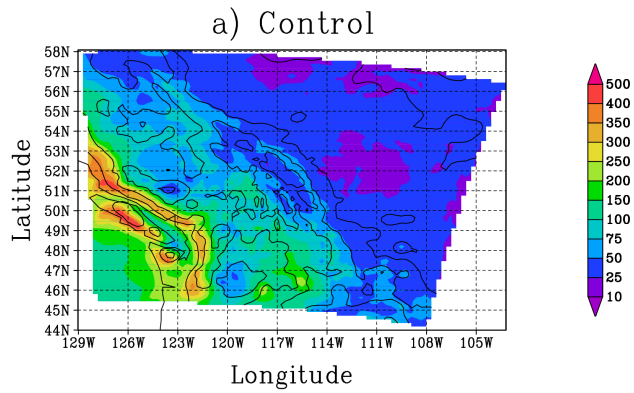


Figure 12: a) The control annual mean rainfall (cm). b) The 2025 annual mean rainfall minus a. c) As in b but for 2050. d) As in b but for 2075. e) As in b but for 2100. Results are overlaid on 250, 500, 750, 1000, 1250, 1500 1750, 2000, 2250 and 2500 m elevation contours for reference.

Figure 13: a) The control annual mean snowfall (cm). b) The 2025 annual mean snowfall minus a. c) As in b but for 2050. d) As in b but for 2075. e) As in b but for 2100. Results are overlaid on 250, 500, 750, 1000, 1250, 1500 1750, 2000, 2250 and 2500 m elevation contours for reference.

radiation present at the surface at temperatures above freezing remains relatively constant or increases due to the rising temperatures, particularly at higher elevations (Figs. 9b-e). This partially negates the effects of increasing cloud cover (Figs 8c-d) and causes changes in short wave radiative melt to be roughly neutral in a warmer climate, despite increases in cloud cover.

Another consequence of the increasing temperatures is that more precipitation falls as rain. A changeover of precipitation type is simulated in 2050, when annual rainfall over the Rocky mountains is significantly greater than in the control simulation (Fig. 12c). The simulated trends in increasing rainfall are primarily a result of the conversion of snow to rain in the gradually warming climate, but are compounded by the overall trend in increasing winter precipitation (Fig. 2b-e). By 2075 and 2100 the higher elevations of the Coast mountains and Northerly locations experience substantial increases in rainfall and these will lead to increased melt because the rain contains thermal energy that enhances snow melt.

Although simulated rainfall shows fairly consistent increases in most places through the 21st century (cf. Fig. 12b-e), snowfall initially increases at high elevation until 2050, and decreases thereafter (Fig. 13b-e). In contrast, decreases in January snowfall at higher elevations are not apparent until 2100 (Fig. 5b-e). Annual snowfall is therefore more sensitive to global warming in the short term than January snowfall. Decreases in simulated snowfall occur below progressively higher elevations as the century progresses, which shows that snow lines associated with synoptic systems are rising, regardless of snowfall amounts at higher elevations. The significant decrease in snowfall at high elevation by 2100 (Fig. 13e) is caused by the cumulative temperature increases (Fig. 9b-e) and the consequent dominance of rain over snow. In this study, the elevations above which snowfall increases is lower than that in the study of Kim et al. (2002), in which snowfall increases only above elevations of 2500 m in California. In

these simulations, this elevation rises from roughly 500m to 2000 m from 2025 through 2100 (Fig. 5b-e). This elevation discrepancy is not surprising considering that our study area is at a higher latitude than California, meaning that surface temperatures are colder in both the present climate and the future climate.

Although snowfall initially increases at high elevation (Figs. 5b-e and 13b-e), the potential for melt also increases significantly in a warmer climate (Figs. 9b-e, 11b-e). In the next section potential snowfall, short wave radiative melt, long wave radiative melt, melt due to sensible heat fluxes, and melt due to rainfall are taken into account in an effort to quantify potential changes to the Rocky mountain cryosphere in the 21st century.

3c: Snow mass balance

Model results indicate increases in snowfall at higher elevations (despite increases in temperature) up until 2075 for the January mean and until 2050 for the annual mean, with subsequent decreases in both cases (Figs. 5b-e, 11b-e). This leads to short term increases in positive net snow accumulation in the Rockies. However, increasing temperatures enable a lengthening of the radiative melt season and increasing sensible heat fluxes into snow/ice masses in the Rockies (Figs. 9b-e, 11b-e). Furthermore, increases in rainfall and long wave radiation (Figs. 9b-e, 12b-e) contribute negatively to snow and ice mass balance. In this section, the effects of all of these opposing negative and positive feedbacks will be summarized to determine how climate changes impact net snow accumulation in the Rocky mountains in a warmer climate.

Given the annual data from the MM simulation, a simple calculation is performed to yield an estimate of annual snow mass balance M (in mm/year), as a function of snowfall S (in mm/year water equivalent), incoming long wave radiation J_l (W/m^2), sensible heat flux C (W/m^2), incoming short wave radiation J_s (W/m^2) and rainfall rate r . The idealized system of accumulation and ablation is described by the following formula,

$$(3.6) \quad M = S - \frac{1}{L_{yr}} \int H(T(t) - T_f) \gamma(t) dt \quad ,$$

with

$$(3.7) \quad \gamma(t) = J_s(t) A_s + C(t) + H(J_l(t) - J_o)(J_l(t) - J_o) A_l + c_{pw} r(t) (T(t) - T_f)$$

and $H(x) = \begin{cases} 1 & \text{if } x \geq 0 \\ 0 & \text{if } x < 0 \end{cases}$ being the step function. J and A are the average incident

radiations and fraction of incident radiation absorbed, respectively, and the subscripts s and l denote short and long wave components, respectively. J_o is the outgoing long wave radiation from an ice surface at 0°C, 315 W/m². L_f is the latent heat of fusion of water. c_{pw} and T_f are the specific heat capacity at constant pressure and freezing temperature of water (273.15 K), respectively. dt is the output data resolution of 1 hour.

The sensible heat flux from a snow surface for an air mass with neutral stability, C, is handled as in Munro (1991):

$$(3.8) \quad C(t) = \rho_a(t) c_{pa} k_v^2 \frac{u(T(t) - T_f)}{[\ln(z/z_o)]^2}$$

with ρ_a the air density (kg/m³), c_{pa} the specific heat capacity of air at constant pressure, k_v is the von Karman constant, u is the wind speed (m/s), z is the above ground height (taken to be 2 m), and z_o is the thermal roughness length of a smooth, wet snow surface (taken to be a constant 0.1 mm based on the findings of Calanca (2001)).

The albedo of snow varies significantly, depending on snowfall, melt, and snow age and the value of 70% used here is taken to be a reasonable average value for old, wet snow (Warren 1982). This is typical for snow patches at higher elevations during extended periods of melt. Although using a relatively low albedo during the winter is questionable, the possibility of melt occurring then is negated by the requirement that melt occur only when surface temperatures are above freezing. Furthermore, insolation during these months is generally weak. Seasonal snow melt can therefore be calculated to

a reasonable accuracy using a constant albedo of 70% as a first approximation.

The terms in equation 3.6 can be considered independently, to determine what role each plays in total snow melt at any given location. At elevations above 2000 m in the Rocky mountains, sensible heat fluxes contribute about 15% to total annual melt, long wave radiation contributes about 5%, and rainfall contributes less than 1% (cf. Figs. 11a, 14a, 14c, 14e). However, at elevations below 1000 m, these fractions increase substantially, with sensible heat fluxes contributing 30%, long wave radiation contributing up to 20%, and rainfall contributing about 5% to total annual melt. Melt due to sensible heat fluxes, long wave radiative melt, and melt due to rainfall all increase rapidly with decreasing elevation, and all of them also increase in a warmer climate, even at higher elevations (Figs. 14b, 14d, 14f). Although melt due to short wave radiation is indirectly affected by increasing temperatures, melt due to sensible heat fluxes, long wave fluxes, and rainfall are directly related to temperature. The sensible heat flux, in particular, plays a relatively small role in total melt in the control simulation (~15% in the Rockies cf. Figs. 11a and 14a), but increases substantially in a warmer climate, as a direct consequence of the warmer temperatures (cf. Fig. 9e). In fact, increases in melt due to sensible heat fluxes are greater than the combined increases in melt due to short wave radiation, long wave radiation, and rainfall (cf. Figs. 11e, 14b, 14d, 14f).

Higher net snow accumulation tends to occur in years when there is also higher snowfall (cf. Figs. 11 and 15), indicating that glacial mass balance is more strongly correlated with snowfall than with temperature (cf. Figs. 11 and 15). This result is consistent with the observations of Bitz and Battisti (1999), who found strong positive correlations between mass balance and precipitation anomalies and weak negative correlations between mass balance and temperature anomalies for several glaciers in the Canadian Rockies. The highest annual net snow accumulation (of more than 2 meters water equivalent per year) is found at the highest model elevations (Fig. 15a). Changes in

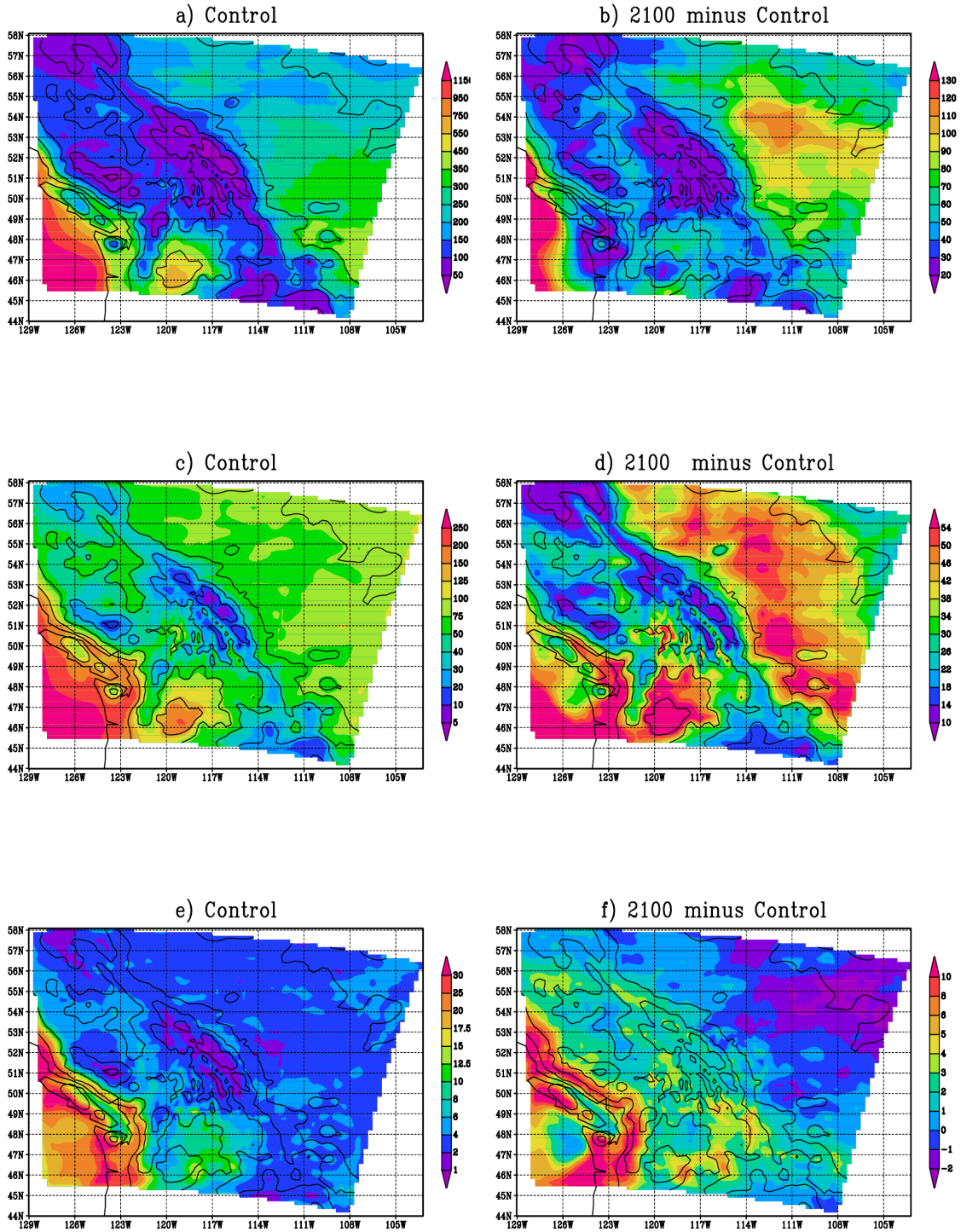


Figure 14: Annual mean terms in the mass balance equation (cm). a) The control simulation sensible heat flux. b) The 2100 mean sensible heat flux minus Control. c) As in a but longwave flux. d) As in b but for long wave flux. e) As in a but for rainfall flux. f) As in b but for rainfall flux. Results are overlaid on 250, 500, 750, 1000, 1250, 1500, 1750, 2000, 2250, and 2500 m elevation contours for reference.

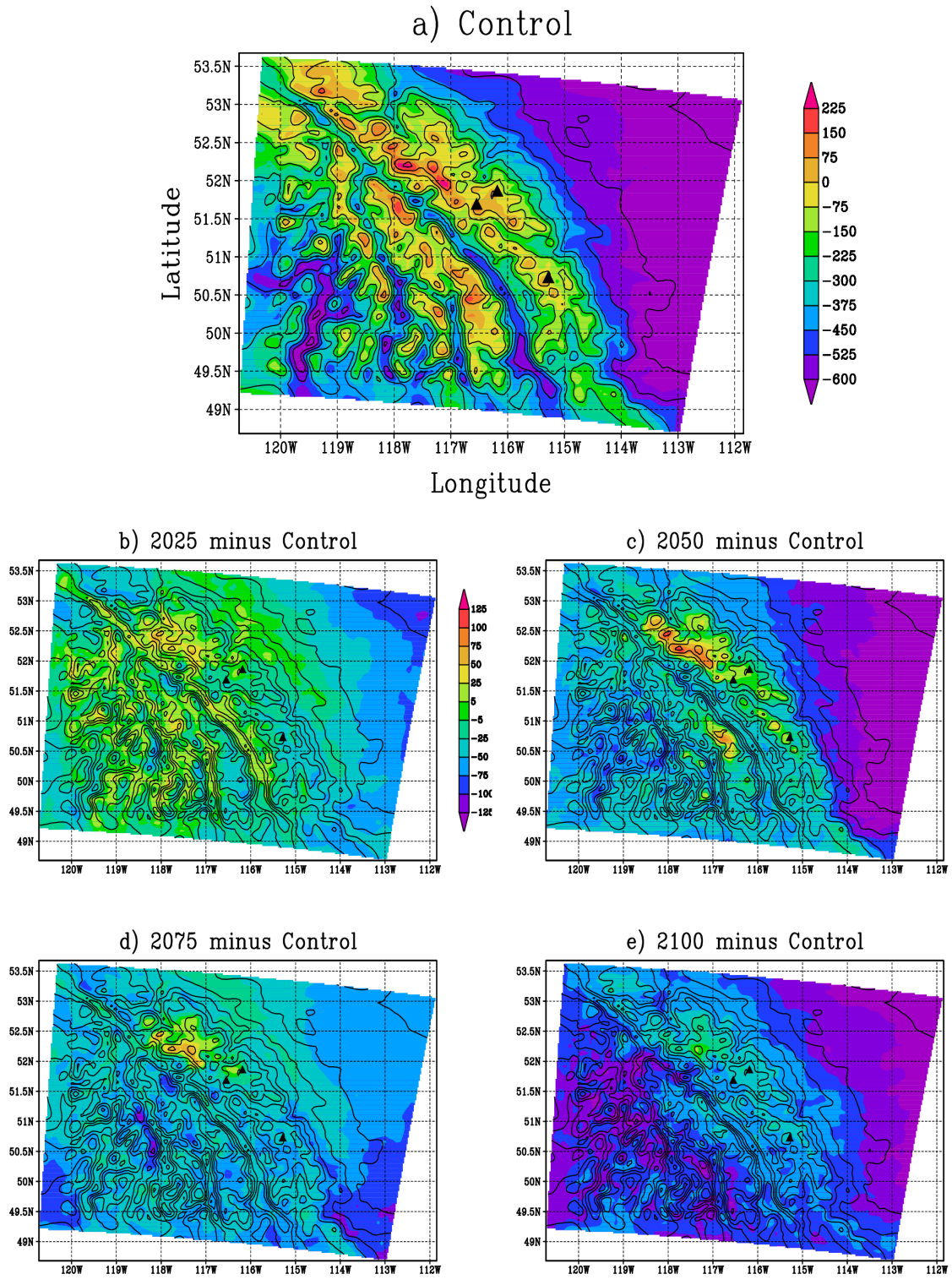


Figure 15: The domain 3 annual mass balance (cm) for a) the control simulation. b) The 2025 mean minus a. c) As in b but for 2050. c) As in b but for 2075. d) As in b but for 2100. The locations of the Haig, Peyto and Ram River glaciers are marked by the triangles. Results are overlaid on 250, 500, 750, 1000, 1250, 1500, 1750, 2000, 2250, and 2500 m elevation contours for reference.

snow mass balance over time initially show increases at high elevations in 2025 through 2075 (Fig. 15b-c), with simultaneous decreases at lower elevations in those years.

However, this period is followed by large decreases in 2100, primarily at low elevation with smaller decreases at high elevations (Fig. 15d-e). The trends are consistent with Schiefer et al. (2007), who noted areas of apparent thickening of glaciers at high elevations (despite wide-spread thinning at lower elevations) over the period 1985-1999 in satellite based estimates of glacier elevation change.

For simplicity the equilibrium line altitude (ELA) is chosen here as the elevation at which the 0 contour of annual snow mass balance lies (Fig. 15). Because the topography used in the MM is significantly smoother than real topography, the estimated position of the ELA will also be significantly smoother than in reality, encompassing a much broader area. Nevertheless, glaciated and non-glaciated regions are generally separated by the 0 contour (Fig. 16a) and a reasonable estimate of whether ELAs over a region are increasing or decreasing in time can be acquired from changes in the position of this contour. Initially, snowfall increases (Fig. 13b-e) combined with increasing short wave radiative melt (Fig. 11b-e) lead to fluctuating ELAs in many locations until 2050, with increases in net snow accumulation in some places and decreases in others (Fig. 16b-c). However, as temperatures continue to rise to the point where they begin to affect precipitation type (cf Fig. 9b-e and 13b-e), increasing ELAs are apparent over the entire region after 2050 (Fig. 16d-e). Although short term fluctuations in ELA are evident in some regions, average ELAs over the entire region rise steadily over the 21st century and the total area which receives positive snow mass balance is reduced to ~41% of its original size in 2100 (Table 1). Areas to the South, in the lee of the Rockies, and at lower elevations no longer receive positive net snow accumulation by 2100 (Fig. 16d). Areas in the vicinity of the Haig glacier in particular, experience no positive net snow accumulation in 2100 (Fig. 16e-e). Nevertheless, the Columbia icefields and many other

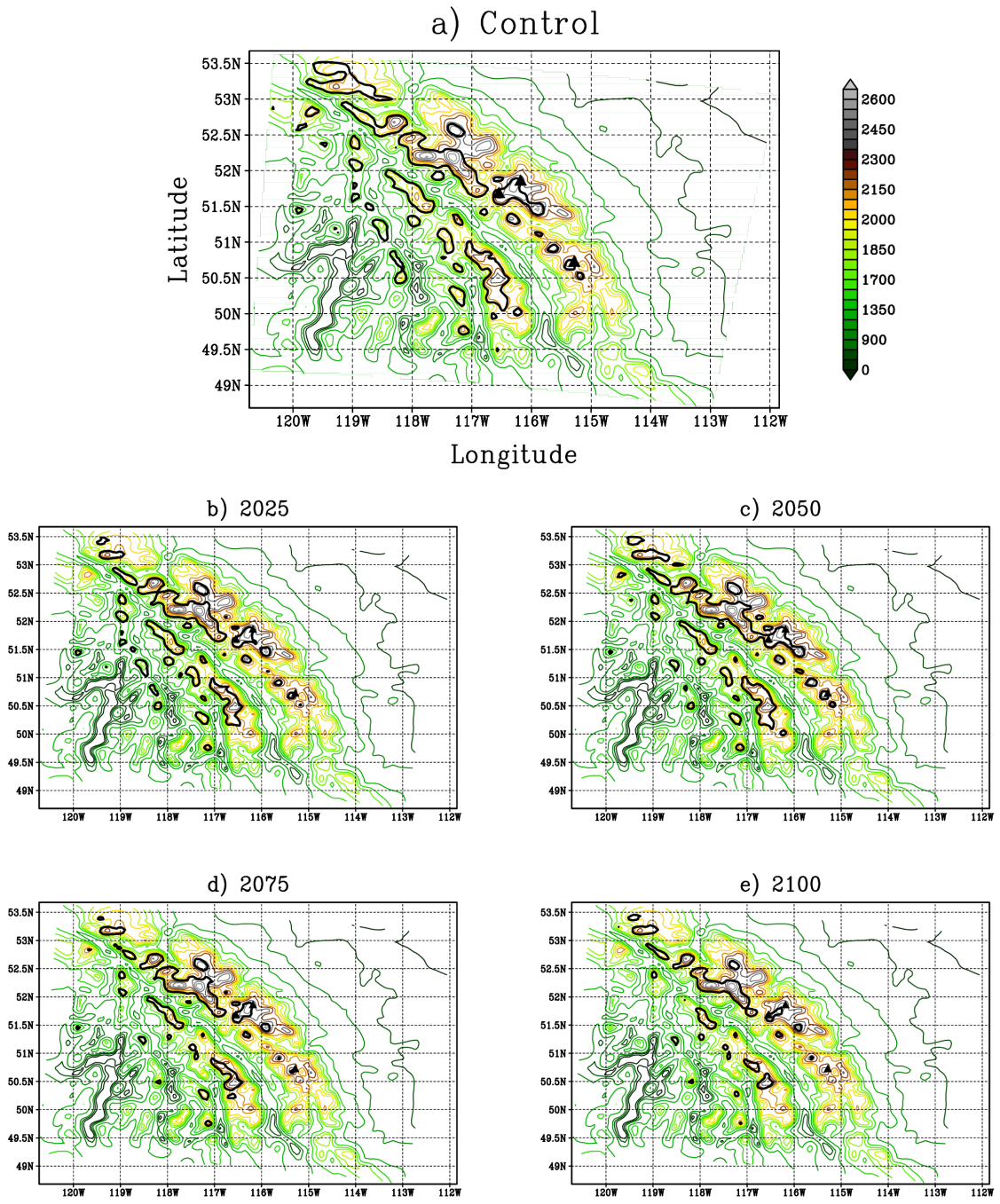


Figure 16: The equilibrium line plotted over topography (m) for a) the control simulation. b) The 2025 equilibrium line. c) As in b but for 2050. c) As in b but for 2075. d) As in b but for 2100. The locations of the Haig, Peyto and Ram River glaciers are marked by the triangles.

higher elevations of the Rockies and Columbia mountains continue to receive positive net snow accumulation through 2100 (Fig.16e).

	Control	2025	2050	2075	2100
Average ELA	2056.05	2073.74	2105.46	2128.81	2152.21
Positive M Area	11604.13	9231.24	10297.01	6508.51	4743.08

Table 1: Average domain 3 ELA (m) and areal coverage of positive net snow accumulation (km²). The ELA is defined here as the average of all elevations in domain 3 which have net annual accumulation of snow within 25 cm water equivalent of neutral.

Comparison of mass balance results from the glaciers of interest and the other 2 locations of interest illustrates the elevation dependence of mass balance in a warming climate (Table 2). In particular, the highest model grid points (the Columbia Icefields) initially experience increases in net snow accumulation, followed by a relatively static period between 2050 and 2075, and substantial reductions thereafter whereas the Hunters range experiences nearly continuously decreasing net snow mass balance through the 21st century. Between these two extremes are the Haig, the Ram River, and the Peyto glaciers, which experience fluctuating net snow accumulation until 2050 and decreases thereafter. The most pronounced decreases in net snow accumulation are simulated at Haig glacier, although the Peyto glacier also experiences large decreases (Table 2).

	Elevation	Control	2025	2050	2075	2100
Haig glacier	2300.03	-48.4	-321.9	-18.0	-428.1	-556.4
Peyto glacier	2326.78	642.29	395.99	642.86	375.85	199.15
Ram river	2458.41	44.7	83.8	104.3	-11.9	-281.5
Columbia I.	2518.54	726.7	1060.7	1282.7	1227.3	746
W. Columbia Mtn.	1578.44	-1061.2	-1173.8	-1539.9	-1700.8	-2080.8

Table 2: Elevation (m) and mass balance in time (mm water equivalent) for the Haig, Ram R., and Peyto glaciers, as well as the Columbia Icefields and a relatively high region of the Western Columbias.

4: Discussion

MM results are consistent with global trends in relative humidity, temperature, and precipitation results presented in Chapter 1 and with other studies of future climate (Dai et al. 1997, Zhang et al. 2000, Ingram 2002, Wetherald and Manabe 2003, Lorenz and DeWeaver 2007). The magnitude of projected temperature and precipitation increases in the 21st century are much higher than the observed changes during the 20th century (Zhang et al. 2000), suggesting that global warming-related changes are accelerating. This results in elevation-dependent non-linear trends in temperature, snowfall, and ultimately snow and ice mass balance in the Rocky mountains (Fig. 15b-e).

The MM also produces realistic regional and elevation-dependent variability not simulated in the GCM. In particular, the MM provides an improved representation of orographic processes (Leung and Ghan 1995, Andrieu et al. 1996, Esteban and Chen 2008) and precipitation increases by 10-15% in the Rocky mountains over the next century, close to the predictions of Chapter 1 (cf. Figs. 1.17, 1.18, 4b-e). In the short term, increases in snowfall (Fig. 4b-e) offset increases in melt caused by rising temperatures at many high elevation sites (Figs. 5b-e, 13b-e and Table 2). Other high elevations and high latitudes around the world have also experienced trends in increasing snowfall (Thompson and Pollard 1997, Masiokas et al. 2006, Box et al. 2006) and some studies of future climates have suggested that these trends will continue (Kim et al. 2002, Giorgi et al. 1994). However, the simulated climate in the Rocky mountains in the 2nd half of the 21st century is substantially warmer and more precipitation falls as rain, resulting in accelerated reductions in snow mass balance even at high elevations (cf. Figs. 12b-e, 13b-e, 15b-e). By 2100, this results in a substantial reduction in the area of the regions receiving net annual snow accumulation, with coverage reduced to 41% of its original control simulation size (Fig. 16b-e, Table 1). Besides producing a more regionally accurate temperature and precipitation field, the MM also makes evident some

unanticipated climate processes not simulated by the GCM, primarily resulting from orographically forced condensation in the higher resolution MM topography.

There is an elevation and seasonal dependence of temperature increases in the Rockies in the 21st century (Figs. 2b-e, 6b-e). During the winter season, temperature increases are amplified over high terrain (Fig. 6b-e), consistent with Kim et al. (2002) and Giorgi et al. (1994). This is primarily caused by increasing atmospheric water vapour and subsequent increases in condensation where orographic forcing occurs. The same phenomenon results in more moderate temperature increases at higher elevations during the summer (Fig. 2b-e) because increases in orographic cloud cover reduce surface solar radiation sufficiently enough to reduce temperatures (Figs. 2b-e, 8d, 10b-e). The seasonality of these changes are a result of increasing middle level cloud in both seasons (Figs. 8c-d), and the competing effects of clouds on absorbed solar radiation and the latent heat release which occurs during their formation.

5: Conclusion

Although ELAs gradually increase and there is a reduction in the area receiving positive net snow accumulation in a warmer climate from control to 2100 (cf. Tables 1 and 2), many of the higher elevations in the Rocky mountains continue to experience positive snow mass balance despite the temperature increases (Fig. 16e). The divergence of snow mass balance results for different elevations in a warming climate (illustrates Table 2) illustrates the degree of control elevation has on potential net snow accumulation. They also illustrates the need to use high resolution mesoscale modelling in the consideration of potential glacier changes in future climates over mountainous topography since higher resolution models automatically incorporate a more complete range of elevations and therefore climatic conditions.

Despite the temperature increases (Fig. 9b-e) ELAs in some regions are initially

stable or even decreasing (Fig. 16b-e). However, glacial expansion does not necessarily ensue. The meteorological models employed here do not take into account several essential aspects of glacial dynamics and glacial melt. Primarily, increased snowfall at higher elevation and increased melt at all elevations would result in greater along-glacier mass balance gradients (Figs. 5b-e, 9b-e, 11b-e, 14) and because the maximum strain rate in ice flow increases with increasing ice temperature (Glen 1955), glaciers in a warmer climate are characterized by higher downhill flow speeds. Furthermore, glacial ice has a significantly lower albedo than snow, and because of this, ice will be affected to a greater degree than snow by short wave radiation under a given temperature increase (Eq. 3.6). Finally, glacial ice flows downhill into warmer regions, another mechanism for more rapid melt than snow under equivalent solar forcing. The numerical results presented here must therefore be used in future work as boundary condition forcing for glaciological models in order to better determine the impact of increasing CO₂ concentrations on the glaciers in the Western Cordillera. The behavior of ice masses under the different forcings simulated here (such as increasing temperatures and more precipitation), requires the use of thermomechanical ice models such as in Huybrechts and de Wolfe (1999), and Otto-Bliesner et al. (2006) and is the subject of future research.

Final Remarks:

The impact of such meteorological forcings on the nature of glacial flow (and thus the glacier terminus position) can only be determined through numerical modeling of ice masses and so further studies must be performed to fully answer this question.

Nevertheless, this study makes clear some essential aspects of high elevation Rocky mountain climate change. Namely, snowfall trends and hence glacial mass balance trends can be highly non-linear in an increasing carbon dioxide atmosphere. To be specific, in the short term snowfall increases at high elevations and high latitudes, because of global increases in temperature and atmospheric water vapour and the subsequent increases in snowfall. In the long term, however, snowfall amounts in these regions decline, as temperatures increase sufficiently enough to modify precipitation type. This illustrates that there exists a threshold temperature required to change large portions of precipitation from snowfall to rainfall. Hence, although some glaciers may be stable, or even advancing in the short term (i.e. the next 50 years or so), these trends will eventually give way to a more rapid retreat once this threshold temperature is achieved. Nevertheless, areas of positive mass balance are still present in 2100 in the high elevations of the Columbias and the Rockies, meaning that a complete loss of all glacial ice in the Rockies by the end of the 21st century under a conservative emission scenario is unlikely.

A detailed climate forecast for specific locations on the planet should include ensemble results from multiple GCMs and RCMs, thus minimizing standard error. In this manner, quantification of the potential altitude dependence of temperature, precipitation, and glacial mass balance changes in a warmer climate for different regions could be achieved. Global and regional climate modeling combined with glacier modeling has the potential to accurately predict, for all of the world's glaciers, the terminus position and thickness through the 21st century. This would give policy makers and planners the ability to take such climate changes into account, potentially improving long term

standards of living.

References

Andrieu H., M. French, V. Thauvin, W. Krajewski, 1996: Adaptation and application of a quantitative rainfall forecasting model in a mountainous region: *Journal of Hydrology*, 198, 243-259.

Bitz C.M. and Battisti D.S., 1999. Interannual to Decadal Variability in Climate and the Glacier Mass Balance in Washington, Western Canada, and Alaska. *Journal of Climate*. pp. 3181–3196.

Boer G. W., B. Yu, S. Kim, G. Flato, 2004: Is there observational support for an El Niño-like pattern of future global warming?, *Geophysical Research letters*, 31, L06201.

Bolton D., 1980: The Computation of Equivalent potential temperature., *Monthly Weather Review*, 108, 1046-1053.

Box J. E., D. Bromwich, B. Veenhuis, L. Bai, S. Wang, J. Stroeve, T. Haran, J. Rogers, K. Steffen, 2006: Greenland Ice Sheet Surface Mass Balance Variability (1988–2004) from Calibrated Polar MM5 Output. *Journal of Climate*, 19, 2783–2800.

Broccoli A., Manabe S., 1992: The Effects of Orography on Northern Hemisphere Midlatitude Dry Climates., *Journal of Climate*., 5, 1181-1201.

Bromwich D.H.,L. Bai, G.G. Bjarnason, 2005. High-Resolution Regional Climate Simulations over Iceland Using Polar MM5. *Monthly Weather Review*. pp. 3527–3547.

Bush A. B. G., W. R. Peltier, 1994: Tropopause Folds and Synoptic-Scale Baroclinic

Wave Life Cycles. *Journal of Atmospheric Science*, 51, 1581-1604.

Bush A. B. G., 2007: Extratropical Influences on the El Niño–Southern Oscillation through the Late Quaternary., *Journal of Climate*, 20, 788-800.

Calanca P., 2001: A note on the roughness length over melting snow and ice. *Quarterly Journal of the Royal Meteorological Society*, 127, 255-260.

Callendar G. S., 1938: The Artificial Production of CO₂ and its Influence on Temperature., *Quarterly Journal of the Royal Meteorological Society*, 64, 223-240.

Cash B. A., P. J. Kushner, G. K. Vallis, 2004: Zonal Asymmetries, Teleconnections, and Anular Patterns in a GCM. *Journal of Atmospheric Sciences*, 62, 207-219.

Dai A., I. Fung, A. Del Genio, 1997: Surface Observed Global Land Precipitation Variations during 1900–88. *Journal of Climate*, 10, 2943–2962.

Dai A., T. Wigley, B. Boville, J. Kiehl, L. Buja, 2001: Climates of the twentieth and twenty-first centuries simulated by the NCAR climate system model. *Journal of Climate*, 2001, 485-519.

Dai A., 2006: Recent Climatology, Variability, and Trends in Global Surface Humidity. *Journal of Climate*, 19, 3589–3606.

Esteban M. A., Chen Y., 2008: The Impact of Trade Wind Strength on Precipitation over the Windward Side of the Island of Hawaii., *Monthly Weather Review*, 136, 913–928.

Fealy R., J. Sweeney, 2007: Identification of frequency changes in synoptic circulation types and consequences for glacier mass balance in Norway. *Norsk geografisk tidsskrift*, 61, 76-91.

Flato G., G. Boer, 2006: Warming Asymmetry in Climate Change Simulations. *Geophysical Research Letters*, 28, 195-198.

Geng Q., M. Sugi, 2003: Possible change of extratropical cyclone activity due to enhanced greenhouse gases and sulfate aerosols - Study with a high-resolution AGCM. *Journal of Climate*, 16, 2262-2274.

Giorgi F., C. S. Brodeur, and G. T. Bates, 1994: Regional climate change scenarios over the United States produced with a nested regional climate model: Spatial and seasonal characteristics. *Journal of Climate*, 7, 375–399.

Giorgi F., Marinucci M.R., Visconte G., 1992: A 2XCO₂ Climate Change Scenario Over Europe Generated Using a Limited Area Model Nested in a General Circulation Model 2. *Climate Change Scenario.*, *Journal of Geophysical Research*, 97, 10,011-10,028.

Giorgi F., J. W. Hurrell, M. R. Marinucci, and M. Beniston, 1997: Elevation dependency of the surface climate signal: A model study. *Journal of Climate*, 288–296.

Glen J. W., 1955: The creep of polycrystalline ice. *Proceedings of the Royal Society of London. Series A, Mathematical and Physical Sciences*, 228, 519-538.

Gordon C. T., and W. Stern, 1982: A description of the GFDL global spectral model. *Monthly Weather Review*, 110, 625-644.

Hansen J., D. Johnson, A. Lacis, S. Lebedeff, P. Lee, D. Rind, G. Russel, 1981: Climate Impact of Increasing Atmospheric Carbon Dioxide. *Science*, 213, 957-966

Hansen, J., A. Lacis, D. Rind, G. Russel, P. Stone, I. Fung, R. Ruedy, J. Lerner, 1984: Climate sensitivity analysis of feedback mechanisms. *Climate Processes and Climate Sensitivity. Geophysical Monographs*, 29, 130-163.

Held I., B. Soden, 2006: Robust Responses of the Hydrological Cycle to Global Warming., *Journal of Climate*, 19, 5686-5699.

Hewitt K., 2005: The Karakoram anomaly? Glacier expansion and the 'elevation effect,' *Karakoram Himalaya, Mountain Research and Development*, 25, 332-340.

Hock R., 2003: Temperature index melt modelling in mountain areas. *Journal of Hydrology*, 282, 104-115.

Holland M., Bitz C., 2003: Polar amplification of climate change in coupled models. *Climate Dynamics*, 21, 221-232.

Horel J.D. and Wallace J.M., 1980. Planetary-Scale Atmospheric Phenomena Associated with the Southern Oscillation. *Monthly Weather Review*. pp. 813–829.

Huybrechts P., J. de Wolde, 1999. The Dynamic Response of the Greenland and

Antarctic Ice Sheets to Multiple-Century Climatic Warming. *Journal of Climate*. pp. 2169–2188.

Ingram W. J., 2002: On the robustness of the water vapor feedback: GCM vertical resolution and formulation. *Journal of Climate*, 15, 917–921.

IPCC (Intergovernmental Panel on Climate Change), cited 2007: IPCC WG1 AR4 Report. [Available online at <http://ipcc-wg1.ucar.edu/wg1/wg1-report.html>].

Johansson B., D. Chen, 2003: The influence of wind and topography on precipitation distribution in Sweden: Statistical Analysis and Modelling. *International Journal of Climatology*, 23, 1523 - 1535.

Johns T. C., Gregory J. M., Ingram W. J., Johnson C. E., Jones A., Lowe J. A., Mitchell J. F. B., Roberts B. L., Sexton D. M. H., Stevenson D. S., Tett S. F. B., Woodage M. J., 2003: Anthropogenic climate change from 1860 – 2100 simulated with the HadCM3 under updated emission scenarios. *Climate Dynamics*, 20, 583-612.

Kalnay E., M. Kanamitsu, R. Kistler, W. Collins, D. Deavon, L. Gandin, M. Iredell, S. Saha, G. White, J. Woollen, Y. Zhu, M. Chelliah, W. Ebisuzaki, W. Higgins, J. Janowiak, K. C. Mo, C. Ropelewski, J. Wang, A. Leetmaa, R. Reynolds, R. Jenne, D. Joseph, 1996: The NCEP/NCAR 40-year Reanalysis Project. *Bulletin of the American Meteorological Society*, 1996, 437-471.

Kim J., T. Kim, R. Arritt, N. Miller, 2002: Impacts of Increased Atmospheric CO₂ on the

Hydroclimate of the Western United States. *Journal of Climate*, 15, 1926–1942.

Leung L. R., S. J. Ghan, 1995: A Subgrid Parameterization of Orographic Precipitation. *Theoretical and Applied Climatology*, 52, 95-118.

Leung L. R., S. J. Ghan, 1999b: Pacific Northwest climate sensitivity simulated by a regional climate model driven by a GCM. Part II: $2\times\text{CO}_2$ simulations. *Journal of Climate*, 12, 2031–2053.

Lorenz D., E. DeWeaver, 2007: The Response of the Extratropical Hydrological Cycle to Global Warming. *Journal of Climate*, 20, 3470–3484.

Manabe S., 1969: Climate and the ocean circulation: 1. The atmospheric circulation and the hydrology of the Earth's surface. *Monthly weather review*, 97, 739-774.

Manabe S., and R. T. Wetherald, 1975: The effects of doubling the CO_2 concentration on the climate of a general circulation model. *Journal of Atmospheric Science*, 32, 3–15.

Manabe S., R. J. Stouffer, M. J. Spelman, K. Bryan, 1991: Transient Responses of a Coupled Ocean-Atmosphere to Gradual Changes of Atmospheric CO_2 . Part 1: Annual Mean Response., *Journal of Climate*, 4, 785-818.

Manabe S., M. J. Spelman, R. J. Stouffer, 1992: Transient Responses of a Coupled Ocean-Atmosphere to Gradual Changes of Atmospheric CO_2 . Part 2: Seasonal Response., *Journal of Climate*, 4, 785-818.

Manabe S., R. J. Stouffer, 1994: Multi-Century Response of a Coupled Ocean-Atmosphere Model to an Increase of Atmospheric Carbon Dioxide., *Journal of Climate*, 7, 5-23.

Marshall S., 2003: The Predictability of Winter Snow Cover over the Western United States. *Journal of Climate*, 16, 1062–1073.

Masiokas M., R. Villalba, B. Luckman, C. Le Quesne, J. Aravena, 2006: Snowpack variations in the central Andes of Argentina and Chile, 1951-2005: Large-scale atmospheric influences and implications for water resources in the region. *Journal of Climate*, 19, 6334-6352.

Meehl G. A., W. M. Washington, B. D. Santer, W. D. Collins, J. M. Arblaster, A. Hu, D. M. Lawrence, H. Teng, L. E. Buja, W. G. Strang, 2005: Climate Change Projections for the Twenty-first century and Climate Change Commitment in the CCSM3. *Journal of Climate*, 19, 1597-2616.

Meehl G., H. Teng, G. Branstator, 2006: Future change of El Niño in two global coupled climate models. *Climate Dynamics*, 26, 549-566.

Meehl G., H. Teng, 2007: Multi-model changes in El Niño teleconnections over North America in a future warmer climate. *Climate Dynamics*, 29, 779-790.

Molnia B., 2006: Late nineteenth to early twenty-first century behavior of Alaskan glaciers as indicators of changing regional climate. *Global and planetary change*, 56, 23-56.

Munro S., 1990: Comparison of Melt Energy Computations and Ablatometer Measurements on Melting Ice and Snow. *Arctic and Alpine Research*, 22, 153-162.

Munro S., 1991: A Surface Energy Exchange Model of Glacier Melt and Net Mass Balance. *International Journal of Climatology*, 11, 689-700.

Muskett R. R., Lingle C. S., Sauber J. M., Post A. S., Tangborn W. G., Rabus B. T., 2008: Surging, accelerating surface lowering and volume reduction of the Malaspina glacier system, Alaska, USA, and Yukon, Canada, from 1972 to 2006. *Journal of Glaciology*, 54, 788-800.

Navarra A., M. Biasutti, S. Gualdi, E. Roeckner, U. Schlese, U. Schulzweida, 2000: Sensitivity experiments to mountain representations in spectral models. *Annali di geofisica*, 43, 59-584.

Oerlemans J., 2005: Extracting a climate signal from 169 glacier records. *Science*, 308(5722), 675-677.

Ommanney S.L., 1984. *Glaciers of North America – Glaciers of Canada – Glaciers of the Canadian Rockies*. U.S. Geological Survey Professional Paper. 1386-J-1.

Otto-Bliesner B. L., S. J. Marshall, J. T. Overpeck, G. H. Miller, A. Hu, CAPE Last Interglacial Project members, 2006: Simulating Arctic Climate Warmth and Icefield Retreat in the Last Interglaciation. *Science*, 311, 1751-1753.

Pacanowski R. C., 1995: MOM2 documentation, user's guide, and reference manual. GFDL Ocean Group Tech. Rep. 3, 232 pp.

Plummer D., Caya D., Frigon A., Cote H., Giguere M., Paquin D., Biner S., Harvey R., 2006: Climate and Climate Change over North America as Simulated by the Canadian RCM., *Journal of Climate.*, 19, 3112-3132.

Radic V. and Hock R., 2006. Modelling future glacier mass balance and volume changes using ERA-40 reanalysis and climate models: A sensitivity study at Storglaciaren, Sweden. *Journal of Geophysical Research.* Vol. 111, F03003.

Rinke A., Dethloff K., 2008: Simulated circum-Arctic climate changes by the end of the 21st century., *Global and planetary change*, 62, 173-186.

Ross J., W. Elliot, 2001: Radiosonde-Based Northern Hemisphere Tropospheric Water Vapor Trends., *Journal of Climate.*, 14, 1602–1612.

Santer B. D., K. E. Taylor, T. M. Wigley, J. E. Penner, P. D. Jones, U. Cubasch, 1995: Detection of climate change and attribution of causes. *Climate Change 1995: The Science of Climate Change*, Cambridge University Press, 407–443.

Schiefer E., B. Menuonos, R. Wheate, 2007: Recent volume loss of British Columbian glaciers, Canada. *Geophysical Research Letters*, 34, L16503.

Schneeberger C., H. Blatter, A. Abe-Ouchi, M. Wild, 2003: Modelling changes in the mass balance of glaciers of the Northern hemisphere for a transient 2xCO₂ scenario.

Journal of Hydrology, 282, 145-163.

Sidjak R. W., R. D. Wheate, 1999: Glacier mapping of the Illecillewaet icefield, British Columbia, Canada, using Landsat TM and digital elevation data. *International journal of remote sensing.*, 20, 273-284.

Stahl K., R. D. Moore, J.M. Shea, D. Hutchinson, A.J. Cannon, 2008: Coupled modelling of glacier and streamflow response to future climate scenarios. *Water Resources Research*, 44, W02422.

Stephens G., 1984: The Parameterization of Radiation for Numerical Weather Prediction and Climate Models. *Monthly Weather Review*, 112, 826-867.

Stouffer R., 2004: Time scales of climate response. *Journal of Climate.*, 17, 209-217.

Thompson S. L., D. Pollard, 1997: Greenland and Antarctic Mass Balances for Present and Doubled Atmospheric CO₂ from the GENESIS Version-2 Global Climate Model., *Journal of Climate*, 10, 871-900.

Thompson D. W., J. M. Wallace, 1998: The Arctic Oscillation signature in the wintertime geopotential height and temperature fields. *Geophysical Research Letters*, 25, 1297-1300.

Thompson D. W., J. M. Wallace, 2001: Regional Climate Impacts of the Northern Hemisphere Annular Mode. *Science*, 293, 85-89.

Trenberth K., 1997: The definition of El Niño. *Bulletin of the American Meteorological*

Society., 12, 2771.

Troen I. B., L. Mahrt, 1986: A Simple Model of the Atmospheric Boundary Layer; Sensivity to Surface Evaporation. *Boundary-Layer Meteorology*, 37, 129-148.

Vecchi G., B. Soden, A. Wittenberg, I. Held, A. Leetmaa, 2006: Weakening of tropical Pacific atmospheric circulation due to anthropogenic forcing. *Nature*, 441, 73-76.

Warren S., 1982: Optical properties of snow. *Reviews of geophysics*, 20, 67-89.

Watson E., B. Luckman, 2004: Tree-ring-based mass-balance estimates for the past 300 years at Peyto glacier, Alberta, Canada. *Quaternary Research*, 62, 9-18.

Wetherald R., S. Manabe, 2003: Simulation of hydrological changes associated with global warming. *Journal of Geophysical Research*, JD004253, 107, 4379.

Widmann M., C. Bretherton, E. Salathe Jr. 2003: Statistical Precipitation Downscaling over the Northwestern United States Using Numerically Simulated Precipitation as a Predictor. *Journal of Climate*, 15, 799-816.

Wilby R. L., 1997: Non-stationarity in Daily Precipitation Series: Implications for GCM Downscaling using Atmospheric Circulation Indices. *International Journal of Climatology*, 17, 439-454.

Wilby R. L., T. M. L. Wigley, D. Conway, P. D. Jones, B. C. Hewiston, J. Main, and D. S. Wilks, 1998: Statistical downscaling of general circulation model output: A

comparison of methods. *Water Resources Research*, 34, 2995–3008.

Wood A., L. Leung, V. Sridhar, D. Lettenmaier, 2004: Hydrological Implications of Dynamical and Statistical Approaches to Downscaling Climate Model Outputs. *Climate Change*, 62, 189-216.

Zhang X., Vincent L., Hogg W., Niitsoo A., 2000: Temperature and precipitation trends in Canada during the 20th century., *Atmosphere and Ocean.*, 38, 395-429.

Zhang, M., and H. Song, 2006: Evidence of deceleration of atmospheric vertical overturning circulation over the tropical Pacific. *Geophysical Research letters.*, 33, L12701.